# IPP-Report

Max-Planck-Institut für Plasmaphysik

Dominik Brida

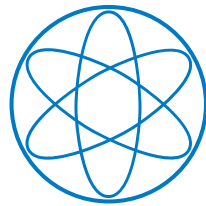**Experimental and Numerical Investigation of Power Exhaust in the Tokamak ASDEX Upgrade with Magnetic Perturbations**

# Technische Universität München

# Physik Department

Lehrstuhl für Plasmarand- und Divertorphysik

# Experimental and Numerical Investigation of Power Exhaust in the Tokamak ASDEX Upgrade with Magnetic Perturbations

## PhD Thesis

## Dominik Brida

Technische Universität München

Max-Planck-Institut für Plasmaphysik

# Experimental and Numerical Investigation of Power Exhaust in the Tokamak ASDEX Upgrade with Magnetic Perturbations

## Dominik Brida

Vollständiger Abdruck der von der Fakultät für Physik der Technischen Universität München zur Erlangung des akademischen Grades eines

Doktors der Naturwissenschaften

genehmigten Dissertation.

| | |
|---|---|
| Vorsitzender: | Prof. Dr. Björn Garbrecht |
| Prüfer der Dissertation: | |
| | 1. Prof. Dr. Ulrich Stroth |
| | 2. apl. Prof. Dr. Andreas Ulrich |

Die Dissertation wurde am 09.11.2017 bei der Technischen Universität München eingereicht und durch die Fakultät für Physik am 10.01.2018 angenommen.

## Abstract

One of the currently most promising concepts to confine high temperature fusion plasmas is the divertor tokamak. In devices of this type a large part of the power which is exhausted from the magnetically confined main plasma is deposited on divertor targets, wall components which are specifically designed to sustain high heat and particle fluxes. The width of the channel in which the power flows to these targets, the so called *power decay length*, is typically only a few millimeters. Hence, in future fusion devices, such as ITER, the material limit of 5–10 MW/m$^2$ of the targets will be exceeded substantially, if no measures to mitigate the heat flux are undertaken.

The strategies to reduce the target heat flux efficiently, e.g. by injecting impurity atoms which radiate in the divertor region, have been investigated in numerous experimental and numerical studies. These studies largely assume an axisymmetric magnetic field geometry. However, in recent years 3D Magnetic Perturbation (MP) fields have been increasingly applied in several tokamaks, in order to mitigate or even suppress edge localized modes, harmful bursts of power and particles from the plasma edge. MP fields break the toroidal axisymmetry of the magnetic configuration and lead in effect to a change of the radial plasma transport. If they find application in future divertor tokamaks, their impacts on power exhaust and the heat flux onto the divertor targets need to be understood.

MP fields might have harmful as well as beneficial consequences for power exhaust. A possible harmful effect is the toroidally asymmetry of the heat flux pattern. It has been speculated that this may lead to a *burn-through*, i.e. the existence of toroidally localized high heat flux regions under conditions which would lead to a low heat flux everywhere without MP field. If this problem arises in ITER, it would be necessary to apply countermeasures, such as rotating the MP field, which would entail substantial engineering efforts. On the other hand, MP fields could lead to the beneficial effect of an increased toroidally averaged power decay length. This effect would not only lead directly to a decreased target peak heat flux due to an increased plasma wetted area, but also increase the volume in which impurities can radiate efficiently.

In this thesis, the effects of MP fields on the plasma transport in the divertor tokamak ASDEX Upgrade (AUG) were studied experimentally and numerically. Moreover, the implications of the results were discussed in view of ITER. Based on the experimental measurements of the heat flux onto the divertor target it will be argued that a burn-through event is unlikely in ITER, since toroidal asymmetries are smoothed out by diffusive transport at low divertor plasma temperatures. In addition to that, the comparison of the experiments with simulations by the transport code EMC3-EIRENE revealed several strong indications that the MP field is screened by currents induced in the plasma. Due to this, the impact on both, the toroidally averaged power

decay length and the radiation, is rather small and barely measurable with the present diagnostics in AUG. In ITER, however, where the power decay length is predicted to be of the same order as in AUG, while the radial perturbation of field line paths by the MP field is much larger, a substantially stronger effect is predicted.

## Zusammenfassung

Eines der derzeit vielversprechendsten Konzepte zum Einschluss von Hochtemperatur Fusionsplasmen ist der Divertortokamak. In Anlagen dieser Art trifft ein Großteil der aus dem Hauptplasma abgeführten Leistung auf sogenannte Divertorplatten. Dies sind Wandkomponenten, welche speziell entworfen wurden um hohen Wärme- und Teilchenströmen standzuhalten. Die Breite des Kanals in dem die Wärme zu den Divertorplatten fließt, die sogenannte Leistungsabfalllänge, beträgt typischerweise nur wenige Millimeter. Daher wird in zukünftigen Fusionsanlagen, wie etwa ITER, das Materiallimit von 5–10 MW/m² erheblich überschritten, wenn keine Maßnahmen zur Verringerung des Wärmeflusses unternommen werden.

Die Strategien um den Wärmefluss auf die Divertorplatten effizient zu reduzieren, z.B. durch Injektion von Verunreinigungsatomen, welche in der Divertorregion strahlen, wurden in zahlreichen experimentellen und numerischen Studien untersucht. Diese Untersuchungen nehmen weitgehend eine axialsymmetrische Magnetfeldgeometrie an. Allerdings wurden in den letzten Jahren in mehreren Tokamaks zunehmend dreidimensionale magnetische Störfelder (MP-Felder) eingesetzt, um am Rand lokalisierte magnetohydrodynamische Moden (ELMs) zu kontrollieren. ELMs führen zu vom Plasmarand ausgehenden Eruptionen von Energie und Teilchen, welche die Divertorplatten schädigen können. MP-Felder brechen die toroidale Symmetrie und führen effektiv zu einer Veränderung des radialen Plasmatransports. Wenn sie in künftigen Divertortokamaks Anwendung finden, müssen ihre Auswirkungen auf die Leistungsabfuhr und den Wärmefluss auf die Divertorplatten verstanden werden.

MP-Felder könnten schädliche sowie nützliche Auswirkungen auf die Leistungsabfuhr haben. Ein möglicher schädlicher Effekt ist die toroidale Asymmetrie des Wärmeflusses. Es wurde spekuliert, dass dies zu einem *Durchbrennen* führen kann, d. h. es existieren toroidal lokalisierte Bereiche mit hohem Wärmefluss, unter Bedingungen, die ohne MP-Feld überall zu einem niedrigen Wärmefluss führen würden. Wenn dieses Problem bei ITER auftritt ist es notwendig Gegenmaßnahmen zu ergreifen, wie z. B. das Rotieren des MP-Feldes, was einen erheblichen ingenieurtechnischen Aufwand erfordern würde. Auf der anderen Seite könnten MP-Felder zu dem vorteilhaften Effekt einer erhöhten toroidal gemittelten Leistungsabfalllänge führen. Dies würde nicht nur die Wärmestromdichte auf die Divertorplatten vermindern, sondern auch das Volumen erhöhen, in dem Verunreinigungen effizient strahlen können.

In dieser Arbeit wurden die Wirkungen von MP-Feldern auf den Plasmatransport im Divertortokamak ASDEX Upgrade (AUG) experimentell und numerisch untersucht. Des weiteren wurden die Ergebnisse im Hinblick auf ITER diskutiert. Basierend auf den experimentellen Messungen des Wärmeflusses auf die Divertorplatten wird argumentiert, dass ein Durchbrennen in ITER unwahrscheinlich ist, da bei niedrigen Plasmatemperaturen im Divertorbereich

die toroidale Asymmetrie des Wärmeflusses durch diffusen Transport ausgewaschen wird. Darüber hinaus zeigte der Vergleich zwischen Experimenten und Simulationen mit dem Transportcode EMC3-EIRENE mehrere starke Hinweise darauf, dass das MP-Feld durch im Plasma induzierte Ströme abgeschirmt wird. Dadurch ist der Einfluss auf beides, die toroidal gemittelte Leistungsabfalllänge und die Strahlung, eher klein und mit den vorliegenden Diagnostiken in AUG kaum messbar. In ITER jedoch, wo eine ähnliche Leistungsabfalllänge wie in AUG erwartet wird, während die radiale Störung der Feldlinien viel größer ist, wird ein wesentlich stärkerer Effekt vorhergesagt.

# Contents

# Chapter 1

# Introduction

The current world wide economic and population growth increases the demand for energy at a rapid pace [1]. At present the energy production relies largely on the exploitation of fossil fuels and nuclear fission. However, the combustion of fossil fuels increases the atmospheric carbon dioxide concentration, which is a main contributor to global warming [2]. Nuclear fission, on the other hand, produces long-lived radioactive waste and fission reactors are prone to accidents. In recent years electric energy is therefore increasingly produced by renewable energy forms. While these are safe and produce only a negligible amount of carbon dioxide, the effectiveness of the energy production depends on the geographic and climatic conditions. Moreover, wind and solar power production can fluctuate strongly.

In the future, nuclear fusion might serve as an additional form of energy production. Nuclear fusion does not bear the safety and environmental risks inherent to nuclear fission and fossil fuels, and its fuel resources are abundant. Furthermore, it is not limited by the same constraints as renewable energies.

The technologically most feasible fusion reaction is the fusion of the hydrogen isotopes deuterium (D) and tritium (T). This reaction produces an alpha particle and a neutron, which have a total energy of 17.6 MeV, i.e. a factor of one million more than in a typical chemical combustion process. However, in order to achieve significant fusion rates, the reactants have to be heated to 100 million Kelvin. At these temperatures the atoms are ionized and a plasma is formed, which consists of free negatively and positively charged particles. The electromagnetic nature of these charged particles has led to the development of various concepts to confine fusion plasmas by magnetic field configurations in order to avoid a contact between this hot matter and the surrounding materials.

The currently most developed design to confine high temperature plasmas is the divertor tokamak. In the divertor tokamak a region of closed field lines, the *confinement region*, and one of open field lines, the *Scrape Off Layer (SOL)* exist. In the confinement region field lines lie on closed surfaces, whereas in the SOL the field lines intersect with target plates located in the divertor. Energy

and particles which diffuse from the confinement region into the SOL are guided along the field towards these target plates. If no energy is dissipated on the way to the targets the power flux density would exceed 100 MW/m$^2$ in future divertor tokamaks. Although the material properties have been optimized in order to sustain large heat and particle loads, it is currently estimated that the steady state heat flux has to be limited to 5–10 MW/m$^2$ in order to guarantee a sufficiently long material life time. Therefore, one of the key problems of fusion research is to limit the peak heat loads on the target plates. In order to achieve this goal a *detached regime* has to be reached. This regime is, in contrast to the *attached* one, characterized by low target heat and ionized particle fluxes, and low plasma temperatures at the target. Detached divertor plasmas have been successfully achieved in several divertor tokamaks.

One of the key features of the tokamak is its inherent axisymmetry, which means that the physical processes can be considered in an effectively two dimensional (2D) space. However, in recent years non-axisymmetric Magnetic Perturbation (MP) fields have been in the focus of intense research, since it is possible to influence Edge Localized Modes (ELMs) with them. ELMs are quasi-periodic bursts of energy and particles, driven by magnetohydrodynamic instabilities, from the edge of the confinement region, which can lead to transient non-tolerable heat and particle loads onto the divertor targets. Mitigating or suppressing ELMs will therefore be mandatory in future fusion devices. Currently, MP fields are discussed for the next step fusion device ITER as an ELM control tool.

Although the strength of the MP field is about a thousand times smaller than that of the unperturbed tokamak field, it can change the magnetic field topology dramatically. As a result, also the divertor heat and particle fluxes become non-axisymmetric. While at some locations along the target this leads to decreased heat and particle fluxes under attached conditions, at other locations the fluxes will increase compared to the unperturbed case.

The redistribution of these fluxes might have favorable as well as unfavorable effects. Among the favorable effects is an effective increase of the radial heat transport, which would lead to an increase of the plasma wetted area on the target. This, in turn, would result in a reduction of the (toroidally averaged) target peak heat flux. The increased effective radial heat transport could, moreover, lead to an increase of the radiating volume and, hence, of the maximum attainable radiation in the SOL [3]. Non-favorable effects of the MPs might be detrimental influences on detachment due to the toroidally localized heat fluxes. Since these can be higher than in the unperturbed case, detachment might be more difficult to achieve.

Understanding the magnetic field structure created by MPs and the plasma transport with these fields is in particular for ITER of high practical relevance. If the toroidally localized heat fluxes occurring with MPs are problematic for reaching detachment, it might be necessary to rotate the MP field, in order to 'smear out' the heat flux. Due to the large forces acting on the MP coils and the

intermittent loads this would be related to enormous engineering challenges.

In addition to this the understanding of up to which degree the MP fields can penetrate the confinement region of the plasma is crucial for predicting the impact on ELMs and the global plasma confinement.

In this thesis, the possible favorable and unfavorable effects of MP fields are investigated in the tokamak ASDEX Upgrade. For this purpose a set of experiments with and without MP fields was carried out. The experiments were accompanied by complementary modeling with the transport code EMC3-EIRENE, which solves the three-dimensional equations governing the transport of energy and particles in a plasma. To obtain a realistic description of the magnetic field in the simulations a model was implemented which accounts for the plasma response shielding the externally applied MP field. The objective was to obtain an understanding of the plasma transport with MP fields in AUG, and infer from this how power exhaust in ITER will be affected by such fields.

# Chapter 2

# Nuclear Fusion, Divertor Tokamaks and ASDEX Upgrade

## 2.1 Nuclear Fusion

Nuclear fusion is the process of two nuclei combining to one nucleus, creating one or several subatomic particles, such as neutrons, as additional byproducts. Due to the equality of mass and energy ($E = mc^2$), energy is released in this reaction if the mass of the products is lighter than the sum of the original nuclei. To enable fusion reactions the energy of the reactants has to be high enough to overcome the Coulomb barrier between the nuclei. In the sun, and other light stars, protons fuse mainly by the so called proton-proton chain reaction [4]. However, this fusion reaction is only efficient due to the high pressure in the sun created by gravitational forces. To produce energy in a fusion device, more efficient fusion reactions have to be used. The technologically most feasible one is that of the hydrogen isotopes deuterium D ($^2$H) and tritium T ($^3$H) to an alpha particle and a neutron

$$D + T \rightarrow {}^4\text{He} \,(3.52\,\text{MeV}) + \text{n} \,(14.06\,\text{MeV}), \tag{2.1}$$
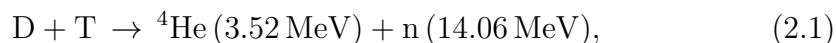
where a total energy of $17.58\,\text{MeV}$ ($1\,\text{eV} = 1.602 \times 10^{-19}\,\text{J}$) is released. In Fig. 2.1 the cross-sections for various fusion reactions are shown as a function of the energy of the reactants. As can be seen, the DT fusion is most efficient at temperatures of several $10\,\text{keV}$[i]. At such high temperatures matter exists in a phase state called *plasma*.

One of the major goals of fusion research is the *ignition* of a fusion plasma, i.e. the energy released from fusion reactions sustains the plasma temperature without additional external heating. To achieve ignition not only the temperature needs to be high enough, but also the density $n$. Furthermore, the thermal insulation of the plasma has to be maximized, in order to reach the high energy density with a minimum amount of input power. A measure for

---

[i]Note that in plasma physics temperatures are often given in energy units with $T$ [eV] $\hat{=}\, T$ [K] $k_B/1.602 \times 10^{-19}$ C, where $k_B = 1.38 \times 10^{-23}$ J/K is the Boltzmann constant.
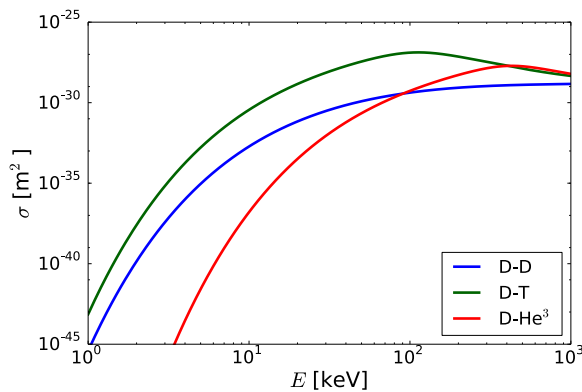
**Figure 2.1:** Cross sections $\sigma$ for D-T, D-D and D-He$^3$ fusion reactions as function of energy $E$ [5,6].

the thermal insulation is the energy confinement time $\tau_E$, which is the time scale on which an unheated plasma cools down. A detailed energy balance shows that in order to achieve ignition the *triple product* $nT\tau_E$ has to fulfill [7]

$$nT\tau_E > 3 \times 10^{24}\,\mathrm{eVsm}^{-3} \tag{2.2}$$

at $T = 15\,\mathrm{keV}$. One of the currently most promising ways to achieve a high triple product is *magnetic confinement fusion (MCF)*, where the plasma is confined by magnetic fields. The two most advanced MCF concepts are the *stellerator* and the *tokamak* [8], of which the latter will be discussed in detail in the following section 2.2. The next step fusion device ITER, which is currently being built in Cadarache, France, is of the tokamak type. It will not yet achieve ignition, but is designed for a *Q-factor* of $Q = 10$ [9], meaning that the power produced by the fusion reactions is ten times larger than that of the external heating.

## 2.2 Magnetic Confinement Fusion Devices

At the beginning of fusion research the attempt was made to produce and confine high temperature plasmas in linear devices. An electric current in the plasma would lead to a contraction of the plasma, which would thus heat up adiabatically. These linear *pinch* devices were, however, prone to instabilities. Moreover, the plasma was in direct contact with the column 'ends', and eroded wall impurities contaminated the plasma. This led to the development of the *tokamak* (Toroidalnay Kamera Magnitnaya Katuschka) in the 1950s in the Soviet Union. Unlike linear devices, the plasma is confined here in a torus. The basic design of a tokamak can be seen in Fig. 2.2. A set of toroidal coils creates a toroidal magnetic field $B_t$, which decays as $R^{-1}$ with the distance $R$ from the torus axis. The decrease of the magnetic field with the radius led to the terms High Field Side (HFS) and Low Field Side (LFS) for the inner and

outer sides of the torus. In a purely toroidal field the positively charged ions will drift to the upper side of the torus, and the negatively charged electrons to the lower one. The result is a vertical electric field, which provokes a drift of the plasma towards the LFS. Therefore, a magnetic configuration with a purely toroidal field leads to poor confinement. A considerable improvement of the confinement can be reached if there is an additional *poloidal field* $B_p$, which connects the upper and lower side of the torus, such that a current, the so called Pfirsch-Schlüter current, can reduce the charge difference [8,10]. The resulting magnetic field lines wind helically around the torus. The poloidal magnetic field can be created by inducing a toroidal current in the electrically conducting plasma via a central solenoid positioned at the torus axis. A more detailed stability analysis shows that this configuration is still not stable and in addition to the toroidal field coils a set of vertical field coils is needed to stabilize the plasma.

The main difference to the related concept of the stellarator, is that in a stellarator the entire magnetic field is created by external coil currents, and no toroidal plasma current is needed. This requires 3D coil shapes, which is challenging from an engineering point of view. Due to its relatively simple design with respect to the stellarator, the tokamak is therefore currently the most developed concept to confine fusion plasmas. Typical temperatures, densities and confinement times that can be reached in todays tokamaks are around $T = 10$–$20$ keV ($\sim 100$ million Kelvin), $n = 10^{19}$–$10^{21}$ m$^{-3}$ and $\tau_E = 10$–$50$ ms. The high temperatures are only possible with external heating systems, such as microwave heating and neutral beam injection. The techniques to heat a fusion plasma will be discussed in more detail in section 2.4.

It is known that the energy confinement time of a tokamak, and therefore its triple product, increases with its size. The currently largest tokamak JET, in which a Q-factor around 0.6 was reached in 1997 [11], has a major radius of $R \approx 3$ m, and the next step fusion device ITER will have a major radius of $R \approx 6$ m. While ITER is not designed as a fusion reactor, its follow-up experiment DEMO is planned to be the first fusion experiment which is equipped with a generator to transform the heat created by the neutrons in the blanket into electric energy. Although it is known which requirements a fusion reactor will have to satisfy, there still remain physical and engineering questions which have to be resolved. Todays tokamak experiments, such as ASDEX Upgrade, are designed to address these problems, and support and prepare the ITER and DEMO experiments. For example, some of the research topics investigated in todays tokamak experiments are:

- How can the confinement be improved?

- How can the heating power be effectively coupled into the plasma?

- How can plasma instabilities be suppressed?

- How can impurities, e.g. the Helium 'ash' or wall impurities, be controlled?

- How can we decrease the heat and power loads onto the vessel walls?

- What materials are best suited for the wall?
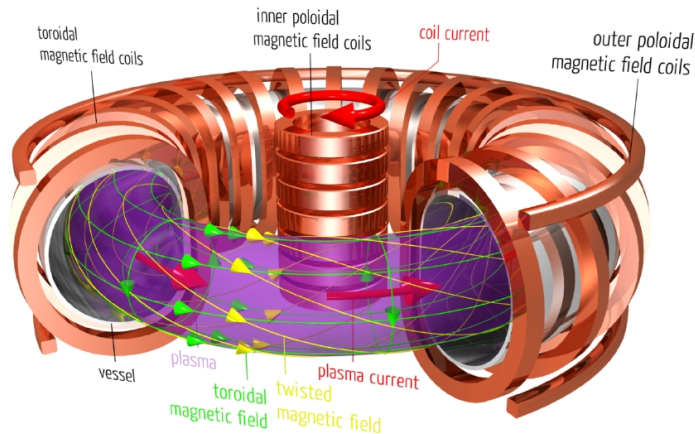


**Figure 2.2:** Illustration of the tokamak concept, from [12].

Finally, the poloidal magnetic flux function $\psi(R, z)$ will be introduced, which is frequently used to map plasma parameters from a two dimensional representation in $R$ and $z$ to a one dimensional profile. The contour surfaces, where $\psi(R, z) = const$, are nested toroidally as shown in Fig. 2.3. Following an individual field line located on a flux surface, the whole surface will be filled out by this field line[ii].

Assuming that the forces due to collisions of the particles in the plasma are negligible, force equilibrium requires the magnetic force to balance the pressure force,

$$\vec{j} \times \vec{B} = \nabla p. \tag{2.3}$$

From (2.3) it can be seen that $\nabla p \cdot \vec{B} = 0$, i.e. the pressure is constant on each flux surfaces. Furthermore, from $\nabla \cdot \vec{j} = 0$ it is seen that the plasma current $\vec{j}$ lies also in the magnetic flux surface. Since the parallel heat conductivity is very large compared to the radial one, it can often be assumed that not only the plasma pressure $p = nT$, but also the temperature $T$ and the density $n$ are constant on each flux surface, i.e. $T = T(\psi)$ and $n = n(\psi)$.

---

[ii]There is a countable set of field lines which close on themselves after a finite number of toroidal turns. These field lines lie on so called *rational surfaces*. A rational surface is always infinitely close to an *irrational surface*.

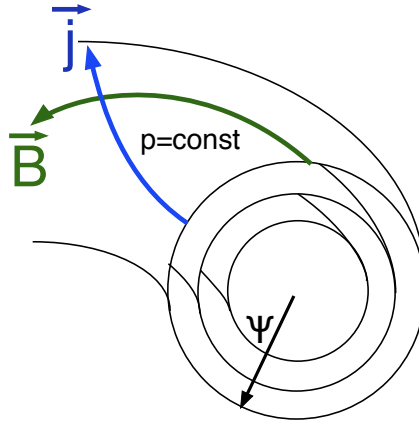**Figure 2.3:** The magnetic field lines $\vec{B}$ form toroidally nested magnetic flux surfaces, which are labeled by $\psi$. The pressure $p$ is constant on each flux surface $\psi$ and the plasma current $\vec{j}$ lies in the flux surfaces.

## 2.3 The Divertor Tokamak

The plasma is surrounded by a vacuum vessel and direct, uncontrolled contact with this vessel has to be prevented. Historically, the first attempts to control the plasma-wall interaction was by inserting protruding elements into the plasma, so called *limiters*, see Fig. 2.4a. This would restrict the plasma-wall interaction to a small area, while protecting the vessel. However, the plasma eroded the limiter material, leading to a contamination of the main plasma with atoms from the limiter material. These *impurities* radiate strongly in the main plasma through bremsstrahlung and line radiation, leading to a cooling of the plasma and, in the worst case, to a disruption of the plasma current. The solution to this problem was found by moving the plasma-wall interaction region sufficiently far away from the confinement region, such that most impurities cannot reach it. This can be achieved by using a *divertor configuration*, which was first realized in the tokamak ASDEX at the Max-Planck-Institut for Plasma Physics in Garching in the 1980s.

In Fig. 2.4b the cross-section of a divertor configuration is sketched. Below the confinement region a conductor is placed, which carries a toroidal current. This leads, in addition to the *O-point*, to a second point where the poloidal field vanishes, the so called *X-point*. The flux surface containing the X-point is called *separatrix*. Below the X-point, divertor targets are placed on the LSF and HFS. The flux surfaces which cross the target plates are called open flux surfaces, while the field lines inside the separatrix which are above the X-point are closed. The region inside the separatrix which is below the X-point is called *Private Flux Region (PFR)*.

In a divertor tokamak, energy and particles diffuse from the confinement region across the separatrix to the region of open field lines. From here the energy and particles are transported along the field lines, while still diffusing radially, i.e. perpendicular to the flux surfaces, outwards. Due to the high ratio of parallel

to perpendicular transport, only a narrow radial layer outside of the separatrix can be filled with plasma before one of the divertor targets is reached. This *Scrape Off Layer* (SOL) has a radial extension of only several mm at the midplane.

As in the case of the limiter, the plasma-wall interaction will create impurities at the divertor targets. However, here most of the impurities return to the target surface before they reach the confinement region.
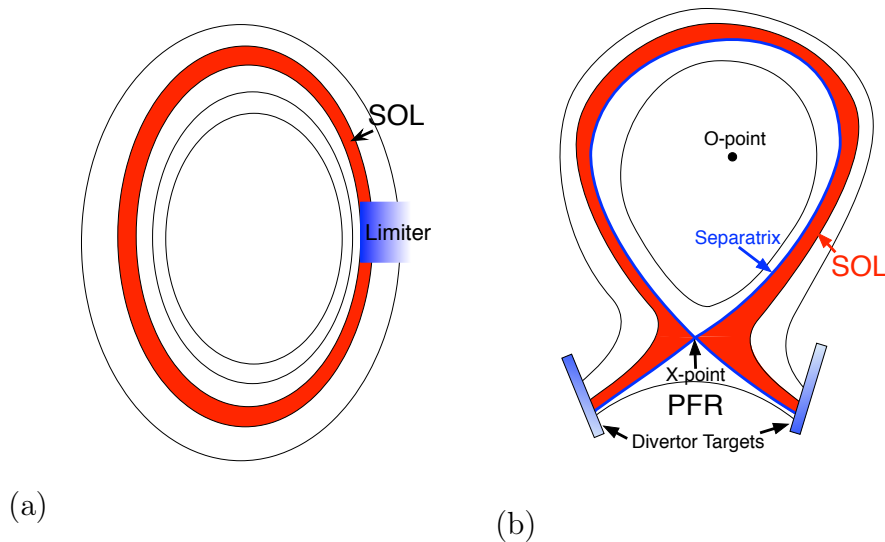


**Figure 2.4:** Illustration of the limiter (a) and divertor (b) concepts.

Apart from preventing impurities from entering the confinement region, the divertor concept proved to have several more advantages compared to the limiter:

- High plasma densities and low temperatures in the divertor region: In the divertor high densities can be achieved, while the temperature is simultaneously reduced with respect to the upstream location. Low divertor temperatures reduce sputtering of target atoms, which leads to a lower impurity contamination and an increased material life time.

- Efficient pumping of helium and deuterium/tritium: In a future fusion reactor helium will be produced in DT fusion reactions. This helium will dilute the plasma fuel species (i.e. D and T) and reduce the efficiency of a future fusion device. The helium content can be reduced by pumps, which are located near the divertor plates [13]. While pumping is also possible in a limiter configuration, it is considerably more efficient in a divertor. The reason for this is that in the divertor volume a high neutral pressure can be achieved, which is not possible near a limiter. Efficient pumping is not only important to remove helium ash, but also to control the D and T density in the plasma.

- Accessibility of the H-mode: The *high confinement mode (H-mode)* [14] is a state in which the confinement of energy and particles in the main plasma is improved by a factor of about 2 with respect to the so called *low confinement mode (L-mode)*. This means that a higher temperature at the same density can be reached, which is beneficial for enabling the fusion reaction. While the H-mode can also be reached in limiter plasmas, it can be accessed more easily and the confinement is better in tokamaks with X-point configuration. The reasons for this are still under investigation.

- Divertor detachment: In the divertor region power can be removed efficiently by volumetric processes, such as radiation [15], which leads to a reduction of the plasma temperature. When the temperature is below about 5 eV atomic processes set in, which reduce the particle flux to the divertor targets [16]. This state is called *detachment*. Due to the reduced power and particle target loads, detachment is a favorable regime compared to the *attached* regime. It is believed that a future fusion reactor will have to achieve (partial) detachment in order to guarantee a sufficiently long material life time. Detachment will be discussed in more detail in section 3.4.

## 2.4   The Tokamak ASDEX Upgrade

In the previous two sections the general design of a divertor tokamak was discussed. In this section the tokamak ASDEX Upgrade (AUG) [17, 18], located at the Max-Planck-Institut for Plasma Physics in Garching, where the experiments presented in this thesis were carried out, is discussed in some detail. AUG is the follow-up experiment of the tokamak ASDEX (Axial Symmetric Divertor EXperiment) [19] which was operated from 1980–1990 in the same institute. In table 2.1 some typical AUG parameters are listed.

| | |
|---|---|
| Major radius $R_0$ | 1.65 m |
| Minor radius $a$ | 0.5 m |
| Mass | 340 t |
| Maximum toroidal magnetic field $B_\phi$ | 3.9 T |

**Table 2.1:** Typical parameters for the tokamak ASDEX Upgrade.

While the objective of the predecessor ASDEX was to show the principle feasibility of the divertor concept, the main objective of AUG is to study plasma boundary and first wall problems under conditions closer to those found in a future fusion reactor [18, 20]. To achieve these conditions the plasma in AUG can be heated with a maximum heating power of about 30 MW, which makes AUG currently the highest powered experimental fusion device with respect to its dimensions.

The heating of the plasma is not provided by a single heating system but by several ones which exploit different physical mechanisms. In the following the heating systems used in AUG are briefly described.

### Ohmic Heating

As mentioned in section 2.2 a toroidal current $I_\phi$ is induced in the plasma of the tokamak. The plasma has a non-zero electrical resistance $R_{pl}$, and the resulting Ohmic heating power is therefore given by

$$P_{OH} = R_{pl} I_\phi^2. \tag{2.4}$$

However, since $R_{pl}$ decreases as $T^{-3/2}$, where $T$ is the plasma temperature, the maximum temperature which can be reached with this heating method is limited. To increase the temperature further external heating mechanisms have to be used. The typical Ohmic heating power is about 1 MW in AUG.

### Radio Frequency and Microwave Heating

The ions and electrons in the plasma gyrate around the magnetic field lines with their respective cyclotron frequencies

$$\omega_{c,i,e} = \frac{eB}{m_{i,e}}, \tag{2.5}$$

where $e$ is the elementary charge, $B$ the local magnetic field strength and $m_{i,e}$ the ion/electron mass. These resonance frequencies lie in the radio-frequency range for ions and in the microwave range for electrons for typical magnetic field strengths in a tokamak. Electromagnetic waves which are injected into the plasma at multiples of $\omega_{c,i,e}$ can be absorbed and heat the respective species. The heated plasma particles thermalize then with the colder ones via collisions. In AUG the maximum power provided by the *Electron Cyclotron Resonance Heating (ECRH)* system, which uses a frequency of 140 GHz, is up to 8 MW. The *Ion Cyclotron Resonance Heating (ICRH)* system has a frequency of 30–50 MHz, and can heat the plasma with further 8 MW.

With the ECRH system it is possible to heat electrons localized within a narrow radial and poloidal range of a few cm, which allows to drive currents in a layer around a specific rational surfaces. With this technique, called *Electron Cyclotron Current Drive (ECCD)*, it is possible to shape the current profile and control thereby certain types of MHD instabilities [21, 22]. The possibility to heat localized will also be used in the heat pulse experiment presented in chapter 5.5.

### Neutral Beam Injection

The method which provides the highest heating power in AUG is Neutral Beam Injection (NBI). Here a high energetic beam of neutral hydrogen or deuterium atoms is generated which – unlike charged particles – are not deflected

by the magnetic field of the tokamak. The neutrals can thus penetrate into the plasma, where they are ionized and thermalize with the colder particles. Currently the maximum NBI heating power in AUG is about 20 MW.

## 2.5 ASDEX Upgrade Diagnostics

ASDEX Upgrade is equipped with about 70 different diagnostics [23], which measure plasma parameters, the magnetic field and vessel conditions. In this section the diagnostics which are most relevant for this thesis, shown in Fig. 2.5, are described. These include, besides diagnostics needed for the magnetic reconstruction, several instruments to measure temperature and density profiles and to characterize the divertor conditions. The physical measurement principle as well as the temporal and spatial resolution of each diagnostic will be briefly discussed.
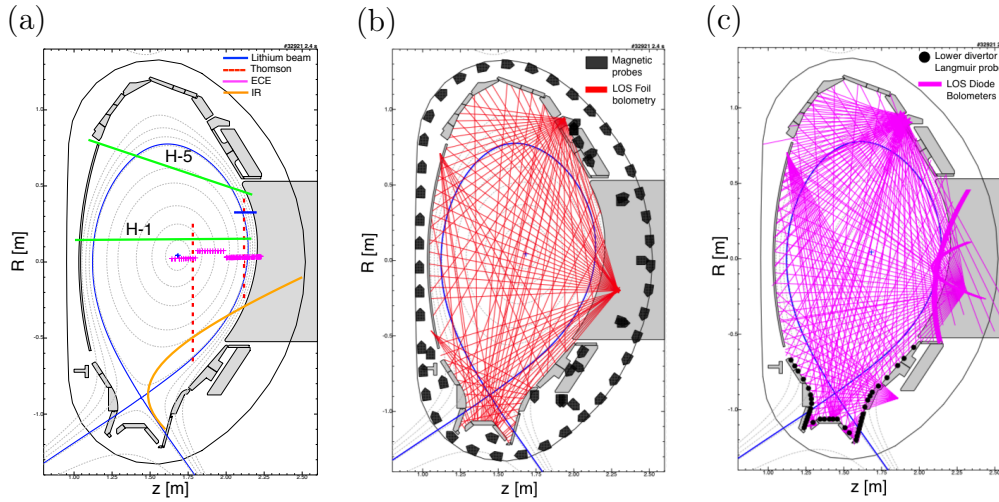


**Figure 2.5:** Poloidal plasma cross section and diagnostics relevant for this thesis. (a) ECE, lithium beam, Thomson scattering, thermography LOS, and H-1 and H-5 interferometry LOS. (b) Foil bolometer LOS, and magnetic pick-up coils. (c) Diode bolometer LOS, and lower divertor Langmuir probes.

### 2.5.1 Magnetic Reconstruction of the Equilibrium Field

As discussed in section 2.2, plasma density and temperature are approximately constant on magnetic flux surfaces. The reconstruction of the magnetic flux surfaces is therefore a key requirement. The poloidal flux function $\psi(R, z)$ can be determined by solving the Grad-Shafranov equation [8]. The Grad-Shafranov equation is a partial differential equation, relating the poloidal magnetic flux to the current distribution in the plasma. In the CLISTE code [24, 25], the current is represented by a linear combination of spline functions. The coefficients of this spline function are then iteratively adapted to

obtain agreement with the magnetic measurements of *pick-up* coils, which are shown in Fig. 2.5b. These coils are arranged around the plasma to measure the time derivative of the magnetic field. Hence, by integrating the coil signals with respect to time, the magnetic field at the coil positions can be obtained.

## 2.5.2 Interferometry

Interferometric techniques allow to measure the line integrated density along a Line Of Sight (LOS). This is achieved by means of a Mach-Zehnder interferometer, where a light beam in the far infrared range is split into a reference beam which bypasses the plasma, and a second beam passing through the plasma. In the plasma the phase speed of electromagnetic waves is proportional to the plasma density. Therefore, the phase shift between the two beams depends on the line averaged plasma density.

In AUG the interferometry light source consists of a DCN laser generating a laser beam at 195 $\mu$m [26], and the line averaged density is measured along five LOS. The two LOS H-5 and H-1, which measure the edge and core line averaged densities, are shown in Fig. 2.5a.

## 2.5.3 Thomson Scattering

The Thomson scattering diagnostic [27] measures density and temperature profiles simultaneously. It is based on the scattering of monochromatic light by electrons. If the Debye length [28] is much larger than the incident wavelength (incoherent scattering), it can be shown that due to the Doppler effect the spectral density of the scattered light is in the non-relativistic case proportional to the electron velocity distribution [29]. From the intensity of the scattered light one can therefore deduce the electron density, and from the spectral density the electron temperature.

In ASDEX Upgrade core and edge vertical Thomson scattering systems exist. The laser system of the core/edge Thomson scattering system consists of a cluster of four/six Nd-YAG lasers with pulse energies of 1 J and pulse durations of 15 ns. The horizontal distance between the lasers of each system is about 3 mm, and each laser has a repetition frequency of 20 Hz.

The scattered light is detected by 16 core and 11 edge channels with a vertical distance of 6 cm between the channels (see Fig. 2.5a).

## 2.5.4 Lithium Beam

The lithium beam diagnostic measures the spectral emissions of a neutral lithium beam, which is injected into the plasma [30, 31]. The technique to estimate the density profile at the plasma edge is based on the strong dependence of the lithium population state $N_i$ of the excitation level $i$ on the plasma electron density $n_e$. Along the lithium beam axis $z$, $N_i$ is given by the solution

of a coupled system of differential equations

$$\frac{dN_i(z)}{dz} = \sum_j (n_e(z)a_{i,j} + b_{i,j})N_j(z), \quad N_j(z=0) = \delta_{1,j} \qquad (2.6)$$

where the coefficient $a_{i,j}$ covers collisional excitation and de-excitation, and the coefficient $b_{i,j}$ spontaneous emission. The lithium beam system measures only the intensity $I_{2p2s}$ of the li(2p) $\rightarrow$ li(2s) transition at 670.8 nm. It is then assumed that $N_2$ is proportional to $I_{2p2s}$. The density is evaluated based on a probabilistic approach, using Bayes' theorem, by solving (2.6) for various test density profiles [32]. The density profile for which the solution of (2.6) and the intensity measurements agree best, is then the most likely one.

In AUG the neutral lithium beam is injected from the LFS with an energy of 60 keV. The high energy is necessary to guarantee that the beam can penetrate far enough into the edge region, before it is completely ionized. To generate the neutral beam, first ions are extracted from a *β-eucryptite* emitter. The ions are accelerated and focused, and after that neutralized before they enter the plasma along the horizontal direction. The line intensity $I_{2p2s}$ along the beam axis is measured at a spatial resolution of about 5 mm (see Fig. 2.5a) by photomultiplier tubes equipped with filters.

### 2.5.5 Electron Cyclotron Emission Radiometry

The Electron Cyclotron Emission (ECE) diagnostic measures midplane electron temperatures with a time resolution of 30 kHz and a spatial resolution of 5 mm in AUG [33]. This diagnostic detects the radiation which electrons emit at multiples of their cyclotron frequency $\omega_{ce}$ (see (2.5)), which depends on the local magnetic field. Since the magnetic field decays approximately as $1/R$, each resonance frequency can be uniquely mapped to a radial location. If the plasma is optically thick enough, it can be considered as a black body and the power radiated at the resonance frequency depends only on the electron temperature at the resonance location. Hence, from spectrally resolved ECE measurements temperature profiles in dependence of $R$ can be obtained.

In order to measure the temperature accurately relativistic effects and Doppler broadening have to be taken into account when analyzing ECE spectra. Moreover, non-Maxwellian electron velocity distributions and finite optical thickness complicate the interpretation of the spectra. In particular in the edge and SOL regions, where the density is low, the condition of high optical thickness is often not fulfilled and the temperature cannot be determined.

### 2.5.6 Bolometry

Bolometers are designed to measure the spectrally integrated radiation along a LOS. By covering the plasma with a network of LOS the total radiation from the plasma volume can be calculated. Moreover, by inversion techniques, such

as the Abel transform, the radiation distribution can be estimated from the measurements along individual LOS.

In AUG two kinds of bolometers are installed: foil bolometers and diode bolometers. In foil bolometers a thin foil is heated by the radiation. The foil covers a meander structure. From the resistance, which changes as the foil temperature changes, the radiated power can be calculated. The foil bolometry system consists of 128 LOS, shown in Fig. 2.5b, and has a data acquisition rate of 2 kHz. The diode bolometers [34] use AXUV diodes, in which a photocurrent proportional to the incoming radiation is induced. The diode bolometry system has 256 LOS, shown in Fig. 2.5c, and acquires data at a rate of 200 kHz. In contrast to the foil bolometers, the diode bolometers have a reduced sensitivity in the ultraviolet spectral region and are not absolutely calibrated.

### 2.5.7 Thermography

To study target heat fluxes, AUG is equipped with an infrared camera [35] which observes the outer divertor target. The camera is directed towards the outer target, rather than the inner one, since the heat flux is here commonly higher. The photon flux $\Gamma_\lambda$ measured by the camera detector at the wavelength $\lambda$, is related to the target surface temperature by Planck's law

$$\Gamma_\lambda(T) = c_0 \epsilon \frac{2\pi c}{\lambda^4} \frac{1}{\exp(\frac{hc}{\lambda k_B T}) - 1}. \tag{2.7}$$

Here $\epsilon$ is the surface emissivity, $c$ the speed of light, $h$ Planck's constant and $k_B$ Boltzmann's constant. $c_0$ is a calibration constant, containing information about the spectral bandwidth and the viewing angle of the camera. After inverting (2.7), from the temporal evolution of the surface temperature the target heat flux can be obtained by solving the heat diffusion equation

$$\rho c_\rho \frac{\partial T}{\partial t} = \nabla \cdot \vec{q}, \quad \text{with} \quad \vec{q} = \kappa \nabla T, \tag{2.8}$$

in the target tile material. Here $\rho$ is the target mass density, $c_\rho$ the target's specific heat capacity and $\kappa$ the target's heat conductivity. Equation (2.8) is solved numerically by using the THEODOR code [36]. The infrared system at the outer divertor in AUG has a spatial resolution of 0.6 mm and a temporal resolution of approximately 1 ms.

At high divertor densities $n$ the IR signal is frequently corrupted by bremsstrahlung, which scales as $n^2$. At these conditions the heat flux cannot be determined from the IR data, and other diagnostics have to be used. One possibility is to use measurements from Langmuir probes, which are discussed below.

### 2.5.8 Divertor Langmuir Probes

Langmuir probes [29] consist of one or multiple electrodes protruding into the plasma. They measure the current-voltage (I-V) characteristics of the

*plasma sheath* which forms self-consistently when a material is brought into contact with a plasma and which will be discussed in section 2.6.1. The I-V curve shape is determined by the plasma particle fluxes and the electron temperature at the sheath entrance. One can therefore derive these plasma quantities by fitting a theoretically derived I-V curve to the measured one. In the divertor of AUG, so called *triple Langmuir probes* [37], which consist of three electrodes, are used. This setup allows measuring three points of the I-V curve simultaneously. Although the triple probe measurements contain less information, compared to a voltage *sweep* which measures the full I-V curve at a rate of 500 Hz, it can measure at a considerably higher rate of 25 kHz. In AUG the poloidal separation of the Langmuir probes is 2–3 cm, and the extension of the collectors is 5 mm. Because of the importance for this thesis, it will be discussed in an extra section how Langmuir probes can be used to measure the target heat flux.

# 2.6 Target Boundary Conditions and Heat Flux Determination by Langmuir Probes

The energy flux to the target can be decomposed into the ion and electron heat flux $q_{kin,i}$ and $q_{kin,e}$, the recombination energy flux $q_{rec}$ and the reflected energy flux $q_{refl}$:

$$q_\perp = q_{kin,i} + q_{kin,e} + q_{rec} + q_{refl}. \tag{2.9}$$

The suffix $\perp$ indicates that the heat flux is perpendicular to the target surface. In the following specific expressions for the individual generic terms in (2.9) will be discussed. These are determined by the boundary conditions imposed by the sheath which forms in front of a target which is connected to a plasma. These boundary conditions will be briefly discussed in the following.

## 2.6.1 Target Boundary Conditions - The Bohm and Chodura Criteria

When a target is brought into contact with a plasma, the electrons – with their much lower mass compared to the ions – reach the target more rapidly than the ions if the electron temperature $T_e$ is of the order of the ion temperature $T_i$. The target surface will therefore charge negatively and a negative electric field in front of the target is created, which repels the electrons. The electron target flux drops until a steady state is reached, in which the electron and ion particle fluxes are equal, resulting in a so called ambipolar flux $\Gamma = \Gamma_e = \Gamma_i$. In this state the electric potential drops from the plasma potential $\phi_p$ to the target potential $\phi_t$ within a distance, which is of the order of the Debye length $\lambda_D$ [28] in an unmagnetized plasma. The region in which this potential drop

occurs is called Bohm sheath and at its entrance the Bohm criterion holds:

$$v_{\perp,t} \geq c_s. \tag{2.10}$$

Here $v_\perp$ is the ion fluid speed normal to the target surface and

$$c_s \approx \sqrt{\frac{k(T_e + T_i)}{m_i}} \tag{2.11}$$

is the ion sound speed at the sheath edge (see Fig. 2.6). In fact, it can be shown that in order to avoid any singularities in the parallel velocity profile, equality has to hold in (2.10). If a magnetic field with a tangential component to the wall is present a *magnetic pre-sheath*, also called *Chodura sheath*, forms in front of the Debye sheath (see Fig. 2.6). This sheath has a typical width of the ion Larmor radius $\rho_i$ and at its entrance the Chodura criterion holds [38, 39]:

$$v_\parallel \geq c_s. \tag{2.12}$$

Here $v_\parallel$ is the thermal ion velocity component parallel to the magnetic field. The Bohm criterion at the Bohm sheath entrance is still valid with magnetic field. The electric field in the Chodura sheath leads to a deflection of the ion trajectories towards the target, such that (2.10) is fulfilled[iii].
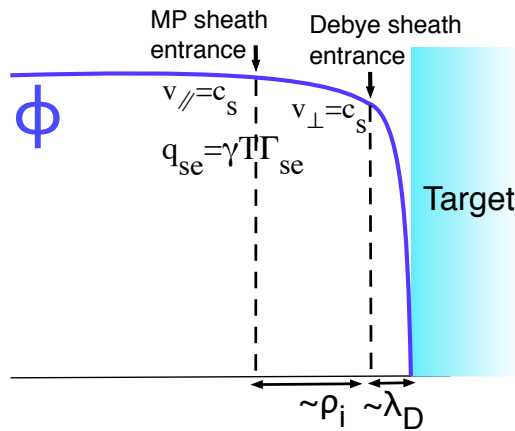


**Figure 2.6:** Illustration of the Bohm and Chodura sheath in front of a target. On the horizontal axis the distance perpendicular to the target is shown. $\phi$ is the electric potential.

The second boundary condition comes from the parallel kinetic heat flux $q_{se}$ at the Chodura sheath entrance, which can be expressed as

$$q_{se} = (\gamma_i T_i + \gamma_e T_e)\, \Gamma_{se}, \tag{2.13}$$

---

[iii]More precisely, as pointed out in [40], it is the gradient of the electric field which leads do a deflection towards the target. A constant electric field would only result in a drift of the plasma tangential to the target.

where $\Gamma_{se}$ is the particle flux at the sheath entrance, and $\gamma_e$ and $\gamma_i$ are the ion and electron *sheath heat transmission factors*. No simple theory exists to determine these factors, since they depend on the ion and electron velocity distributions at the sheath entrance, which are in general not known. However, theoretical considerations give $\gamma_e \approx 5$ and $\gamma_i = 2$–3.5. Often it is assumed that $T_e = T_i \equiv T$ and a total sheath heat transmission factor $\gamma = \gamma_i + \gamma_e$ [41] can be introduced, such that

$$q_{se} = \gamma T \Gamma_t. \tag{2.14}$$

## 2.6.2 Target Heat Flux Determination by Langmuir Probe Measurements and Comparison to Thermography Data

Using the target boundary conditions, expressions for the terms in (2.9) can be derived. We start with the term $q_{kin,i}$, by noting that the kinetic energy transported over the sheath entrance per ion is given by $\gamma_i T_i$. To obtain the kinetic ion heat flux at the target, it has to be taken into account that each ion is additionally accelerated by the sheath potential $V_s$. Therefore, the kinetic energy per ion at the target is approximately given by

$$E_0 = \gamma_i T_i + eV_s, \text{ with } V_s \approx 2.85 T_e/e, \tag{2.15}$$

for a deuterium plasma [42]. The kinetic target ion heat flux can consequently be expressed as

$$q_{kin,i} = (\gamma_i T_i + eV_s)\Gamma, \tag{2.16}$$

where $\Gamma$ is the ambipolar particle flux to the wall.

However, it has to be taken into account that a fraction $R_N$ of the ions is reflected directly from the target as neutrals (see Fig. 2.19 from [43]). The fraction of the total kinetic ion energy which is reflected back in this process is $R_E$, such that the reflected energy flux can be expressed as

$$q_{refl} = -q_{kin,i} R_E. \tag{2.17}$$

The ion energy and particle reflection coefficients increase with decreasing ion impact energy and depend strongly on the involved elements. For example $R_E \approx 0.5$ for deuterium ions with energies of 20 eV impinging on a tungsten target, while for a carbon target $R_E \approx 0.1$ [44]. Therefore, it is to be expected that for a tungsten divertor target, as the one of AUG, ion reflection plays a considerably larger role than for a carbon divertor. The values used for $R_E$ and $R_N$ in this study are obtained from the fit function formula (6) in [44], valid for ion impact energies $E_0 < 10^5$ eV and normal ion impact angles:

$$R_{E,N} = \frac{a_1 \epsilon^{a_2}}{1 + a_3 \epsilon^{a_4}}, \quad \epsilon \equiv \frac{E_0}{\epsilon_L} \tag{2.18}$$

|       | $a_1$               | $a_2$                  | $a_3$                | $a_4$ |
|-------|---------------------|------------------------|----------------------|-------|
| $R_E$ | $2.547 \times 10^{-1}$ | $-1.146 \times 10^{-1}$ | $1.195$              | $1.259$ |
| $R_N$ | $4.453 \times 10^{1}$  | $-8.079 \times 10^{-2}$ | $5.964 \times 10^{-1}$ | $1.344$ |

**Table 2.2:** Fit coefficients for deuterium on tungsten for the fit function (2.18).

where $E_0$ is the impact energy given by (2.15), $\epsilon_L = 9.923\,26 \times 10^3$ for deuterium impinging on tungsten, and the fit coefficients $a_1, ..., a_4$ are given in table 2.2.

The reflection coefficients for tungsten obtained from the fit are plotted in Fig. 2.7 as functions of the electron temperature $T_e$ by the red curves. For comparison the reflection coefficients for carbon are shown by the black curves. Here (2.15) with the assumption $T_i = T_e$ has been used.
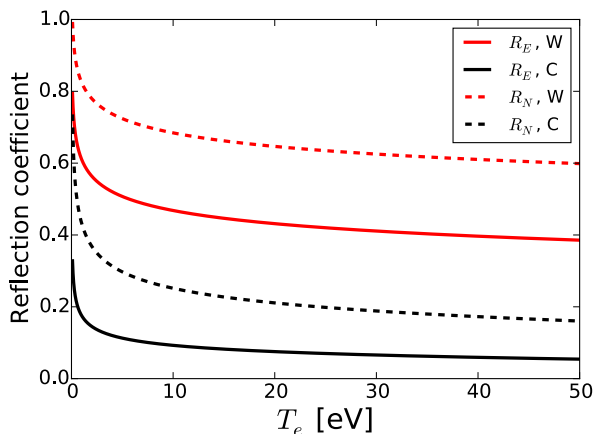


**Figure 2.7:** Energy and ion reflection coefficents $R_E$ and $R_N$ obtained by (2.18) as functions of the electron temperature $T_e$ for tungsten (W) and carbon (C) targets. Eq (2.15) and the assumption $T_e = T_i$ has been used to relate $T_e$ to $E_0$.

The kinetic energy transported over the sheath entrance per electron is given by $\gamma_e T_e$. In contrast to the ions, the electrons are decelerated by the sheath potential. The kinetic target electron heat flux is therefore given by

$$q_{kin,e} = (\gamma_e T_e - eV_s)\Gamma. \tag{2.19}$$

The contribution of the secondary and the reflected electrons is neglected here, since it is assumed that most of these promptly return to the target surface in the presence of a shallow magnetic field angle, due to their finite Larmor radius [45].

It is further assumed that the non-reflected as well as the reflected ions recombine mainly to $D_2$ molecules at the target surface. The recombination energy which is deposited at the target is therefore given by

$$q_{rec} = E_{rec}\Gamma, \tag{2.20}$$

where $E_{rec}$ is the sum of the ionization energy $E_{ion} = 13.6$ eV and the Franck-Condon dissociation energy per recycled ion $E_{FC,D_2} = \frac{4.5}{2}$ eV.

Inserting (2.19), (2.17), (2.16) and (2.20) into (2.9) with $T = T_e = T_i$, the following expression for the target heat flux is obtained (see also [42]):

$$q_\perp = (\gamma_t T + E_{rec}) \, \Gamma, \tag{2.21}$$

where

$$\gamma_t = \gamma_i (1 - R_E) + \gamma_e - R_E \frac{eV_s}{T}. \tag{2.22}$$

Note, that (2.21) is valid at the target, while (2.14) is valid at the sheath edge. Equation (2.21) depends only on the quantities $T_e$ and $\Gamma$, measured by the Langmuir probes. Inserting the values for $\gamma_i = 2$, $\gamma_e = 5$ and $V_s = 2.85T/e$, we get $\gamma_t = 4.85(1 - R_E) + 2.15$. For example, at about 10 eV, $\gamma_t = 6.5$ is obtained for carbon ($R_E \approx 0.1$), and $\gamma_t = 4.8$ for tungsten ($R_E \approx 0.45$).
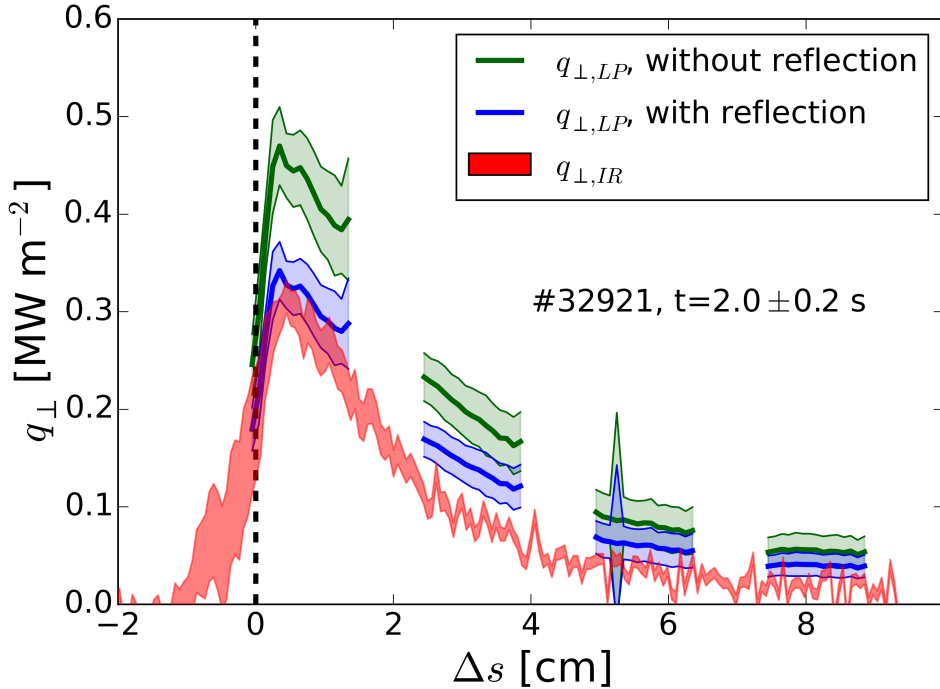


**Figure 2.8:** Thermography (red) and Langmuir probe target heat flux of discharge #32921 for the time range $t = 2.0 \pm 0.2$ s. $\Delta s$ is the distance from the separatrix. The Langmuir probe heat flux is obtained via (2.21), once without taking ion reflection into account (green) and with reflection coefficients obtained by (2.18) (blue).

In Fig. 2.8 the outer target heat flux $q_{\perp,IR}$ of the AUG discharge #32921 (discussed in detail in chapter 6), obtained by the IR diagnostics, is compared to the one obtained from the Langmuir probe measurements according to (2.21). The variable $\Delta s$ in Fig. 2.8 is the distance from the separatrix, where $\Delta s < 0$ corresponds to the private flux region and $\Delta s > 0$ to the SOL. The shown time

range is $t = 2.0 \pm 0.2$ s, where the density is still low and the contribution of Bremsstrahlung to the IR signal can consequently be neglected. In this time range the strike line is moving by about 1.5 cm. Therefore each Langmuir probe measures effectively a continuous part of the profile within these 1.5 cm. The Langmuir probe heat flux is shown once with the fitted reflection coefficients (blue) and once with $R_E = 0$ (green). As can be seen the heat flux measured by IR is overestimated by about 50 % if the ion reflection is neglected, while a considerably better agreement is obtained if reflection is taken into account.

# Chapter 3

# Power Exhaust and Transport Physics

As discussed in the introduction of this thesis, one of the main challenges in future fusion devices is the high power load onto the walls. In this section the problem of *power exhaust* in a divertor tokamak will be further discussed in some detail and simple physical models of the transport in the SOL will be introduced. Although these models do not describe the transport in its full complexity, general dependencies of SOL plasma parameters can be obtained from them.

The next step fusion device ITER is expected to produce a total fusion power of about $P_{tot} = 500$ MW [46, 47], of which about $P_{heat,\alpha} = 100$ MW is going to the alpha particles, which in turn heat the plasma in addition to the auxiliary heating of $P_{heat,aux} = 50$ MW. Ideally $P_{heat} = P_{heat,\alpha} + P_{heat,aux}$ is dispersed isotropically over the first wall to guarantee that no localized heat fluxes occur. However, as we will see, a large fraction of the power tends to be concentrated on a small area on the divertor targets. If no measures are undertaken to mitigate this heat flux the material heat flux limit of 5–10 MW/m$^2$ [48] is exceeded substantially. A thorough understanding of the physical processes of power dissipation and how to control these processes is therefore required.

## 3.1 Power and Particle Balance in a Divertor Tokamak

In Fig. 3.1a the global power balance in a divertor tokamak is illustrated. In the confinement region the plasma is heated with the total heating power $P_{heat}$. In todays experimental tokamaks $P_{heat}$ is provided mainly by the auxiliary heating systems discussed in section 2.4, whereas the plasma in a future fusion reactor will be predominantly heated by fusion reactions. A fraction $P_{vol,\,main}$ of $P_{heat}$ will be dissipated inside the main plasma [49, 50] by volumetric processes, such as radiation. The fraction $P_{sep} = P_{heat} - P_{vol,\,main}$, which is not dissipated

inside the main plasma, is transported across the separatrix. From there the power flows predominantly parallel to the magnetic field lines in a channel with a characteristic width of the so called *power decay length* $\lambda_q$. As will be
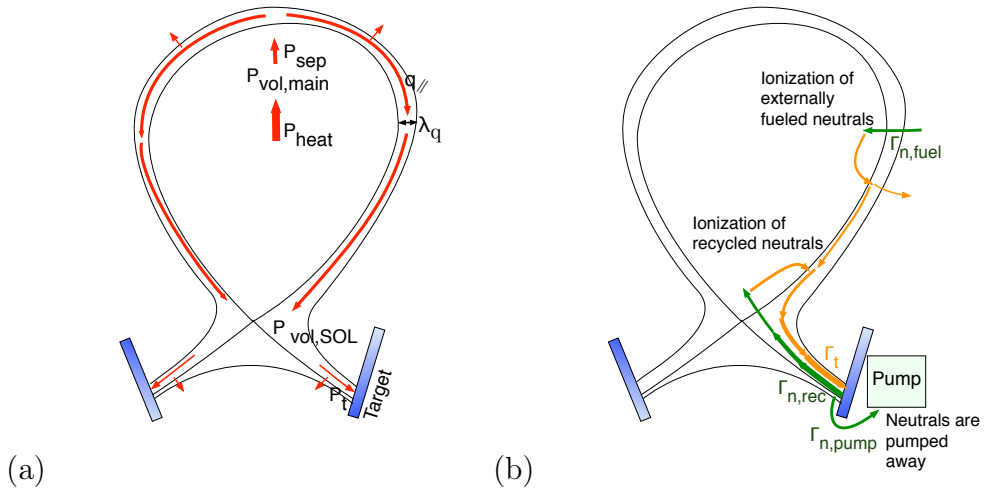


**Figure 3.1:** (a) Illustration of the power exhaust in a divertor tokamak. The plasma is heated by the power $P_{heat}$, from which the fraction $P_{vol,main}$ is radiated inside the separatrix. The power $P_{sep} = P_{heat} - P_{vol,\,main}$ crossing the separatrix is transported along the field lines towards the target within a narrow layer of width $\lambda_q$. In the divertor further volumetric losses $P_{vol,SOL}$ occur, and the power deposited on the target is therefore given by $P_t = P_{sep} - P_{vol,SOL}$. (b) Illustration of the particle exhaust in a divertor tokamak. Here $\Gamma_t$ is the target plasma particle flux. The plasma particles recombine to neutrals in the target and lead to a flux $\Gamma_{n,rec}$ of recycled neutrals away from the target. Most of the recycled neutrals ionize in the divertor region or inside the separatrix, leading again to a plasma particle flux towards the target. A part $\Gamma_{n,pump}$ of $\Gamma_{n,rec}$ can be pumped away behind the target. The plasma is additionally fueled by an external source $\Gamma_{n,fuel}$ of neutrals, which is ionized in the plasma.

discussed in section 3.5, $\lambda_q$ is independent of the tokamak's major radius $R_0$, and in ITER a $\lambda_q$ of only about 1 mm is expected [51]. A deposition of the power within such a narrow region would result in an intolerable high target heat flux. Fortunately, it will be seen that geometric effects and perpendicular diffusion in the divertor region can help to increase the plasma wetted area at the target. In the SOL and in the divertor region, further volumetric losses $P_{vol,SOL}$ occur and the total power which is therefore deposited on the targets is given by $P_t = P_{sep} - P_{vol,SOL}$.

The volumetric radiation in the main plasma and SOL consists of bremsstrahlung and line radiation of impurity ions and fuel neutrals. The impurity ions can be intrinsically produced by sputtering of wall atoms, such as tungsten or beryllium, or deliberately *seeded* into the plasma, in order to increase the radiation and decrease therefore $P_t$. In a future fusion reactor the impurity species and concentration has to be chosen carefully, in order to limit the radiation volume to the edge and SOL region of the plasma, without significant radiation in the core plasma where the fusion reaction takes place. Currently

the use of nitrogen, neon and argon are considered as possible seeding species for this purpose. Their practicability is investigated in AUG and other fusion experiments [49,52,53]. The radiation properties of impurities will be discussed in section 3.3. A further volumetric power dissipation process are energetic neutrals, whose trajectories are not affected by the magnetic field. These fast neutrals are created by charge exchange reactions and elastic collisions of hot plasma ions with slower neutrals (see also section 3.3).

The global particle balance in a tokamak is illustrated in Fig. 3.1b. Plasma particles flow to the targets, resulting in a target particle flux density $\Gamma_t$. For plasma temperatures above 2 eV at the target, most of the incoming ions recombine to neutrals at the target surface, while for lower temperatures, the particles can already recombine in the plasma. Ionization and recombination are further discussed in section 3.3. The neutrals can then leave the target again towards the plasma, leading to a flux $\Gamma_{n,rec}$ of recycled neutrals. In a saturated state the recombination rate in the target equals the neutral flux towards the plasma, i.e. $\Gamma_t = -\Gamma_{n,rec}$. A large fraction of the neutrals coming from the target is then ionized in the plasma, i.e. they lead to a plasma particle source. This process is called *particle recycling*. To control the particle content in the plasma a part $\Gamma_{n,pump}$ of $\Gamma_{n,rec}$ can be pumped away. Furthermore, the plasma is fueled by an external neutral particle source $\Gamma_{n,fuel}$. In contrast to the energy flow, the particle flow forms a largely self-sufficient system, i.e. a large fraction of the ion target flux is created by ionization of recycled neutrals. Therefore, $\Gamma_{n,pump}$ and $\Gamma_{n,fuel}$ are often considerably smaller than $\Gamma_{n,rec}$.

In the next section analytic one-dimensional models for the plasma transport in the SOL will be discussed. These models treat the SOL as an effectively 1D object, which is described by a simplified set of fluid equations. In particular volumetric sources and sinks of particles, momentum and energy, as well as cross field transport are neglected. In section 3.4 the effect of sinks and sources will be considered, which are required to achieve the detached regime. Section 3.5 will discuss two-dimensional effects in the SOL.

## 3.2 Simple One Dimensional SOL Transport Models without Volumetric Dissipation

In this section the simple transport models discussed extensively in [42], will be recapitulated. Any transport model has to fulfill the conservation equations for particles, momentum and energy. Assuming that there are no sinks and sources in the SOL, these equations can be formulated as [42]

$$\Gamma_p \equiv nv = \text{const}, \tag{3.1}$$

$$p_{tot} \equiv m_i n v^2 + p_{stat} = \text{const}, \tag{3.2}$$

$$q_\parallel = \text{const}, \tag{3.3}$$

where $n$ is the plasma density, $v$ the plasma fluid velocity parallel to the magnetic field lines and $m_i$ the ion mass. Equations (3.1), (3.2) and (3.3) state that the parallel particle flux $\Gamma_p$, the *total* pressure $p_{tot}$ and the heat flux $q_\parallel$ are conserved along a field line in the SOL. The static pressure is defined as $p_{stat} \equiv n(T_e + T_i)$, where $T_e$ and $T_i$ are the electron and ion temperatures. By inserting the Chodura boundary condition (2.12), into the pressure conservation equation (3.2), and assuming $T_e = T_i$, the upstream (u) static pressure can be related to the target (t) static pressure by

$$p_u = n_u T_u = 2 n_t T_t. \tag{3.4}$$

The parallel heat flux $q_\parallel$ can be decomposed into conductive and convective terms

$$q = q_i^{conv} + q_e^{conv} + q_i^{cond} + q_e^{cond}, \tag{3.5}$$

where $q_{i,e}^{conv}$ are the ion and electron convective heat fluxes and $q_{i,e}^{cond}$ the ion and electron conductive heat fluxes. The convective heat fluxes can be expressed as

$$q_{i,e}^{conv} = \left( \frac{1}{2} m_{i,e} v_{i,e}^2 + \frac{5}{2} k T_{i,e} \right) n v_{i,e}, \tag{3.6}$$

where $v_{i,e}$ are the ion and electron fluid velocities. The conductive heat fluxes are given, according to *Spitzer-Härm* [54], by

$$q_{i,e}^{cond} = -\kappa_{i,e} T_{i,e}^{5/2} \frac{dT_{i,e}}{dx}, \tag{3.7}$$

where $\kappa_i \approx 60 \, \mathrm{W/(eV)^{7/2}m}$ and $\kappa_e \approx 2000 \, \mathrm{W/(eV)^{7/2}m}$.

We consider now two simplifications of (3.5): In the first case the conductive heat flux can be neglected, which applies if no parallel temperature gradient exists. This case represents the so called *sheath limited regime*. The term sheath limited indicates that in this regime the transport is determined purely by the boundary conditions at the plasma sheath entrance in front of the target, which will be discussed below. The second case represents the other extreme, where the heat flux is only carried by conduction. This is the *conduction limited regime*.

Whether the transport is better described by the sheath limited or the conduction limited regime depends on the particle source location in the SOL, i.e. where the recycled neutrals ionize. In the sheath limited regime the neutrals can penetrate into the main plasma and are ionized there. The particle source is therefore located upstream, and $\Gamma_u = \Gamma_t$ holds due to the conservation of particles. In this situation, which is illustrated in Fig. 3.2 (top), the heat flux can be carried convectively. In the conduction limited regime the neutrals ionize near the target, and $\Gamma_u = 0$. In this case the entire heat flux has to be carried conductively to the target, see Fig. 3.2 (bottom). The transition from the sheath limited to the conduction limited regime can be achieved, e.g. by increasing the density and thereby also the ionization rate in the divertor.
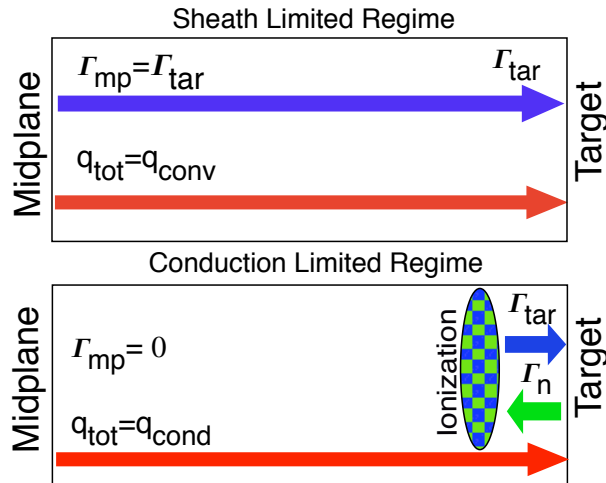
**Figure 3.2:** Sheath and conduction limited regimes.

In the conduction limited regime the upstream temperature $T_t$ and target temperature $T_u$ can be related by integrating (3.7), from the target to the upstream location:

$$q_\parallel L = -\kappa_e \frac{7}{2}(T_u^{7/2} - T_t^{7/2}) \Rightarrow T_u^{7/2} = T_t^{7/2} + \frac{2}{7}\frac{q_\parallel}{\kappa_e}L, \qquad (3.8)$$

where $L$ is the field line length. Here the conductive ion heat flux was neglected, since $\kappa_i \ll \kappa_e$. The set of equations constituted by (3.8), the Bohm-Chodura boundary condition (2.14), and the momentum conservation equation (3.4) is commonly called *two-point model*. Often it can be assumed that $T_u^{7/2} \gg T_t^{7/2}$, and consequently the target temperature can be neglected in (3.8). We obtain therefore

$$T_u = \left(\frac{7q_\parallel L}{2\kappa_e}\right)^{2/7}. \qquad (3.9)$$

It can be seen that $T_u$ depends only weakly on the parallel heat flux $q_\parallel$ and the connection length $L$. In experiments and simulations it can therefore be observed that the upstream temperature is a very robust quantity, with upstream separatrix temperatures of $T_e \approx 50$ eV for L-mode discharges and $T_e \approx 100$ eV for H-mode discharges in AUG.

From the two-point model equations the following dependencies of the target quantities on $n_u$ and $q_\parallel$ are obtained

$$T_t \propto \frac{q_\parallel^{10/7}}{L^{4/7}n_u^2}, \quad n_t \propto \frac{n_u^3 L^{6/7}}{q_\parallel^{8/7}}, \quad \Gamma_t \propto \frac{n_u^2 L^{4/7}}{q_\parallel^{3/7}}. \qquad (3.10)$$

All target quantities depend non-linearly on the upstream quantities, which highlights the difficulties involved in modeling the plasma transport in the SOL. Furthermore, since $T_t \propto n_u^{-2}$, the target temperature can be decreased

efficiently by increasing the density. This effect is sometimes called *energy dilution.* Low target temperatures are beneficial due to the following two reasons: 1) Sputtering of target atoms is reduced. 2) Low temperatures of $T_e < 5$ eV are required to reach the detached regime, which is characterized by low target particle and heat fluxes.

## 3.3 Atomic and Molecular Processes Relevant for Divertor Physics

The simple models discussed above, are only valid if particle, momentum, and power sources and sinks are negligible. However, the ionization region represents a particle source as well as an energy sink. The two-point model is therefore only valid up to this region. Furthermore, as discussed before, the plasma is often deliberately seeded with impurities, such as nitrogen, neon or argon. The radiation by these impurities increases the volumetric power losses in the divertor. At low temperatures additional atomic processes, such as ion-neutral charge-exchange collisions and ion-electron recombination become important and lead to the detached regime. The detached regime and its relevance for future fusion devices will be discussed in some detail in the next section. This section reviews some of the most important atomic processes relevant for divertor physics.

### 3.3.1 Ionization and Recombination

The ionization rate of hydrogen neutrals in a plasma can be expressed as

$$S_i = n_e n_H \langle \sigma_i v \rangle, \tag{3.11}$$

where $n_e$ is the plasma density, $n_H$ the (neutral) hydrogen density[i], and $\langle \sigma_i v \rangle$ the rate coefficient, which depends on the ionization cross-section $\sigma_i$ and the electron velocity distribution. If the electrons are Maxwell distributed the rate coefficients become a function of the electron temperature $T_e$. Figure 3.3 shows ionization and recombination rates for temperatures relevant for fusion plasmas. At higher densities multi-step ionization becomes important, i.e. atoms become ionized from excited states. This leads to an increase of the ionization rate coefficient with density. Furthermore, for temperatures below the hydrogen ionization energy, the ionization rate coefficient drops strongly. The recombination rate $R = n_e^2 \langle \sigma_{rec} v \rangle$, on the other hand, decreases with increasing temperature and at around 2 eV the recombination rate becomes larger than the ionization rate.

Since in a multi-step ionization event an atom can get excited and de-excited multiple times before ionizing, the *effective* ionization energy $E_i^{eff}(n_e, T_e)$ is

---

[i]The atomic properties of hydrogen and deuterium are very similar, and therefore commonly atomic data of hydrogen is used for deuterium.

larger than the ionization energy of $E_i = 13.6$ eV. For divertor plasmas a typical value for $E_i^{eff}$ is 30 eV. At low densities recombination is dominated by two-body recombination, and all of the recombination energy is emitted by radiation. At higher densities three-body recombination events become important, where part of the recombination energy goes to the second electron. By this process three-body recombination can increase the electron temperature.
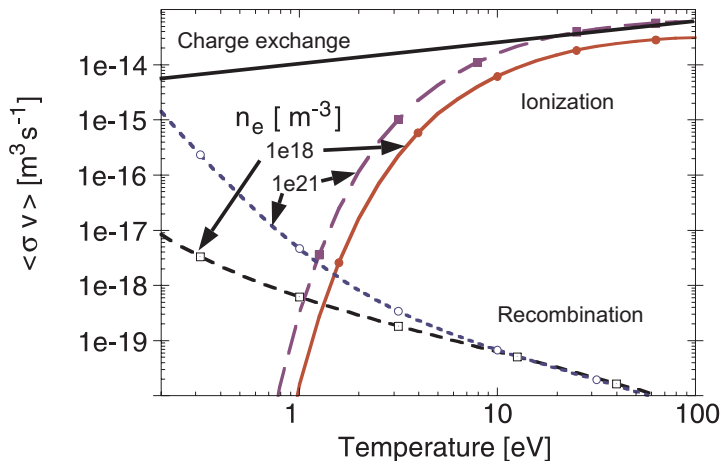


**Figure 3.3:** Ionization, recombination and charge exchange rates for hydrogen [55].

## 3.3.2 Ion-Neutral Friction

In the divertor region hot plasma flows into a 'cushion' of cold neutrals, and at sufficiently low temperatures ion-neutral friction has to be taken into account here. That is, the plasma loses momentum due to charge-exchange (CX) collisions and elastic scattering of ions with neutrals. For ion-neutral collisions to be effective, a sufficiently large number of them has to occur before a neutral ionizes. As can be seen in Fig. 3.3, the ratio of the charge-exchange collision rate and the ionization rate increases rapidly below 10 eV, and therefore only below this temperature ion-neutral collisions play a significant role. If the neutrals leave the plasma after an ion-neutral collision, this process also represents an energy sink.

## 3.3.3 Impurity Radiation

In future fusion devices volumetric power losses due to hydrogen radiation and losses from charge exchange, will not suffice to reduce the target power load to low enough levels. To increase the volumetric power losses further, impurity atoms can be seeded into the plasma. These impurities contribute to the power loss by line radiation and bremsstrahlung. The radiated power $P_{rad}$ by an impurity species can be expressed by its *loss parameter* $L_z$ by

$$P_{rad} = n_H n_Z L_z. \tag{3.12}$$

Here $n_H$ and $n_Z$ are the hydrogen and impurity species densities. Figure 3.4 shows the radiative loss parameter $L_z$ as a function of the electron temperature $T_e$. Typical divertor temperatures are around 10 eV, while further upstream in the SOL the temperature is about 100 eV. In the edge region of the plasma, i.e. just inside the separatrix, several hundred eV to 1 keV are common. From Fig. 3.4 it can therefore be seen that carbon and nitrogen radiate mainly in the divertor, while argon also radiates further up in the SOL and partly inside the separatrix. Krypton can also radiate in the core region. Impurities which radiate significantly at higher temperatures can lead to a confinement degradation. The right seeding recipe which leads to high SOL radiation, while maintaining good confinement, is the subject of current investigations [56].
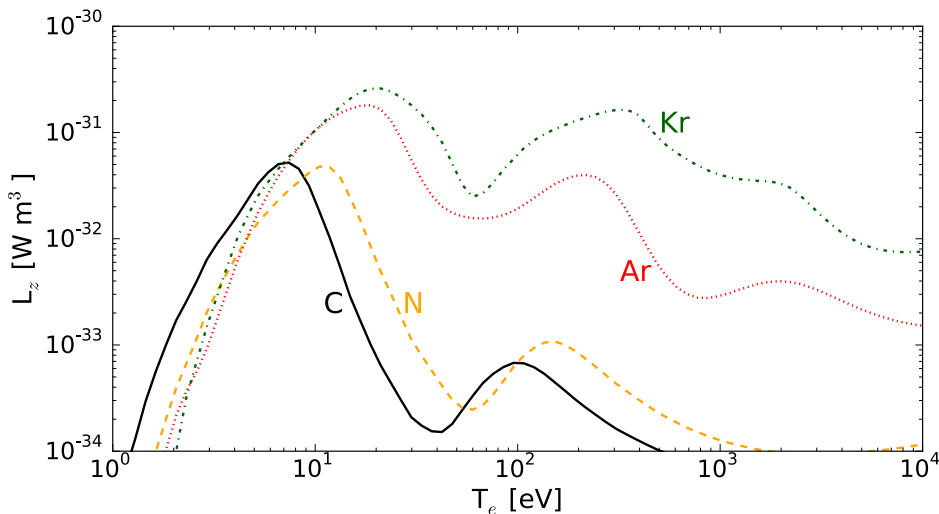


**Figure 3.4:** Power loss factors $L_z$ for carbon (C), nitrogen (N), argon (Ar) and krypton (Kr) in dependence of the electron temperature $T_e$. $L_z$ was calculated using the ADAS data base [57].

## 3.4 Divertor Detachment

As the divertor temperature reaches sufficiently low values the detached regime is reached. This regime is not only characterized by a low target heat flux, but also a drop of the target particle flux and density. The transition to the detached regime is exemplified in Fig. 3.5a from ASDEX, where the divertor density $n_t$, the divertor electron temperature $T_{e,t}$ and ion temperature $T_{i,t}$, in dependence of the core density are plotted [58]. As the upstream density increases, $T_{e,t}$ decreases and $n_t$ increases initially. When $T_{e,t}$ reaches about 5 eV the density *rolls over*, i.e. $n_t$ is decreasing again. The roll over marks the beginning of detachment.The experimental observations during detachment can be analyzed, by using a corrected form of the two-point model, which takes into account loss terms. For this the generic factors $f_{pow}$ and $f_{mom}$ are
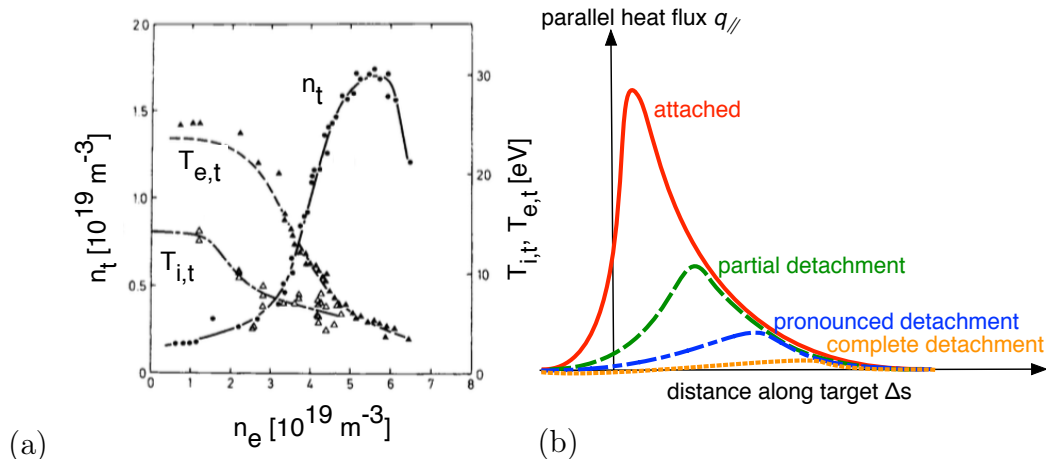
**Figure 3.5:** (a) Measurements of the divertor density $n_t$, the divertor electron temperature $T_{e,t}$ and ion temperature $T_{i,t}$ in ASDEX in dependence of the averaged edge density $n_e$ [58]. (b) Illustration of target heat flux profiles for and attached case and partially, pronounced and completely detached cases [59].

introduced, such that

$$q_t = (1 - f_{pow})q_\parallel, \tag{3.13}$$

$$2n_t T_t = f_{mom} n_u T_u, \tag{3.14}$$

and the two-point target quantities given in (3.8) have to multiplied by the following factors:

$$T_t \propto \frac{(1 - f_{pow})^2}{f_{mom}^2}, \quad n_t \propto \frac{f_{mom}^3}{(1 - f_{pow})^2}, \quad \Gamma_t \propto \frac{f_{mom}^2}{1 - f_{pow}}. \tag{3.15}$$

As can be seen from (3.15), volumetric power losses lead, as expected, to a decrease of the temperature. However, they lead at the same time to an increase of the target particle flux. For the target particle flux and the density to decrease simultaneously, as observed experimentally in the detached phase, significant momentum losses have to occur in addition. Combining the condition of decreasing temperature and density we obtain $f_{mom}^{3/2} < (1 - f_{pow}) < f_{mom}$ from (3.15). Specific physical processes which can lead to momentum loss are ion-neutral friction and recombination. As discussed in the last section, ion-neutral friction becomes effective below 5 eV and recombination below 1–2 eV. Furthermore, ion-neutral friction slows down the plasma, and enables it to recombine before reaching the target.

Commonly *detachment* is defined by a significant drop of the total plasma pressure. Following this definition, detachment would in principle be possible without a significant power loss. However, since the physical processes which can lead to momentum loss require low temperatures, a sufficiently large fraction of the power has to be dissipated already upstream. Therefore, a significant pressure loss is always accompanied by a significant power loss.

The details of the detachment process are not yet fully understood. For example, it is debated if recombination as well as ion-neutral friction are necessary to explain its principal characteristics. It was argued that ion-neutral friction alone is able to explain detachment, and that recombination is only a secondary effect, which decreases the particle flux further [60]. However, in numerical 2D simulations of divertor plasmas the pressure loss due to ion neutral-friction was not able to explain the experimentally observed pressure loss alone [61]. Recombination, therefore, seems to be a necessary ingredient for detachment in a tokamak divertor. Moreover, it is not yet clear if all relevant atomic and molecular processes are included in todays simulations to reproduce the experimental results quantitatively.

In the current divertor of AUG detachment does not occur uniformly along the target, but starts near the strike line, and proceeds then further towards the far SOL. For practical reasons different detachment states have been introduced, which classify which region of the divertor is detached. The target heat flux profiles for these detachment states are sketched in Fig. 3.5b. In a *partially detached state* the heat flux is reduced within 1–2 power decay lengths $\lambda_q$. For *pronounced detachment* the heat flux is reduced over several $\lambda_q$ and in *complete detachment* along almost the full divertor. Pronounced detachment was, however, only achieved under conditions where the confinement of the core plasma already degrades, and therefore it is currently planned to operate ITER in a partially detached regime [47].

## 3.5 Two Dimensional Effects in the SOL: The Power Decay Length and the Power Spreading Factor

In the discussion of the simple models in section 3.2 the SOL was treated as an one dimensional object. However, geometrical effects as well as the perpendicular plasma transport require a 2D description. This section discusses how this 2D nature can be characterized. First the flux expansion will be introduced, which is a purely geometrical effect due to the expansion of magnetic flux bundles in the poloidal plane. After that the power decay length $\lambda_q$, which was already introduced in section 3.1, and the divertor spreading factor $S$ will be discussed in some detail.

### 3.5.1 Definition of the Flux Expansion

The parallel heat flux $\vec{q}_\parallel$ in the SOL, which flows along the magnetic field $\vec{B}$, can be decomposed into its toroidal and poloidal components

$$\vec{q}_\parallel = q_\parallel \left( \frac{\vec{B}_t}{B} + \frac{\vec{B}_p}{B} \right). \tag{3.16}$$

We consider now a ring element at the outer midplane of the plasma torus with width $\delta r_1$, located at the radius $R$. The poloidal projection of this ring element is seen in Fig. 3.6. The area of the ring is $A_1 = 2\pi R \delta r_1$, and the heat flux through it is given by

$$\delta P_1 = A_1 q_{p,1}, \quad \text{where} \quad q_{p,1} \equiv q_{\parallel,1} \frac{B_{p,1}}{B_1}, \tag{3.17}$$

As one traces the ring element along the field lines, the width of it will change to $\delta r_2$, its area to $\delta A_2$, and the magnetic field to $\vec{B}_2$. From the soleonidality of the magnetic field, we obtain

$$\int_V \mathrm{d}V \nabla \cdot \vec{B} = \int_{A_1} \mathrm{d}\vec{A}_1 \cdot \vec{B}_1 + \int_{A_2} \mathrm{d}\vec{A}_2 \cdot \vec{B}_2 = A_1 B_{p,1} - A_2 B_{p,2} = 0,$$

$$\Rightarrow \frac{A_1}{A_2} = \frac{B_{p,2}}{B_{p,1}} \tag{3.18}$$

where $V$ is the volume enclosed by $A_1$, $A_2$ and the connecting flux surfaces. By inserting (3.18) into (3.17), and using energy conservation, $\delta P_1 = \delta P_2$, we obtain

$$q_p \propto B_p. \tag{3.19}$$

In particular, if the aspect ratio of the tokamak is large, $R/a \gg 1$, then $R$ will be approximately constant along the SOL. This means that any change of $A$ is mainly due to a change in $\delta r$, i.e. the distance between the flux surfaces changes. This 'stretching' of the flux surface with respect to the midplane is often called *flux expansion*, and the ratio $f_x^* = \delta r_t / \delta r_u$, where the subscripts $u$ and $t$ correspond to the midplane and the target, is called flux expansion factor.

Commonly one is interested in the heat flux perpendicular to the target $q_{\perp,t}$, which is obtained by projecting the poloidal heat flux onto the target surface

$$q_{\perp,t}(s) = q_{p,t}(s) \sin(\beta) = \frac{q_{p,u}(s)}{f_x}, \quad \text{where} \quad f_x = \frac{f_x^*}{\sin(\beta)}. \tag{3.20}$$

Here $\beta$ is the angle between the target and the poloidal field and $s = r_t/\sin(\beta)$ is the distance along the target. The factor $f_x$ is the *integral* or *effective* flux expansion, which takes into account the magnetic flux expansion as well as the tilting angle $\beta$. The tilting angle depends in general on the local magnetic field and can vary over the target, however, in AUG $f_x = 4.5$ can be assumed within good approximation.

## 3.5.2 The Power Decay Length $\lambda_q$

From experiments and simulations it is known that the parallel heat flux $q_{\parallel}$ has an exponential form at the midplane,

$$q_{\parallel} = q_0 e^{-\frac{r_u}{\lambda_q}}, \text{ with } q_0 = \frac{\int q_{\parallel} \mathrm{d}r_u}{\lambda_q} = \frac{P_u}{2\pi R \lambda_q} \frac{B_u}{B_{p,u}} \tag{3.21}$$
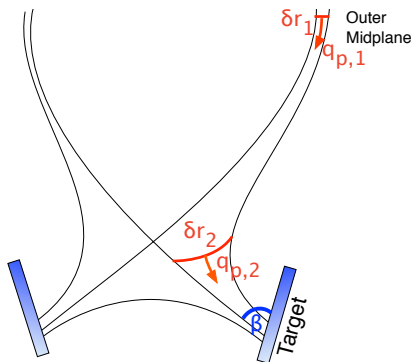
**Figure 3.6:** Illustration of the flux expansion near the X-point.

Here $r_u$ is the distance from the separatrix at the midplane, and $\lambda_q$ the power decay length. The power decay length is one of the most important parameters to estimate the peak heat flux in a future fusion device. However, considering the multitude of plasma transport effects which determine $\lambda_q$, it is also a little understood quantity from a theoretical point of view. Experimentally, a number of studies investigated the scaling of $\lambda_q$ with plasma and tokamak parameters. Recent studies, which have compared $\lambda_q$ in devices with varying major radius $R$, give the following scaling laws[ii]

$$\lambda_q^L \approx 1.44 B_t^{-0.8} q_{95}^{1.14} P_{sep}^{0.22} R^{-0.03} \tag{3.22}$$

for L-mode plasmas [62], and

$$\lambda_q^H \approx 0.73 B_t^{-0.77} q_{95}^{1.05} P_{sep}^{0.09} R^{0.0} \tag{3.23}$$

for H-mode plasmas [51]. Here $q_{95}$ is the *safety factor* at $\psi_N = 0.95$[iii], i.e. close to the separatrix. The safety factor, which is a function of the poloidal magnetic flux surface $\psi$, is the number of toroidal turns a field line completes within one poloidal turn. The regression analysis for the L-mode scaling included the tokamaks AUG and JET, and the one for the H-mode scaling JET, C-MOD, AUG and DIII-D.

These scalings show almost no correlations with $R$, i.e $\lambda_q$ is independent of the machine size. In particular for ITER a $\lambda_q$ of about 1 mm [51] is found by the H-mode scaling.

### 3.5.3 The Divertor Spreading Factor $S$

In last section is was discussed that the upstream heat flux profile can be described by an exponential with e-folding length $\lambda_q$. In the divertor region, however, this exponential profile diffuses towards the private flux region: Figure 3.7 illustrates this effect. At the X-point region an exponential profile with

---

[ii]Here $B_T$, $P_{sep}$, and $R$ are given in [T], [MW] and [m], respectively, and $\lambda_q$ in [mm].

[iii]See equation (4.4) for a definition of the normalized poloidal magnetic flux $\psi_N$.
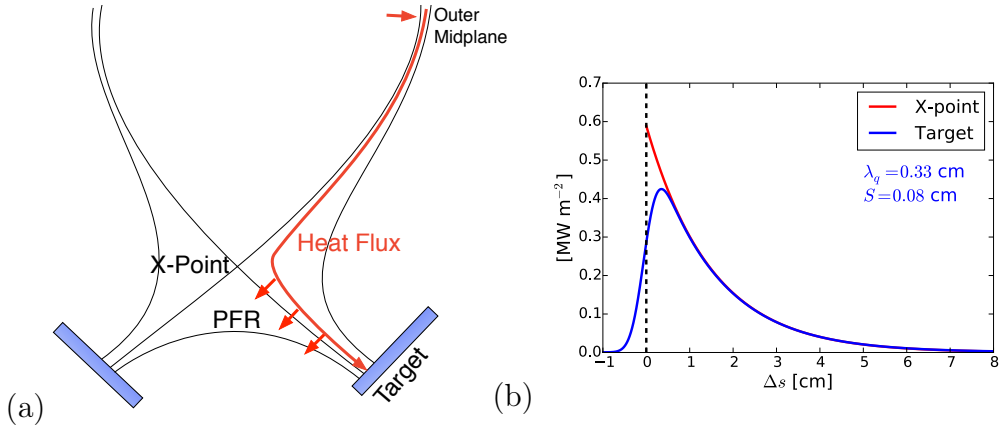
## 3.5. Two Dimensional Effects in the SOL



**Figure 3.7:** (a) Illustration of the heat flux spreading towards the Private Flux Region (PFR) in the divertor. (b) Heat flux profile at the X-point (red) and at the target (blue) for a power decay length $\lambda_q = 3.3$ mm and a divertor spreading factor of $S = 0.8$ mm.

e-folding length $\lambda_q$ can be assumed. The heat is transported from the X-point within the typical time $\tau$ to the target. The diffusion of the profile during $\tau$ can be described by the following diffusion equation

$$K_\perp \frac{\mathrm{d}q_\parallel}{\mathrm{d}t} = \frac{\mathrm{d}^2 q_\parallel}{\mathrm{d}r^2}, \tag{3.24}$$

with the initial heat flux distribution given by the profile at the X-point. The fundamental solution of (3.24) is given by a Gaussian of width $\sqrt{4K_\perp t}$. The target heat flux is accordingly given by the convolution of the upstream profile with this fundamental solution (see e.g. [63])

$$q_{\parallel,t} = q_{0,\parallel} e^{-\frac{r_t}{f_x^* \lambda_q}} \otimes \frac{1}{f_x^* S \sqrt{\pi}} \exp\left(\frac{-\Delta r_t^2}{(f_x^* S)^2}\right). \tag{3.25}$$

Here $r_t$ is the distance along the target from the separatrix in the direction orthogonal to the flux surfaces, and $S$ is the *divertor spreading factor*

$$S \equiv \sqrt{4K_\perp \tau} \tag{3.26}$$

We use the convention that $\lambda_q$ and $S$ are given by their values mapped to the midplane, hence they are multiplied by the flux expansion factor $f_x^*$ in (3.25). The spreading of the heat flux profile in the divertor leads to a decrease of the peak parallel heat flux. This motivates the definition of the *integral power decay length*

$$\lambda_{int} = \frac{1}{f_x^* q_{max,t}} \int q_{\parallel,t}(r_t) dr_t, \tag{3.27}$$

where $q_{max,t}$ is the maximum value of $q_{\parallel,t}(r_t)$. In Ref. [64] it is derived that

$$\lambda_{int} \approx \lambda_q + 1.64S. \tag{3.28}$$

When diffusive parallel transport is assumed, the time $\tau$ in (3.26) is inversely proportional to the heat conductivity, $\tau \propto K_{\parallel}^{-1}$. By using the Spitzer expression for $K_{\parallel}$, and writing $K_{\perp} = n_e \chi_{\perp}$, we obtain therefore

$$S \propto T_e^{-1.2} n_e^{0.5} \sqrt{\frac{\chi_{\perp}}{\kappa_e}}. \tag{3.29}$$

For L-mode discharges in AUG a scaling according to[iv]

$$S = 2.11 T_{e,tar}^{-1.28} n_{e,tar}^{0.66} A^{-0.84} B_{pol}^{1.33} + 1.42 \frac{\rho_i}{f_x} \tag{3.30}$$

was experimentally found [65]. Here $A$ is the ion mass number. The dependence on the temperature and the density agrees approximately with the estimation (3.29). Additionally the scaling shows a dependence on the ion Larmor radius $\rho_i$ at the target. This term becomes important at higher temperatures, where the finite Larmor radius leads again to an increase of $S$.

---

[iv]$T_{e,tar}$, $n_{e,tar}$, $B_{pol}$, and $\rho_i$ are given in [eV], [$10^{19}\,\mathrm{m}^{-3}$], [T], and [mm], respectively, and $S$ in [mm].

# Chapter 4

# Magnetic Perturbations in ASDEX Upgrade

Until now tokamaks were considered in this work as ideally axisymmetric and 3D effects played no role. However, in recent years 3D magnetic perturbations have been routinely applied in several tokamaks worldwide, in order to study their effect on Edge-Localized Modes (ELMs) [66, 67]. ELMs are magneto-hydrodynamic instabilities which arise due to the interplay of large pressure and current gradients in the edge of H-mode plasmas [68, 69]. In each of the ELM crashes, which occur quasi-periodically at a frequency of the order of 100 Hz, plasma particles and energy are ejected from the plasma edge. In ITER unmitigated ELMs will lead to intolerable large divertor target heat and particle loads, and therefore ELM control techniques will be mandatory. The physical process by which MPs influence ELM stability is still a matter of active research. Numerical and experimental studies indicate that ELM control is associated with the appearance of so called kink modes [70–74], which lead to a deformation of the plasma. However, the mechanism by which these kink modes affect ELMs is currently not understood in detail.

Apart from the magnetohydrodynamic interaction with the plasma, the topological changes in the magnetic field created by the MPs lead effectively to a change of the radial plasma transport. Since in a fusion plasma, the parallel transport is orders of magnitudes larger than the perpendicular one, this topological change is clearly reflected in the 2D distribution of the plasma parameters on the divertor plates. In this section the MP coils in AUG will be described and characteristic topological properties of a magnetically perturbed field will be discussed.

The arrangement of the MP coils in AUG is depicted in Fig. 4.1a. In Fig. 4.1b a poloidal cross section of the vessel is shown, with the MP coils indicated in green. The MP coil system consists of eight lower (Bl) and eight upper (Bu) saddle coils, which are located at the LFS below and above the outer toroidal midplane, respectively. The coils are mounted on the Passive Stabilizing Loop (PSL), a massive copper conductor which slows down the growth of the ver-

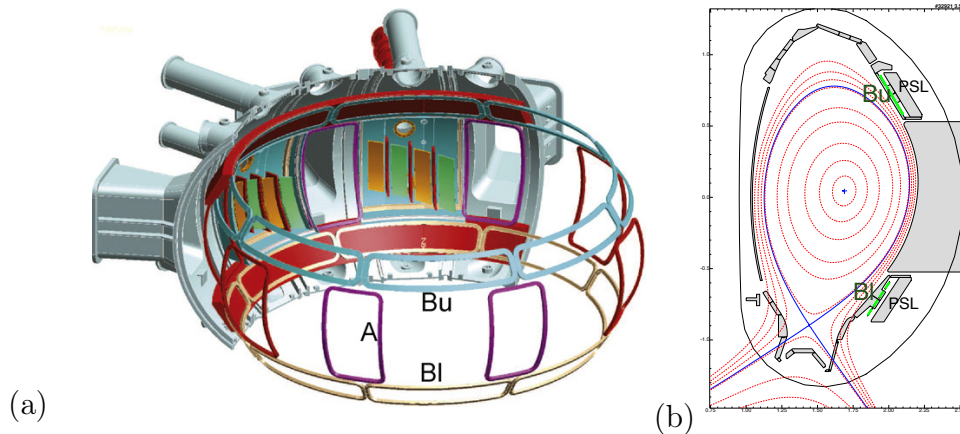tical plasma instability. Each coil consists of five copper windings, which are



**Figure 4.1:** Model of the eight upper (Bu) and eight lower (Bl) MP saddle coils in ASDEX Upgrade (a), and cross-cut of a saddle coil (b). Coils A are a concept for future extensions.

centrally water cooled. The 16 MP coils can be controlled individually and in particular alternating MP coil currents, with phase shifts between the coils, can be generated. Due to the electromagnetic forces acting on the coils in the tokamak's magnetic field the current in each coil is limited to 1 kA per turn for a standard toroidal field strength of $|B_t| = 2.5$ T, and 1.3 kA per turn for reduced toroidal field strength ($|B_t| \leq 2.0$ T). Since there are five turns in each winding this amounts to 5 kA and 6.5 kA, respectively.

By applying alternating coil currents, with appropriately chosen phase shifts between each coil, a toroidally rotating MP field can be approximated. However, since the time averaged amplitude of an alternating current is only a factor $1/\sqrt{2}$ of the maximum current, a rotating MP field is reduced by the same factor with respect to a static MP field. Moreover, a rotating MP field induces eddy currents in the PSL. The field created by these eddy currents leads to a reduction as well as a phase shift of the MP field, which depends on the MP rotation frequency. The typical decay time of an induced current in the PSL is around $\tau \approx 0.6$ s, i.e. for coil currents with a frequency of $f > \frac{1}{\tau} \approx 2$ Hz, a significant shielding effect of the PSL on the MP field is expected. Detailed finite element simulations [75] result in the curve plotted in Fig. 4.2, where the relative field strength $B^{MP}$ created at a coil current frequency $f$, and that of a static MP field $B^{MP}_{f=0}$ is shown on the left axes. At $f = 2$ Hz the MP field is reduced by about 30 %, and at $f = 5$ Hz by about 50 %. On the right axes in Fig. 4.2 the dependence of the toroidal phase shift on $f$ is shown. Here it can be seen that for frequencies between 10 and 100 Hz the phase shift due to the PSL is about 20°.
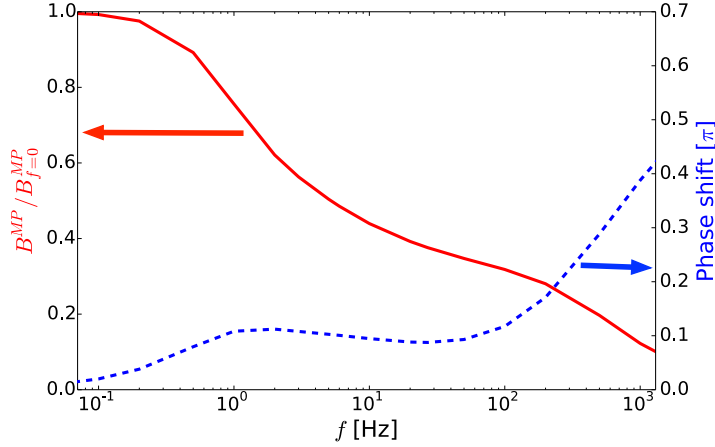
**Figure 4.2:** Left axes: Relative reduction of the MP field strength $B^{MP}/B^{MP}_{f=0}$ with coil current frequency $f$ due to the PSL. Right axes: Toroidal phase shift of the MP field due to the PSL in dependence of $f$.

## 4.1 Perturbed Magnetic Fields

In this section the magnetic field created by the MP coils is analysed and some commonly used terms to characterize the MP field configuration are introduced. Generally, the magnetic field can be represented according to

$$\vec{B}(R, z, \phi) = \vec{B}^{eq}(R, z) + \vec{B}^{MP}(R, z, \phi) + \vec{B}^{resp}(R, z, \phi), \qquad (4.1)$$

where $\vec{B}^{eq}$ is the axisymmetric equilibrium field before switching on the MP coils, $\vec{B}^{MP}$ the field created by the MP coils, and $\vec{B}^{resp}$ is the field created by the plasma in response to the MP field.

The total equilibrium field can be expressed by

$$\vec{B}^{eq} = B^{eq}_R \vec{e}_R + B^{eq}_z \vec{e}_z + B^{eq}_\phi \vec{e}_\phi, \qquad (4.2)$$

where the poloidal field component can be obtained from the poloidal flux function, according to [8, 76]

$$B^{eq}_R = -\frac{\partial \psi}{\partial z}, \quad B^{eq}_z = \frac{\partial \psi}{\partial R}. \qquad (4.3)$$

The poloidal flux function itself is, as discussed in section 2.5.1, calculated by the CLISTE code. The toroidal component of the equilibrium field can be calculated as $B^{eq}_\phi = B^{eq}_{\phi,0} R_0/R$ in good approximation, where $B_{\phi,0}$ is the toroidal magnetic field at an arbitrary $R = R_0$. In this thesis the flux function $\psi$ of $\vec{B}^{eq}$ will also serve as a radial coordinate for perturbed as well as unperturbed equilibria. Specifically, the normalized magnetic poloidal flux, which is defined as

$$\psi_N = \frac{\psi - \psi_{xp}}{\psi_{xp} - \psi_{op}}, \qquad (4.4)$$

will be used. Here $\psi_{xp}$ and $\psi_{op}$ are the values of $\psi$ at the X-point and O-point of $\vec{B}^{eq}$, respectively (cf. Fig. 2.4). By this definition points lying on the separatrix of $\vec{B}_{eq}$ have the value $\psi_N = 1$. Commonly, the coordinate $\rho \equiv \sqrt{\psi_N}$ is used instead of $\psi_N$.

$\vec{B}^{MP}$ is calculated from the coil geometry and the coil currents by using Biot-Savart's law. To take into account the attenuation by the PSL when the MP field is rotating, $\vec{B}^{MP}$ has to be multiplied by the corresponding reduction factor shown in Fig. 4.2. The plasma response $\vec{B}^{resp}$ will be discussed in section 4.4. In this section we make the assumption $\vec{B}_{resp} = 0$, which is often called *vacuum approach*.

While the MPs have a poloidal (i.e. along the magnetic flux surfaces), as well as a perpendicular (i.e. perpendicular to the magnetic flux surfaces) component, it is mainly the perpendicular one which is responsible for the non-axisymmetric topological field changes. Formally the perpendicular field component is given by

$$B_\psi = \frac{\vec{B}^{MP} \cdot \nabla \psi}{|\nabla \psi|}, \tag{4.5}$$

where $\psi$ is the poloidal flux of $\vec{B}^{eq}$. At the separatrix $B_\psi$ is around 5 mT in the vicinity of the coils, which is about $0.2\,\%$ of the toroidal magnetic field. $\vec{B}_\psi$ can be expressed as the sum of the fields $\vec{B}_{\psi,u}$ and $\vec{B}_{\psi,l}$ created by the upper and lower row of coils. Due to the toroidal periodicity, these fields can be written as a Fourier series according to

$$B_{\psi,u,l}(R, z, \phi) = \Re \left( \sum_{n'} \tilde{B}_{\psi,u,l}^{n'}(R, z) e^{i(n'\phi - \varphi_{u,l})} \right) \tag{4.6}$$

The MP field configuration is often denoted by its principal toroidal mode number $n$ and the differential phase shift $\Delta\varphi \equiv \varphi_u - \varphi_l$ between upper and lower MP field. Here $n$ is the $n'$ with the largest $\tilde{B}_{\psi,u,l}$. With the 8 upper and 8 lower coils in AUG the toroidal mode number is restricted to $n = 1, 2, 3$ and $4$. The differential phase shift $\Delta\varphi$ should not be confused with the toroidal phase shift in space $\Delta\phi = \frac{\Delta\varphi}{n}$ between upper and lower MP field. For clarification Fig. 4.3 shows the phasing of the $B_u$ and $B_l$ currents for a $n = 2$ configuration with $\Delta\varphi = -90°$ (a), $\Delta\varphi = 0°$ (b) and $\Delta\varphi = 90°$ (c). The toroidal phase shifts are $\Delta\phi = 45°, 0°$ and $45°$ for (a), (b) and (c), respectively.



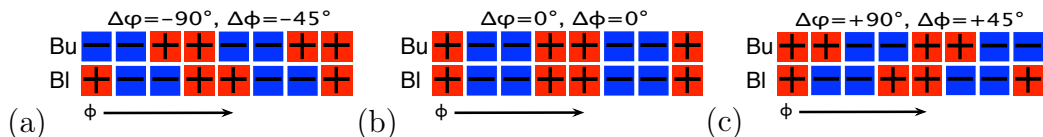**Figure 4.3:** Illustration of the upper and lower coil currents for a $\Delta\varphi = -90°$ (a), 0° (b) and 90° (c).

The differential phase $\Delta\varphi$ determines the *resonance* of the MP field, as illustrated in Fig. 4.4 for two $n = 2$ cases, one with $\Delta\varphi = -90°$ (a) and one with

$\Delta\varphi = 90°$ (b). The black arrows in Figs. 4.4a+b sketch the path of an unperturbed field line near the separatrix, with respect to the poloidal and toroidal angles $\theta$ and $\phi$. The colors of the boxes indicate the direction of the radial magnetic field $B_\psi$ created by the upper and lower MP field coils, where blue means that the field is directed inwards, and red that it is directed outwards. In the $\Delta\varphi = -90°$ case the field line passes the lower as well as the upper MP coil row in a region where $B_\psi < 0$, hence this configuration is called *resonant* near the separatrix. In the $\Delta\varphi = 90°$ case the lower row is passed in a $B_\psi < 0$ and the upper row in a $B_\psi > 0$ region. In this case the radial field line displacements due to the MP fields of the two coil rows counteract. Hence this configuration is *non-resonant* near the separatrix.
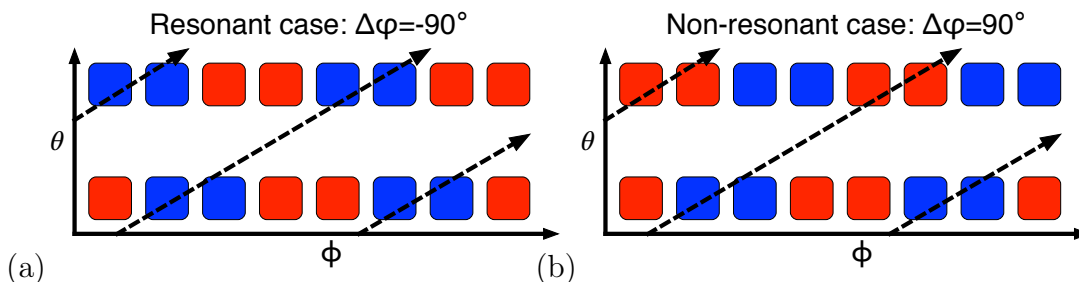


**Figure 4.4:** Sketch of a resonant (a) and a non-resonant (b) MP field configuration. Here $\theta$ and $\phi$ denote the poloidal and toroidal angles. The black dashed arrows show the path of an unperturbed field line on a constant flux surface near the separatrix. The blue and red boxes indicate negative and positive radial magnetic field regions, respectively. In the resonant case the field line experiences inwards displacements at the lower as well as at the upper MP coil row, i.e. the displacements add up. In the non-resonant case the displacements at the lower and upper coil rows are of opposite sign.

In the following section the resonance condition will be discussed in a quantitative way in terms of Fourier components. It will be shown that at rational surfaces a resonant radial perturbation field gives rise to island structures in the magnetic topology. When islands of neighboring rational surfaces start to overlap the field line dynamics becomes non-linear, leading to a *stochastic* field [77].

## 4.2 Rational Surfaces, Magnetic Islands, and Stochastic Magnetic Fields

Rational magnetic surfaces are magnetic surfaces on which the helical field lines complete $m$ integer toroidal turns after $n$ integer poloidal turns. The *safety factor* on a rational surface is then given by $q = m/n$. On a rational surface MPs can induce a fundamental topological field change, with chains of *magnetic islands* being created along the flux surface. In Fig. 4.5 an illustration of a magnetic island chain for a $q = 3$ surface is shown. The islands in the chain are separated by *X-points*, and the center of an island is called *O-point*.

Field lines in the island are separated from field lines outside the island by a *separatrix*[i]. In the toroidal direction the islands move along the unperturbed magnetic field lines.
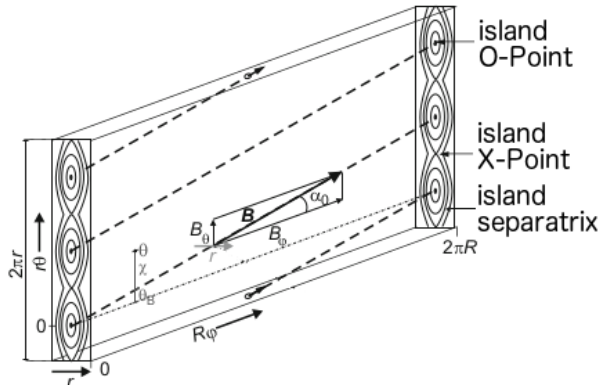


**Figure 4.5:** Illustration of an $m = 3$ island chain adapted from [10].

To formulate the resonance condition mathematically we introduce the straight field line coordinate system $(\phi, \theta^*)$ on a flux surface with safety factor $q$. Here $\phi$ is the usual toroidal angle, and $\theta^* \equiv \frac{\phi}{q}$ parametrizes the poloidal coordinate of the flux surface. In this coordinate system a field line on the flux surface is described by a straight line $\theta^* = \frac{\phi}{q} + c$, where $c$ is a constant. We now introduce the normalized radial magnetic field $b^1$,

$$b^1 \equiv \frac{\vec{B} \cdot \nabla \psi_N}{\vec{B} \cdot \nabla \phi}, \tag{4.7}$$

which can be Fourier decomposed with respect to $\theta^*$ and $\phi$,

$$b^1(\phi, \theta^*) = \sum_{m,n} \tilde{b}^1_{m,n} e^{i(m\theta^* - n\phi)}. \tag{4.8}$$

If $\tilde{b}^1_{m,n} \neq 0$ on a rational surface with $q = \frac{m}{n}$ a magnetic island will be created on that surface, where the number of islands seen in a poloidal cross-section is equal to the mode number $m$. It can be shown that the corresponding half-width $w$ of the island in terms of $\psi_N$ is approximately given by [78]

$$w(m, n) = \sqrt{\frac{4q^2 \tilde{b}^1_{m,n}}{q' m}}, \tag{4.9}$$

where $q' = \frac{dq}{d\psi_N}$.

---

[i]Note that in tokamak physics the terms X-point, O-point and separatrix usually refer to the equilibrium field. When discussing these terms with respect to magnetic islands this will be explicitly stated.

If the islands of two neighboring resonant surfaces start to overlap, the dynamics of field lines become strongly non-linear and the field line paths can become stochastic. A formal measure for stochasticity is the *Chirikov parameter* [79]

$$\sigma_{chir}(m,n) = \frac{w(m,n) + w(m+1,n)}{\Delta(m,m+1)} \qquad (4.10)$$

where $\Delta(m, m+1)$ is the distance in $\psi_N$ between the rational surfaces with $q = \frac{m}{n}$ and $\frac{m+1}{n}$. Stochasticity sets in for $\sigma_{chir} \gtrsim 1$. It is possible that stochasticity is a requirement to achieve ELM mitigation [66, 80], however, whether this condition is necessary is currently under debate.
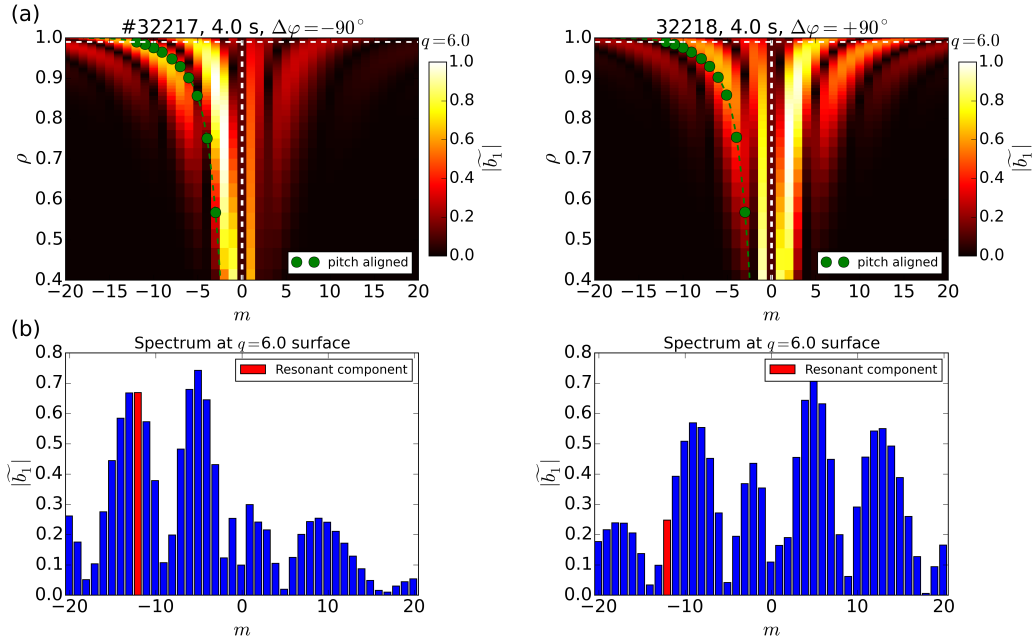


**Figure 4.6:** Mode spectrum in dependence of $\rho$ (a) and mode spectrum at the $q = 6.0$ surface, corresponding to $\rho \approx 0.99$, (b) for the the $\Delta\varphi = -90°$ (resonant) case (left) and $\Delta\varphi = +90°$ (non-resonant) case (right).

In Fig. 4.6a the radial dependence of the Fourier components $\tilde{b}^1_{m,n=2}$ for the discharges #32217 (left) and #32218 (right) at $4.0\,\mathrm{s}$ are shown. The MP field configuration of #32217 is $n = 2, \Delta\varphi = -90°$, i.e. it corresponds to the resonant case shown in Fig. 4.4a, while the MP field configuration of #32218 is $n = 2, \Delta\varphi = 90°$, i.e. it corresponds to the non-resonant case shown in Fig. 4.4b. The radial distance in Fig. 4.6a is given in $\rho = \sqrt{\psi_N}$. The locations of the resonant surfaces are indicated by the green circles, where the $m$ coordinate is given by the resonant $m$, i.e. $m = 2q$. For $\rho > 0.95$ it can be seen that the resonant Fourier components for the resonant case are larger than that for non-resonant one. This can be seen more clearly in Fig. 4.6b, which shows the spectra at the $q = 6.0$ surface indicated by the horizontal dashed lines in the top plots. The corresponding resonant component at $m = -12$ is marked in red in (b).
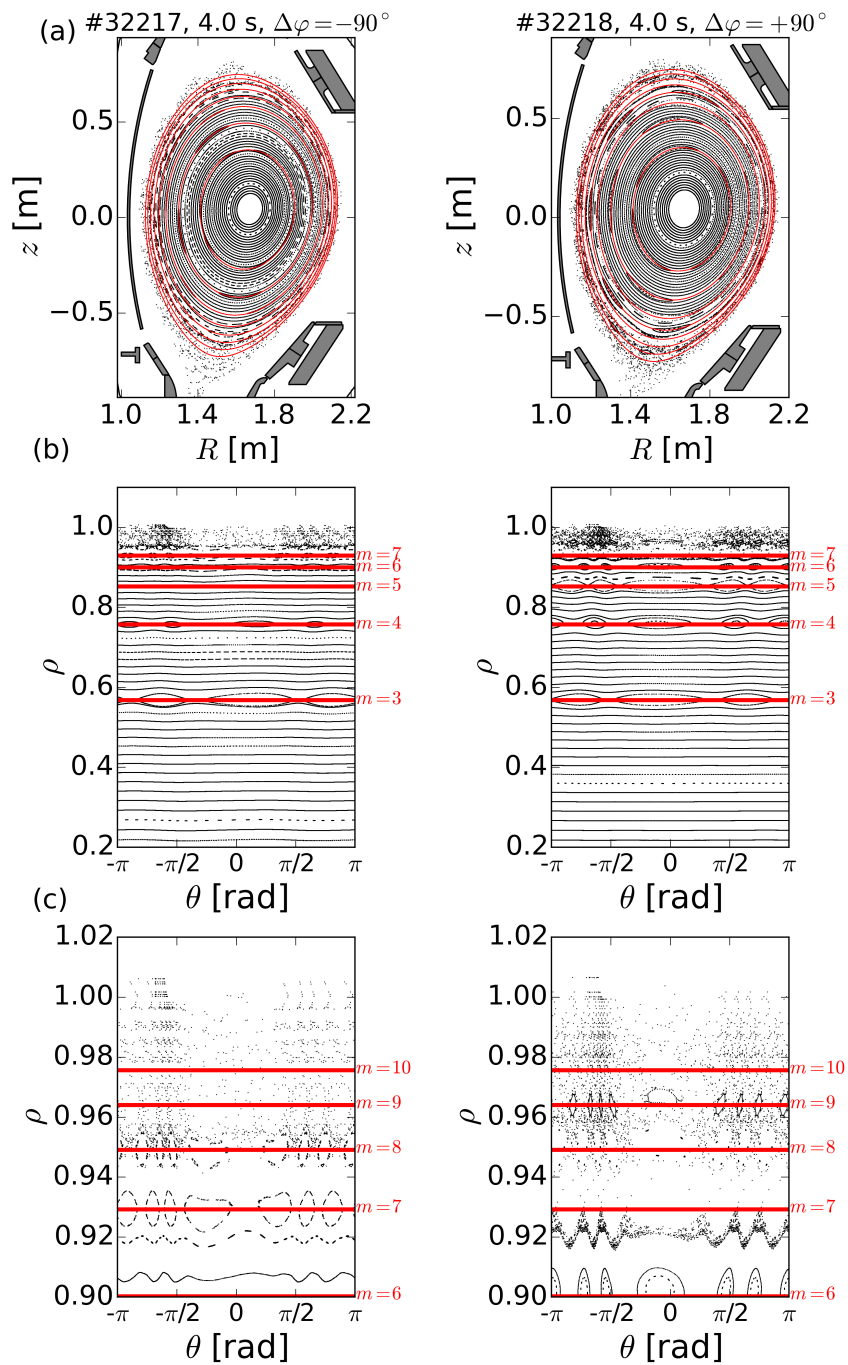
**Figure 4.7:** Poincaré plots for the resonant (left) and non-resonant (right) cases in $(R, z)$ coordinates (a) and $(\rho, \theta)$ coordinates (b). In (c) the zoomed-in region between $\rho = 0.9$ and $1.02$ of (b) is shown.

The topological structure of the magnetic field can be conveniently visualized by using *Poincaré plots*. In Fig. 4.7 such plots are shown for the resonant (left) and the non-resonant cases (right) discussed above. In (a) the Poincaré plots in real space coordinates $(R, z)$ are shown, while (b) shows them in $(\theta, \rho)$

coordinates. The rational surfaces for $q = \frac{m}{2}$, with $m = 3...7$ are shown by the red lines in (a) and (b). In Fig. 4.7c the zoomed-in region between $\rho = 0.9$ and 1.02 of (b) can be seen.

In both cases at surfaces which are resonant for $m < 8$ well defined, non-overlapping island structures exist. These island structures are particularly well visible in Fig. 4.7b at the surfaces resonant with $m = 3$ and 4. For surfaces resonant with $m > 8$ a stochastic behavior sets in, with no discernible closed magnetic flux surfaces. However, in the non-resonant case remaining island structures still exist at the surface resonant with $m = 9$ (see Fig. 4.7c). Moreover, the stochastic region is in the non-resonant case more densely filled than in the resonant one, since in the latter case the field lines hit the target more rapidly. In other words the resonant case is more stochastic in the edge region than the non-resonant one, as it is also expected from the larger resonant Fourier components in the edge region (see. Fig. 4.6b).

In a stochastic region field lines diverge exponentially on short length scales, i.e. the distance $d$ of two infinitesimally close field lines scales according to

$$d = d_0 e^{\frac{l}{L_K}}, \tag{4.11}$$

where $d_0$ is their original distance, $l$ is the parallel field line length, and the length $L_K$ is called *Kolmogorov length* [81]. On larger length scales field lines in the stochastic region become de-correlated. This leads to a diffusive behavior where the field line paths can be described by a *field line diffusion coefficient* $D_{FL}$ [77, 82]. This means statistically the distances between two field lines scales as

$$d \propto \sqrt{D_{FL} l}. \tag{4.12}$$

Due to the fast parallel plasma transport, the diffusion of field lines leads effectively to an increased perpendicular diffusion of heat an particles with respect to the unperturbed field lines.

## 4.3 Connection Length and Magnetic Lobes

A key geometrical parameter to describe the magnetic topology is the connection length of the field lines. The connection length of some point $(R, z, \phi)$ is the distance along the magnetic field line between this point and the target. We distinguish here between the connection lengths $L_{c,inner}$ and $L_{c,outer}$ to the inner and outer target, and the total connection length $L_{c,tot} \equiv L_{c,inner} + L_{c,outer}$. Field lines with long connection lengths are expected to carry a larger heat flux to the target than field lines with short connection lengths, since they penetrate statistically deeper into the hot main plasma.

Connection length plots for the inner, outer, and total connection lengths are shown in Fig. 4.8 for the resonant case. In the bottom plots a zoomed-in view of the divertor region is shown. For $\vec{B}^{MP} = 0$ field lines at $\psi_N < 1$ are closed and have consequently infinite connection lengths. In contrast,

in a perturbed field, field lines inside $\psi_N = 1$ can hit the target, and have therefore finite connection lengths. In the outer connection length plot, shown in Fig. 4.8a, finger-like structures at the HFS with long connection lengths can be seen. These so-called *magnetic lobes* extend towards the SOL and intersect in the divertor region with the inner target. Conversely, with $L_{c,inner}$, shown in Fig. 4.8b, the lobes appear at the LFS and intersect with the outer target. As one follows the lobe structures from above the X-point towards the divertor leg, they lengthen due to the strong magnetic shear near the X-point. Simultaneously they decrease in width, since flux conservation requires the area of a magnetic flux bundle to be constant. Near the divertor leg the lobes align along it, while becoming infinitesimally narrow.

The projection of the magnetic lobes onto the target, a so called *magnetic footprint*, results in a spiraling structure, which will be discussed in more detail in chapter 5. As will be seen, this structure is well reflected in the target heat flux pattern observed in experiments and simulations.
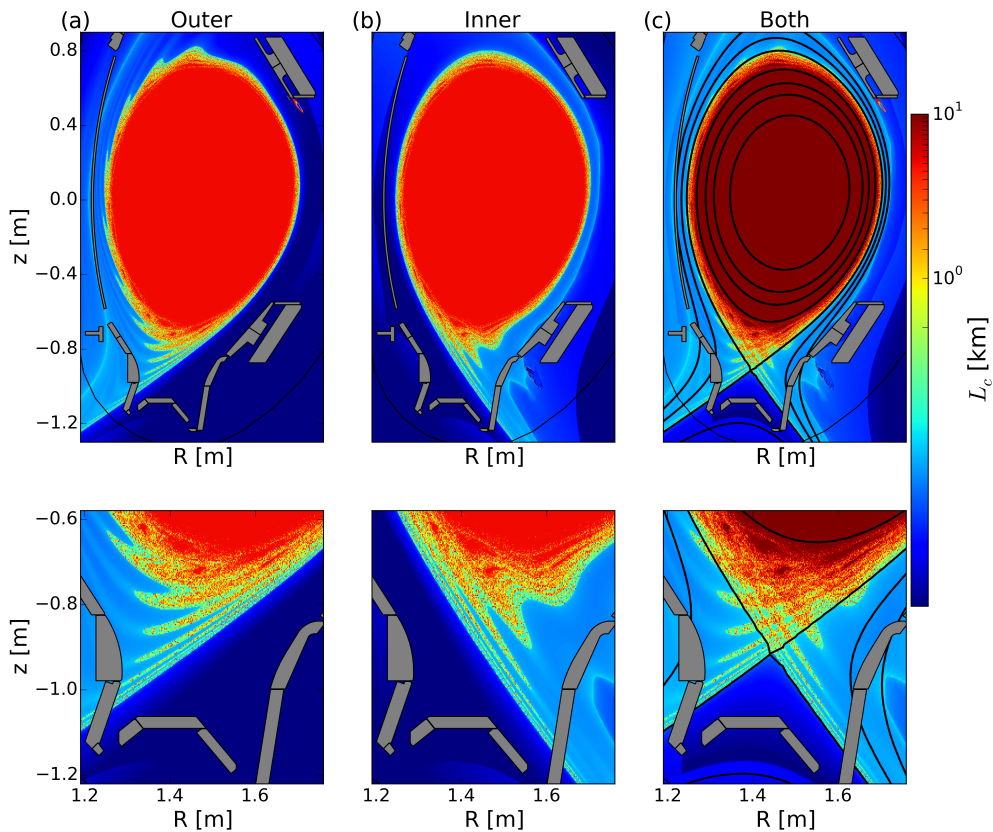


**Figure 4.8:** Connection length $L_c$ to the outer target (a), inner target target (b) and total connection length (c).

It is interesting to note, that when plotting the connection length in terms of the number of full poloidal turns $N_\theta$, as shown in Fig. 4.9a, a fractal structure is revealed. In this plot field lines with $N_\theta = 0$ connect the targets within less

than one full poloidal turn and field lines with $N_\theta = 1$ within one and two full poloidal turns, and so on. It can be seen that separated *basins* with equal $N_\theta$ are formed. Figure 4.9 (b) shows a zoomed-in view of the black framed box in (a), and (c) a zoomed-in view of the black framed box in (b). It can be seen that the basins in the lobe form a stripe pattern, and that stripes with $N_\theta = 1$ alternate with regions which have $N_\theta > 1$. In the stripes with $N_\theta > 1$ again alternating stripes with different $N_\theta$ can be found. This process continues to infinitely small scales, i.e. between any two stripes a set of finer scaled stripes is found. The boundary between two basins is therefore fractal in nature.
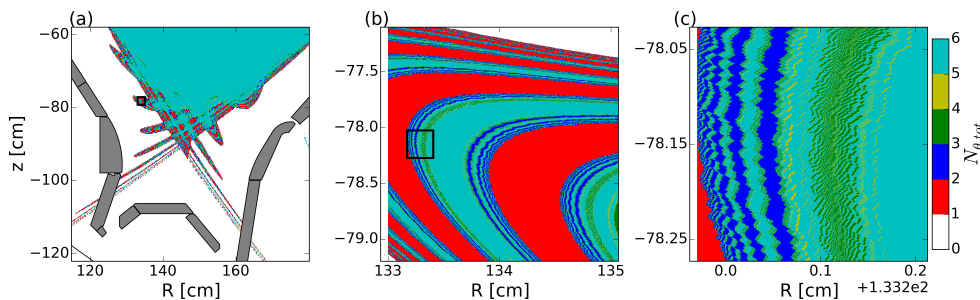


**Figure 4.9:** Number of integer poloidal turns $N_\theta$ within which a field line connects the inner and outer target. In (b) a zoomed-in view of the black framed box in (a), and in (c) a zoomed-in view of the black framed box in (b) is shown.

## 4.4 Screening of MP Fields

In the previous sections it has been assumed that the vacuum approach holds, i.e. the plasma creates no magnetic field in response to the applied perturbation field. A plasma is, however, a highly conducting medium and magnetic perturbations can induce currents in the plasma. According to Ampères law, these currents create a magnetic field and therefore $\vec{B}_{resp}$ cannot be assumed to vanish in (4.1).

In this section an ad-hoc plasma response model is discussed, which was proposed in [83]. It has also been confirmed by theoretical considerations [84] and a number of simulations which model the plasma response to MPs [74, 85–87], that such a screening effect should occur. A review of the Fitzpatrick theory, describing the screening of MP fields due to the plasma rotation is given in appendix A.

The model consists of the following assumptions:

1. The plasma response consists of surface currents which are localized at rational surfaces. The total perturbed plasma distribution can therefore be expressed by

$$\vec{j}(\psi, \theta, \phi) = \sum_i \delta(\psi - \psi_i)\vec{j}_i(\theta, \phi), \tag{4.13}$$

where $\delta$ denotes the delta function, and the index $i$ numerates the rational surfaces.

2. The currents $\vec{j}_i$ are parallel to the magnetic equilibrium field:

$$\vec{j}_i = j_i \frac{\vec{B}_{eq}}{|\vec{B}_{eq}|} \qquad (4.14)$$

3. The currents are divergence free

$$\vec{\nabla} \cdot \vec{j}_i = 0. \qquad (4.15)$$

By this assumption it follows that $\frac{j_i}{|\vec{B}_{eq}|}$ is constant along the field line. Therefore the Fourier expansion of $j_i$ includes only poloidal mode numbers with $m = q_i/n$, where $n$ is the toroidal mode number.

The first assumption is, according to (A.5), fulfilled if the gradient of the equilibrium current is small, so that $\frac{dj}{dr} \approx 0$. Furthermore, the width of the layer in which the current is flowing should be small compared to the plasma minor radius. By the second assumption it is ensured that the response field is perpendicular to the field lines. The third condition is necessary to avoid charge accumulation. We assume from now on that the toroidal spectrum consists only of one mode number $n_0$, and denote surfaces with $q = m/n_0$ by their poloidal mode number $m$. By combining assumptions 1–3, the current at the surface $m$ is given by

$$\vec{j}^m = \Re\left(I^m \delta(q - m/n_0)\exp[i(m\theta^* - n_0\phi)]\vec{B}_{eq}\right), \qquad (4.16)$$

where $I^m$ is a complex constant with physical unit [A/T], which determines the screening strength, and $\Re$ indicates that only the real part is taken. This current generates a (normalized) radial field component $b^{r,m}$, with a resonant Fourier component $b_m^{r,m}$ on the rational surface $m$.

The parameter $I^m$ is an ad-hoc parameter which determines the strength of the surface current. According to the discussion of Fig. A.1, if the unperturbed plasma rotation frequency is considerably above the critical value $\omega_c$, the mode is either almost fully suppressed at its resonant surface or it penetrates. Full suppression requires the resonant component of the total perturbation field to vanish, which determines $I^m$. For example, if screening at only one rational surface $m$ is assumed, $I^m$ is obtained by the following condition:

$$b_m^{r,m} = -b_m^{r,MP} \qquad (4.17)$$

When assuming screening on multiple rational surfaces $(m_1, m_2, ..., m_M)$, it has to be taken into account that each screening current creates resonant field components on the other rational surfaces. Therefore, on each surface $m_i, i = 1, ..., M$ the following condition has to be satisfied:

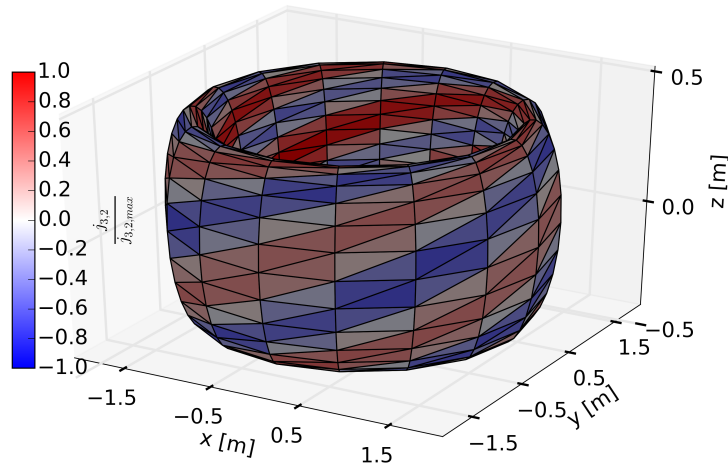$$\sum_{l=1,..,M} b_{m_i}^{r,m_l} = -b_{m_i}^{r,MP}, \qquad (4.18)$$

**Figure 4.10:** Triangularization of the (3,2) rational surface. For displaying reasons the number of triangles in the plot is lower than actually used in the computations. The color indicates the current direction and strength.

which constitutes a linear matrix equation with $M$ unknowns.

Numerically the sheet currents were implemented by a triangular discretization. The magnetic field generated by the current in each of the triangles can be computed analytically [88]. This approach avoids the problem of a diverging field near the screened surfaces which occurs when filaments are used for the discretization, as done in [83]. The triangularization for a (3,2) surface is visualized in Fig. 4.10.

To illustrate the effect of screening on the field topology the screening model was applied to the resonant case discussed in the last section. Two different sets of screening surfaces were chosen: In the first case only the $m = 3$ surface, and in the second case all rational surfaces between $m = 3$ and $m = 12$ were screened. The corresponding $m < 0$ part of the poloidal spectra are shown in Figs. 4.11b+c. The screened surfaces are here indicated by the magenta circles, and the non-screened surfaces by the green circles. For comparison in Fig. 4.11a the case with no screening is shown again. It can be clearly seen that 'holes' are created in the spectrum in the vicinity of the screened resonant components.

The bottom plots in Figs. 4.11a-c show the corresponding Poincaré plots in a $(\theta, \rho)$ coordinate system. The location of the screened surfaces are marked by the red lines. It can be seen that the islands at the screened surfaces vanish. Furthermore in Fig. 4.11c the stochastic region is limited by the last screened surface (i.e. $m = 12$).
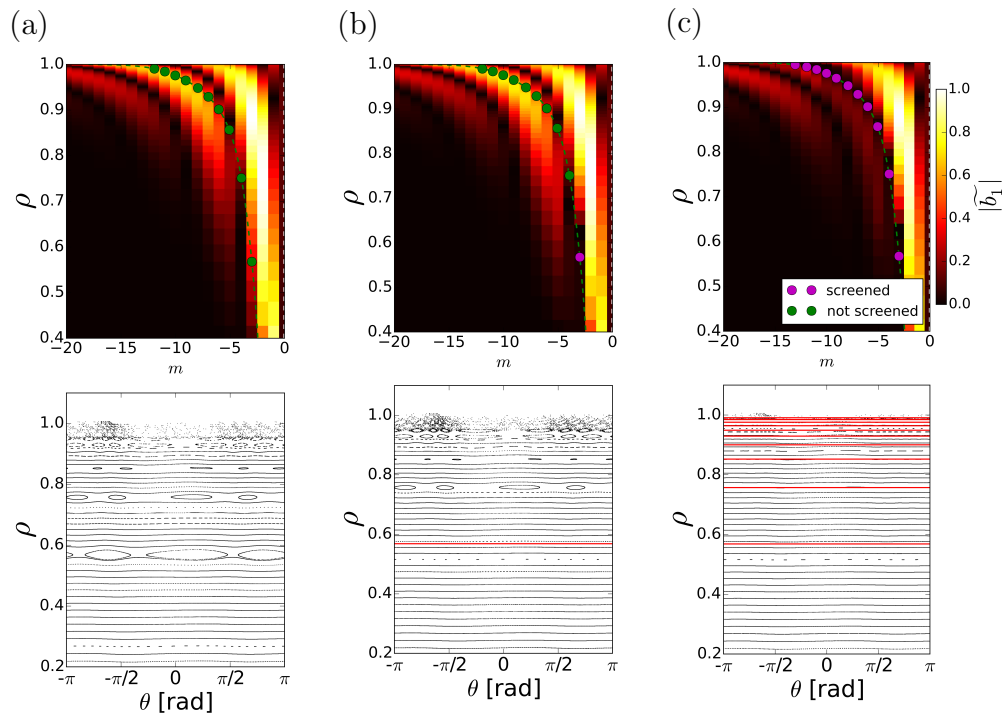
**Figure 4.11:** Poloidal spectrum without screening (a), with screening at the $m = 3$ surface (b) and with screening of all rational surfaces up to $m = 12$ (c). The red lines in (b) show the locations of the screened surfaces.

# Chapter 5

# Effect of MP Fields on the Power Decay Length with Consideration of Screening

In this chapter it will be discussed how MP fields affect power exhaust, and in particular the power decay length, in typical attached AUG L-mode discharges. L-mode discharges often allow for an easier interpretation of the experimental measurements compared to H-mode discharges, since they are ELM free, and the edge gradients of the plasma parameters are flatter. Attached conditions are chosen since the atomic physics effects are less complex in this regime. Moreover, attached conditions are characterized by a low divertor density. As discussed in chapter 2.5, high divertor densities lead to bremsstrahlung dominating the IR signal, whereas in attached conditions the contribution of bremsstrahlung is negligible, and so the divertor power fluxes can be measured more easily at high spatial resolution.

The effect of MP fields on the power decay length depends critically on the degree of screening of the MP field by the plasma. Therefore, in order to model the effect of MP fields on power exhaust, it it necessary to include screening effects correctly in the simulations. Hence, in this chapter it will be furthermore examined how strong the screening is for the discussed type of plasmas.

In section 5.1 the code EMC3-EIRENE, with which the simulations of discharges with MPs presented in this thesis were carried out, will be briefly described. As a first application of the code, simulations of a well diagnosed attached L-mode discharge will be shown. It will be seen that with screening currents a considerable better agreement between the simulations and the experiment can be achieved. In order to support the assumption of screening currents in the plasma a heat pulse experiment was carried out, which will be discussed in section 5.5. In the last section 5.6 of this chapter the effect of MP fields on the power decay length in EMC3-EIRENE simulations of AUG discharges with and without screening will be examined. It will be shown that

screening may explain that in AUG no significant increase of the power decay length can be obtained with MP fields. Finally, an estimation of the effect of MP fields on the power decay length in ITER will be given.

## 5.1   The 3D Transport Code EMC3-EIRENE

As was seen in the last chapter, MP coils lead to a complex 3D field structure. Most tokamak plasma transport codes, such as SOLPS [55] or EDGE2D [89], solve the plasma transport only in 2D. In contrast, the code EMC3-EIRENE, which was used in this thesis, solves the plasma transport equations in 3D. EMC3-EIRENE was originally developed to simulate the plasma transport in stellarators, which are intrinsically three-dimensional [90]. With the emergence of actively applied non-axisymmetric MP fields, EMC3-EIRENE has been increasingly used to model the transport in tokamaks, such as TEXTOR [91,92], DIII-D [81,93–95], NSTX [96] and AUG [97,98].

EMC3-EIRENE couples the plasma fluid transport code EMC3 to the kinetic neutral code EIRENE. A description of the physical models used by these codes can be found in appendix B. Both, EMC3 and EIRENE, apply a Monte-Carlo method to solve the underlying equations. While in EIRENE the Monte-Carlo particles, correspond to neutral particles, in EMC3 they represent discretized fluid quantities. For example, when solving the energy equation, they can be regarded as 'energy parcels'. By the resulting distribution of the Monte-Carlo particles the corresponding macroscopic quantities can then be obtained. The mathematical framework for this approach is described in [99].

In contrast to the above mentioned 2D codes, EMC3 allows to use grids which are not flux surface aligned, making it possible to solve the transport in the complex 3D topologies created by the MP field. Due to this flexibility of the grid, it is also possible to take into account the full 3D wall structure in the simulations [100]. Recently, EMC3-EIRENE has also been applied to toroidally axisymmetric problems with alternative divertor configuration [101], where the construction of the grid proved to be simpler than with 2D codes.

EMC3-EIRENE solves a modified set of the stationary *Braginskii equations* [54] for the plasma and a kinetic equation for the neutrals. The impurities are treated in a trace impurity approach, i.e. they only influence the background plasma via their radiation, but do not directly affect the particle or momentum balance. It should be noted that the code does currently not include drifts and volumetric recombination, which seem to be necessary to describe the detached divertor state in a tokamak [102]. This will become relevant in chapter 6, where detachment with MP fields in AUG will be discussed. However, the attached plasmas presented in this chapter could be modeled without taking these effects into account.

In the following a simplified workflow of an EMC3-EIRENE simulation, sketched in Fig. 5.1, will be described. First, based on the magnetic field, a grid is created. Figure 5.2 shows a typical EMC3-EIRENE grid with a toroidal extension
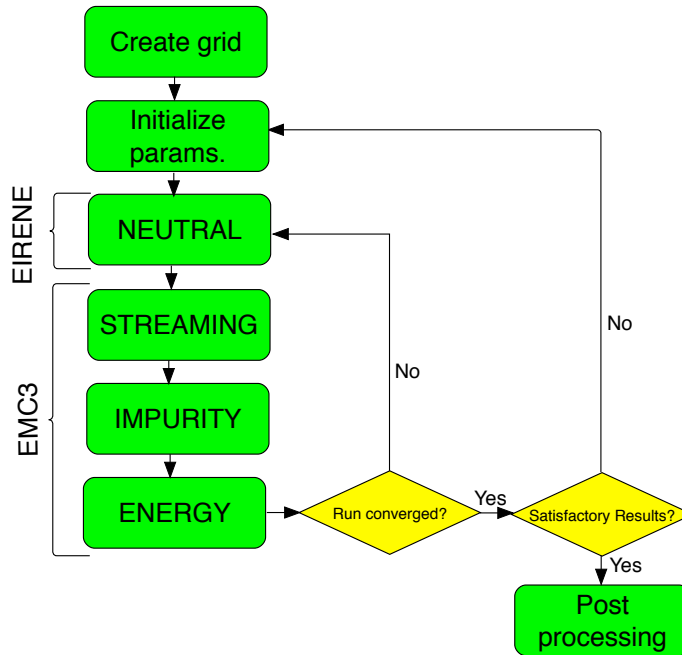
**Figure 5.1:** Simplified workflow diagram of an EMC3-EIRENE simulation.

of 180°. The purpose of this grid is twofold. First, the grid stores the magnetic field geometry. This also means that the magnetic field configuration is not influenced by the simulation results. From the grid points the magnetic field is then interpolated to the locations of the Monte-Carlo particles, which can be located anywhere between the grid points. The second purpose of the grid is to store the simulation results.
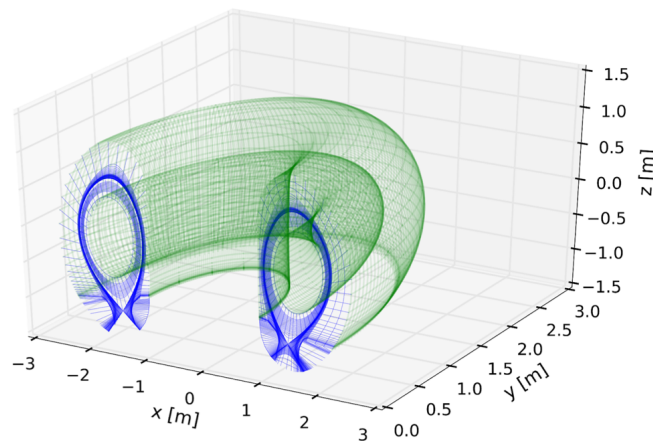


**Figure 5.2:** Grid of an EMC3-EIRENE simulation with a toroidal extension of 180°.

After the grid is created the simulation parameters are set. These include the net heating power $P_{net}$ entering the computational domain, the averaged

separatrix density $n_{sep}$, and perpendicular particle, and electron and ion heat diffusion coefficients $D_\perp, \chi_{e,\perp}$ and $\chi_{i,\perp}$. The perpendicular diffusion coefficients may also have a spatial dependence. The simulation is then started by running EIRENE which solves the equations for the neutral species. Subsequently the continuity and momentum equations (STREAMING), the impurity equation (IMPURITY) and the energy equation (ENERGY) are solved. The last three routines are part of the EMC3 code. The EMC3-EIRENE routines are called iteratively several times until a converged solution is reached, and subsequently it is verified that the solution is 'satisfactory'. This means, e.g., if a specific experiment is modeled that the simulation results agree with the experimentally determined boundary conditions. If there is no satisfactory solution the simulation parameters have to be adapted, and the simulation is continued again until it converges. If satisfactory simulation results are achieved, often further post-processing is performed, e.g. the simulation results are interpolated or extrapolated to points not belonging to the grid.

## 5.2 Discharge Setup and Experimental Heat Flux Pattern

Figure 5.3 shows time traces of selected experimental parameters of the AUG discharge #32217 analyzed in this section. A detailed analysis of the experimental heat flux measurements of the discharge discussed in the following can be found in [103].
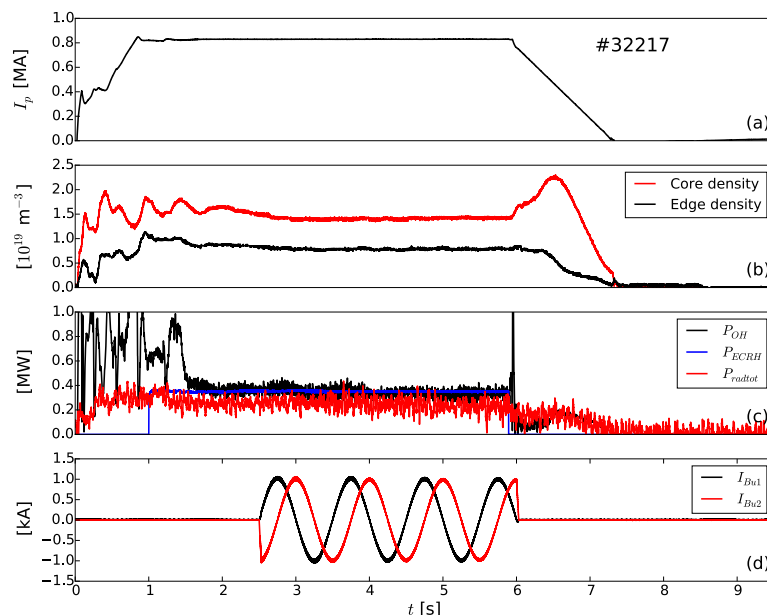


**Figure 5.3:** Time traces for the plasma current $I_p$ (a), core and edge densities (b), ohmic power $P_{OH}$, ECRH power $P_{ECRH}$ and total radiated power $P_{radtot}$ (c), and MP coil currents $I_{Bu1}$ and $I_{Bu2}$ (d).

In Figure 5.3a the toroidal plasma current $I_p$ is plotted, in Figure 5.3b the core and edge densities measured by the interferometry lines H-1 and H-5 (cf. also Fig. 2.5a and in Figure 5.3c the Ohmic heating power $P_{OH}$, the ECRH power $P_{ECRH}$, as well as the total radiation $P_{radtot}$. The plasma current is ramped up within the first second to a value of $I_p = 0.8$ MA. The density reaches a constant value after about 2 s, with $n_{H-5} \approx 0.7 \times 10^{19}\,\mathrm{m}^{-3}$, which is a relatively low value for these conditions. $P_{ECRH}$ and $P_{OH}$ are both about 0.4 MW. About half of the total heating power is radiated, as can be seen by the $P_{radtot}$ signal. The radiation occurs in this discharge predominantly in the core region, with only about $10\,\%$ radiated in the SOL.

The applied MP field was in an $n = 2$, $\Delta\varphi = -90°$ configuration, and hence, as discussed in chapter 4, it is resonant in the edge region. Figure 5.3d depicts the currents $I_{Bu1}$ and $I_{Bl1}$ in the upper and lower MP coils of sector one. Due to the alternating current in the coils the MP field rotates toroidally. Since the various diagnostics only measure at a fixed toroidal location, the rotation is necessary to measure the toroidal dependence of plasma parameters. This is effectively the same as rotating the various diagnostics, with a non-rotating MP field.
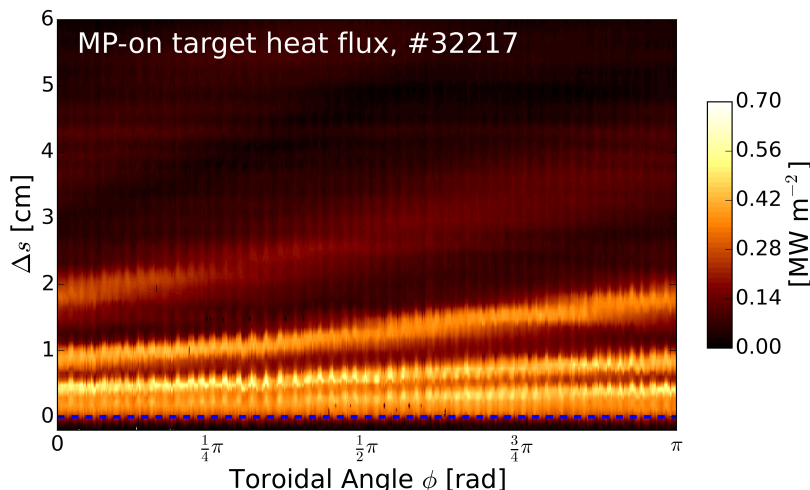


**Figure 5.4:** Outer target heat flux measured by thermography. $\phi$ is the toroidal angle and $\Delta s$ is the distance from the separatrix along the target. The fluctuations at about $50\,\mathrm{Hz}$ are due to sawtooth oscillations in the plasma center, which propagate to the target as heat pulses.

Figure 5.4 shows the heat flux which was measured with the IR camera in this discharge during the MP-on phase over one MP period between 2.8 and 3.8 s. The time $t$ was mapped here to a toroidal angle $\phi = \omega t + \phi_0$, where $\omega = \pi/[1\text{ s}]$, and $\phi_0$ is some offset. The heat flux exhibits fluctuations at a frequency of about $50\,\mathrm{Hz}$ in the range of $20\,\%$. These fluctuations, which are unrelated to the MP field, occur due to so called sawtooth oscillations, periodic instabilities in the plasma center which propagate towards the target as heat pulses [104].

The heat flux shows a stripe pattern, with the individual stripes moving helically away from the strike line location $s_0$ corresponding to the MP-off case. In contrast to the unperturbed case, where the heat flux profile has only one maximum which occurs near the strike line (see. e.g. Fig. 5.7), several maxima along $\Delta s$ at a fixed toroidal location can be seen. This effect is often called *strike line splitting*.

## 5.3 Simulation without MPs

For the simulation without MPs the separatrix density was set to $n_{sep} = 0.45 \times 10^{19}\,\mathrm{m}^{-3}$ and the net input power to $P_{net} = 0.25$ MW. The midplane profile of the perpendicular particle transport coefficient $D_\perp$ is depicted in Fig. 5.6a. The perpendicular heat diffusion coefficients $\chi_{e,\perp}$ and $\chi_{i,\perp}$ were spatially constant at the outer midplane, with $\chi_{e,\perp} = \chi_{i,\perp} = 0.35\,\mathrm{m}^2/\mathrm{s}$.
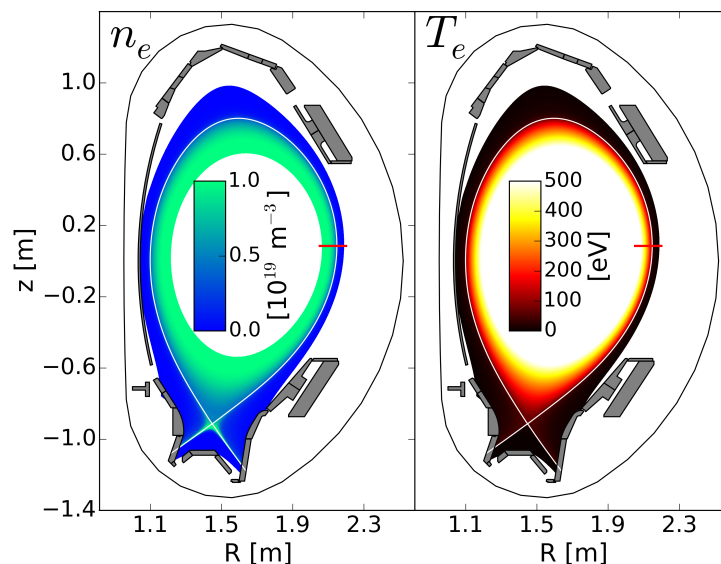


**Figure 5.5:** Cross-section of the EMC3-EIRENE simulation results of the AUG discharge #32217 at 2.4 s (MPs off) for the density $n_e$ (left) and temperature $T_e$ (right). The red line in (a) and (b) shows the outer midplane.

Figure 5.5 shows contour plots of the simulated density $n_e$ and temperature $T_e$, and in Figs. 5.6b+c the corresponding 1D upstream profiles along the red line in Fig. 5.5 are shown. Additionally, in Fig. 5.6b the experimental MP-off density profiles of #32217 obtained by the lithium beam and the core and edge Thomson scattering diagnostics are shown, while in (c) the $T_e$ profiles measured by the Thomson scattering and ECE diagnostics can be seen. For all experimental measurements only the median value within the interval indicated by the horizontal error bar is shown. The median value, rather than the mean value, is used to eliminate outliers. The vertical error bar is given by the standard deviation within each interval.

For the density a good agreement with the lithium beam data and the edge Thomson scattering was achieved for $\rho < 1.01$, while for $\rho > 1.01$ the measurements are overestimated. The simulated temperature follows closely the one measured by the edge Thomson scattering diagnostic. The ECE measurements are overestimated inside the separatrix by about 50 eV.
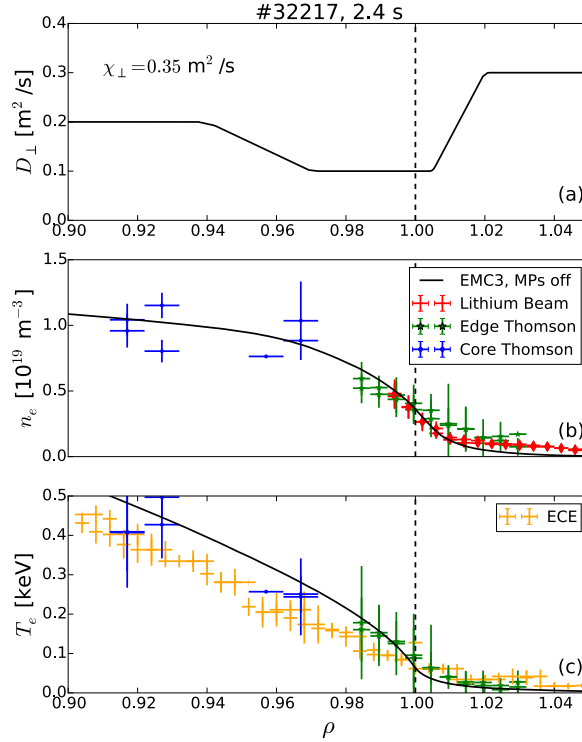


**Figure 5.6:** Midplane profile of the perpendicular particle transport coefficient $D_\perp$ chosen for the simulation of the AUG discharge #32217 at 2.4 s (a). The perpendicular heat diffusion coefficient was spatially constant at the outer midplane, with $\chi_\perp = 0.35 \, \mathrm{m^2/s}$. Outer midplane profiles for the density (b) and the electron temperature (c). The EMC3-EIRENE simulation results are shown by the black curves, while the symbols show experimental measurements.

Figure 5.7 shows the outer target heat flux profile measured by the IR system at 2.4 s, i.e. 0.1 s before the MPs are switched on. The EMC3 results are shown in blue again. By applying the fit function (3.25), for the IR profile a power decay length of $\lambda_q = 3.7$ mm and a divertor spreading factor of $S = 0.34$ mm was found. The simulated profile matches these values within 10 %, with $\lambda_q = 3.4$ mm and $S = 0.31$ mm.

## 5.4 Simulations with MPs

For the simulations with MP fields two different assumptions for the plasma response were made. In the first case, which will be denoted by 'vacuum case' in the following, no screening was taken into account, i.e. $\vec{B}_{resp} = 0$ in (4.1).
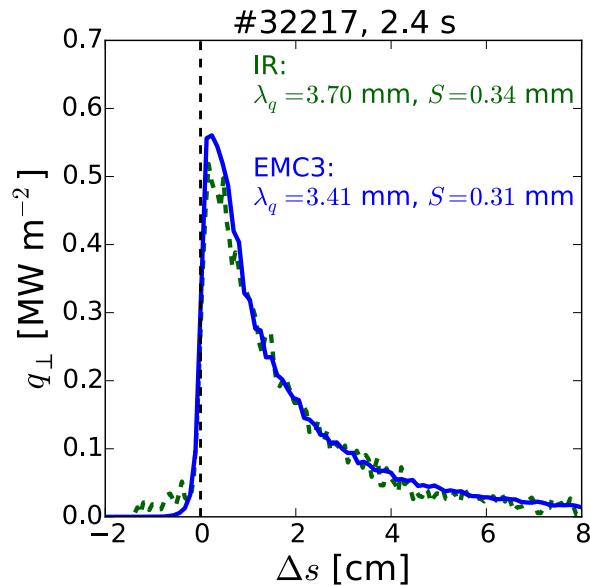
**Figure 5.7:** Simulated outer target heat flux profiles for the MP-off case (blue) and IR measurements (green) for the AUG discharge #32217 at 2.4 s.

In the second case, denoted by 'screened case' all $n = 2$ MP field components at resonant surfaces with safety factor $q \leq 5.5$ were ideally screened, where the radial position of the $q = 5.5$ surface was at $\rho = 0.98$. Moreover, in both cases the reduction of the MP field amplitude of about 30 % by the PSL due to the MP field rotation (cf. chapter 4) was taken into account.

In Fig. 5.8b the simulated upstream density (top) and temperature (bottom) profiles of the MP-off case (blue), the vacuum case (red) and the screened case (magenta) are shown. The dotted-dashed vertical lines indicate the locations of the resonant surfaces, where the corresponding safety factor $q$ is given at the top of the figures. In the simulations the vacuum case shows a reduction of the density by about $0.1 \times 10^{19} \, \text{m}^{-3}$ with respect to the MP-off case, i.e. by about 10 % at $\rho = 0.9$. The temperature is affected much more strongly, with a reduction of about 200 eV, or 30 %, at the inner simulation boundary at $\rho = 0.9$. We see therefore, that the stochastic field, if not shielded, leads to a considerable confinement degradation. Moreover, a staircase pattern can be seen, i.e. the profile flattens near resonant surfaces where islands lead to an increased radial heat transport. In the screened case the density essentially coincides with that of the MP-off case and the temperature is reduced by only about 25 eV. In other words screening is able to recover the confinement of the plasma. Moreover the screened case does not exhibit the staircase pattern, since the islands vanish, and does agree much better with the experimental profiles.

In Fig. 5.8a the experimental profiles for the MP-off case (black) are compared to those of the MP-on case (red). The MP-on profiles were averaged here over

one MP period from 4.5 to 5.5 s. It can be seen that the experimental MP-on profiles coincide with those of the MP-off case within the error bars. Moreover, no clear indication of a staircase profile can be seen in the measurements, which might, however, also be due to the finite spatial accuracy. This means that the simulation with screening leads to a better agreement with the experimental data, which is a strong indication for the existence of screening currents.
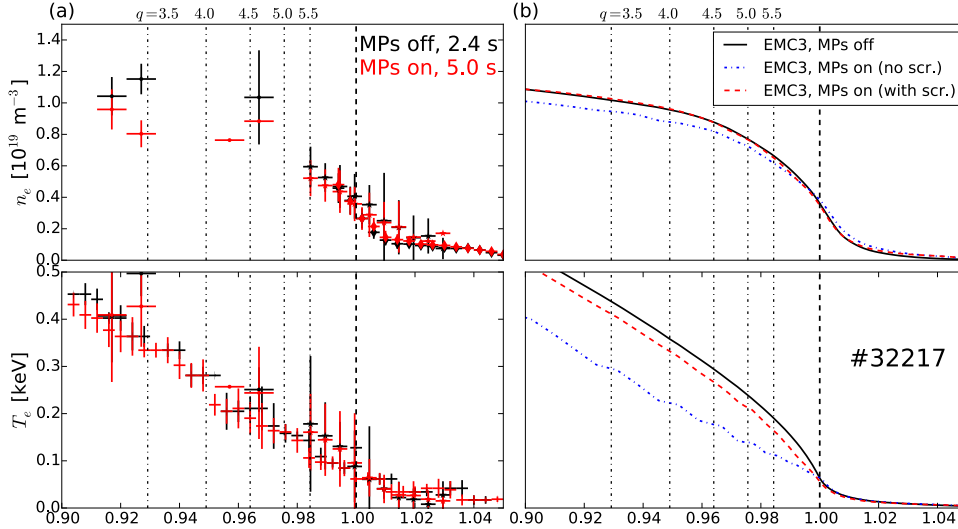


**Figure 5.8:** (a) Experimental outer midplane profiles for density (top) and temperature (bottom) without MP field (black) and with MP field (red). (b) Simulated outer midplane profiles for density (top) and temperature (bottom) for the MP-off (black), vacuum (blue) and screened (red) case. The location of the resonant surfaces is indicated by the vertical dotted-dashed lines, where the corresponding safety factor $q$ is given at the top of the plots.

Figure 5.9 shows 2D cross-sections of the electron temperature $T_e$ and density $n_e$ in the divertor region at the toroidal angle $\phi = 11.25°$ for the MP-off case (a), the vacuum approach case (b) and the screened case (c). As discussed in chapter 4, MPs lead to the formation of magnetic lobes in the SOL, which contain field lines connecting to radial locations with $\psi_N < 1$. Particularly in the vacuum case this magnetic structure is well reflected in the the density and the temperature distributions. For the screened case the magnetic lobes shorten radially and the lobe structures observed in $n_e$ and $T_e$ become correspondingly less pronounced.

In Fig. 5.10a the simulation results for the target heat flux for the vacuum case (top) and the screened case (bottom), and in (b) the corresponding outer target connection lengths can be seen. The intersection of the magnetic lobes with the target forms a helical structure, which is clearly seen in the heat flux pattern. Moreover, for the vacuum as well as the screened case, we obtain a qualitatively good agreement with the experimental heat flux shown in Fig. 5.4.

Since the magnetic lobes are shorter for the screened case, also the heat flux
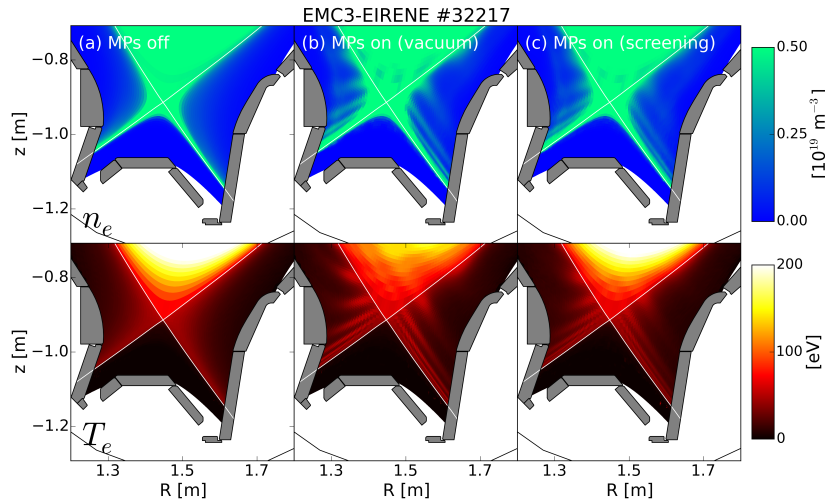
**Figure 5.9:** 2D cross-sections of the divertor region at $\phi \approx 11.25°$ of the simulated electron density $n_e$ (top) and temperature $T_e$ (bottom) for the MP-off (a), the vacuum case (b) and the screened case (c).

striation pattern becomes less pronounced. This can be seen more clearly in 1D profiles at fixed toroidal locations, as those shown in Fig. 5.11 for the toroidal angles $\phi = 0.25\pi$ (a), $0.5\pi$ (b) and $0.75\pi$ (c). The blue curves correspond to the vacuum case, the red ones to the screened case, and the green curves show the IR data.

Since the integral heat flux measured by the IR system fluctuates by about 20 %, all profiles have been normalized to the estimated total outer target heat flux

$$P_{tot}(\phi) \equiv 2\pi R \int q_\perp(s, \phi)\mathrm{d}s, \tag{5.1}$$

where $\mathrm{d}s$ is a line element along the target coordinate, and $R$ the major radius. Since the heat flux is toroidally non-axisymmetric, this estimation has in general a dependence on the toroidal angle $\phi$. At all three toroidal locations the screened case profile is smoother than the one of the vacuum case. Comparing the simulations to the IR measurements it can be seen that for $\Delta s > 2$ cm, the vacuum case overestimates the heat flux measured in the lobe structures, while the screened case yields a good agreement. However, for $\Delta s < 2$ cm, it cannot be unambiguously determined whether the vacuum or the screened case agrees better, due to the following reasons: 1) The spatial dimensions of the strike line splitting are of the order of the spatial resolution of the IR measurements. 2) The fluctuations of the heat flux measured by the IR might also change $\lambda_q$. 3) The surfaces properties are not perfectly homogeneous, leading to local 'hot spots' on the target, where the heat flux is overestimated.

A more quantitative comparison between the simulations and the IR data can be made by analyzing the toroidally averaged heat flux profiles. The toroidally averaged IR data for the MP-on phase between 2.8 and 3.8 s is shown in Fig. 5.12a by the red curve. For comparison the MP-off heat flux, already
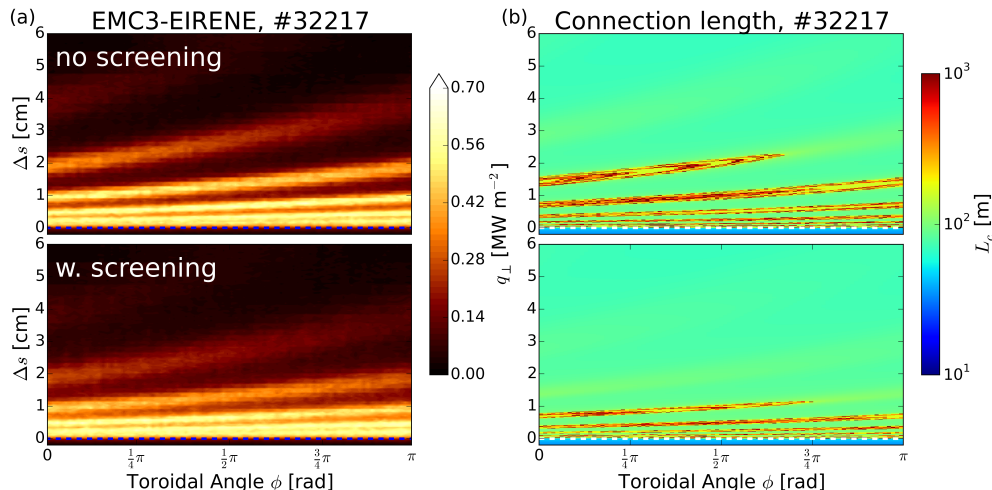
60

**Figure 5.10:** Simulated outer target heat flux pattern (a) and connection length plot (b) for the vacuum (top), and the screened case (bottom).

shown in Fig. 5.7, is plotted in black. Here the data has been normalized to the maximum heat flux. In (b) the toroidally averaged and normalized simulated heat fluxes of the vacuum and screened cases are shown in blue and red. The simulated MP-off case is shown again in black. The experimental as well as the simulated toroidally averaged heat flux profiles can again be well described by (3.25), i.e. they can be parametrized by a divertor spreading factor $S$ and a power decay length $\lambda_q$, as already found in [103]. We obtain for the experimental toroidally averaged MP-on profile a power decay length of $\bar{\lambda}_q^{on} = 3.5$ mm and a divertor spreading factor of $\bar{S}^{on} = 0.35$ mm, i.e. both agree with the experimental MP-off values within 10 %. A deviation of this order is within the typical error of the fit. In the simulations, for the vacuum case $\bar{\lambda}_q^{on} = 4.2$ mm and $\bar{S}^{on} = 0.31$ mm, and for the screened case $\bar{\lambda}_q^{on} = 3.74$ mm and $\bar{S}^{on} = 0.31$ mm were found. We have therefore an increase of $\lambda_q$ by about 10 % for the screened and 25 % for the vacuum case with respect to the MP-off profile. Again, this is an indication for the existence of screening currents.

Hence, although the 2D heat flux pattern with MP field is non-axisymmetric and deviates strongly from the MP-off profile, the toroidally averaged heat flux profiles agree in the experiment, and also in the simulation if screening currents are included.

## 5.5 Further Evidence of Screening by Heat Pulse Experiment

In the previous section it was shown that, to reproduce the experimental discharge results in the simulation, screening currents had to be included. To
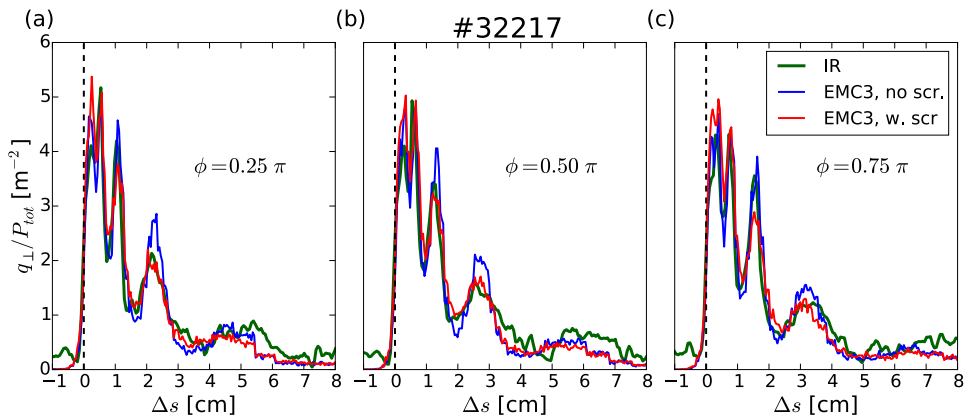
**Figure 5.11:** Experimental outer target heat flux profiles (green), and simulated heat flux profiles without screening (blue), and with screening (red) at the toroidal angles $\phi = 0.25\pi$ (a), $0.5\pi$ (b) and $0.75\pi$ (c).
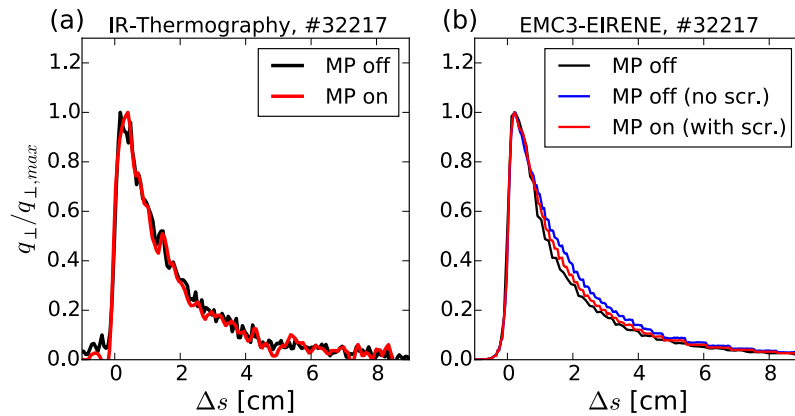


**Figure 5.12:** (a) Experimental MP-off (black) and toroidally averaged MP-on (red) outer target heat flux profiles. (b) Simulated MP-off (black), and toroidally averaged heat flux profiles for the vacuum (blue) and screened (red) case.

corroborate the indications for this screening effect, a dedicated experiment was carried out in AUG, which relied on the deposition of heat pulses in the plasma edge. Heat pulse experiments are an established method to study the energy transport and have already been conducted in various devices to study stochastic fields [105].

Typically, in experiments of this kind localized Electron Cyclotron Resonance Heating (ECRH) with a modulation frequency of about 40 Hz is applied, which leads to a modulation of the electron temperature. The Fourier analysis of the upstream temperature profiles with respect to time allows to obtain information about the transport properties [106]. However, to achieve reliable results with this method a high relative spatial accuracy and a low fluctuation level of the upstream profiles are required, which is not given in the edge region of AUG where stochasticity is expected.

**Figure 5.13:** Connection length plots for the vacuum case (a) and the strongly screened case (b). The ECRH pulse beam trace is shown in yellow, and the flux surface marked white, at $\rho = 0.95$, shows the radial location of the ECRH pulse deposition.
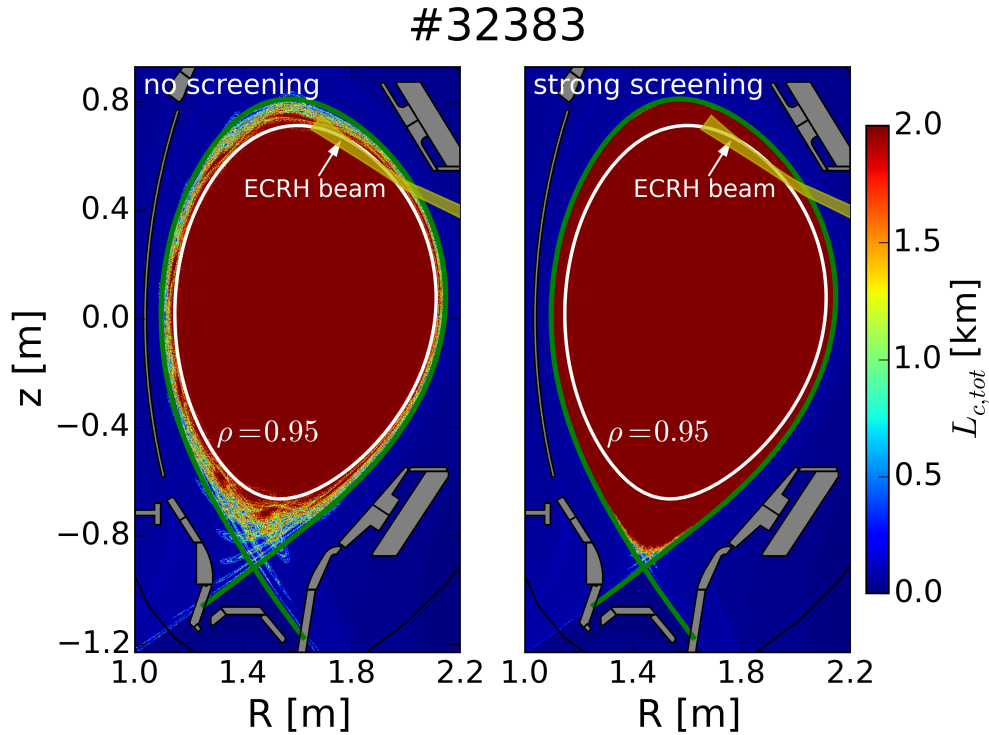
In the experiment presented in this chapter a different approach was used, where heat pulses are deposited in the edge region and the heat flux propagation speed is estimated from the time delay between the heat pulse deposition and the resulting transient heat flux increase at the target measured by the IR system and the Langmuir probes. The measured time differences depend on the spatially averaged transport properties in the edge region. Therefore, this method avoids the problems associated with measuring spatially resolved upstream profiles.

In Fig. 5.13 connection length plots for the vacuum case (a) and a case with strong screening (b) are shown. The trace of the ECRH beam, calculated by the beam tracing code TORBEAM [107], is shown in yellow. The flux surface corresponding to the ECRH pulse absorption location at $\rho = 0.95$ is marked in white. For the vacuum case this flux surface is near to the stochastic region, while in the screened case the stochastic region is limited to a narrow layer near $\rho = 1$. In the stochastic region the radial transport is increased due to the high parallel heat conductivity, i.e. the heat pulse propagation time decreases. Therefore, for the vacuum case a decrease of the propagation time with respect to the MP-off case is expected, while in the strongly screened case the propagation time should be similar to the one of the MP-off case. Hence, it can be assumed that if strong screening occurs, the target heat flux

measurements of the MP-off and on cases show a similar time behavior. As will be discussed in section 5.5.2, this assumption is also confirmed by EMC3-EIRENE simulations, modeling the heat pulse transport.

### 5.5.1 Experimental Setup and Measurements

Selected time traces of the discharge #32383 discussed in this section can be seen in Fig. 5.14. The toroidal magnetic field was $B_t = -2.5$ T, the plasma current $I_p = 1.0$ MA and the edge safety factor $q_{95} = 4.0$. The central electron density $n_{H-1}$ was feedback controlled to $3.7 \times 10^{19}$ m$^{-3}$, i.e. the density was more than twice that of the low density discharge #32217 discussed in the last section. However, the density was still low enough in order to have an attached divertor, with electron temperatures of about 25 eV at the outer target. From
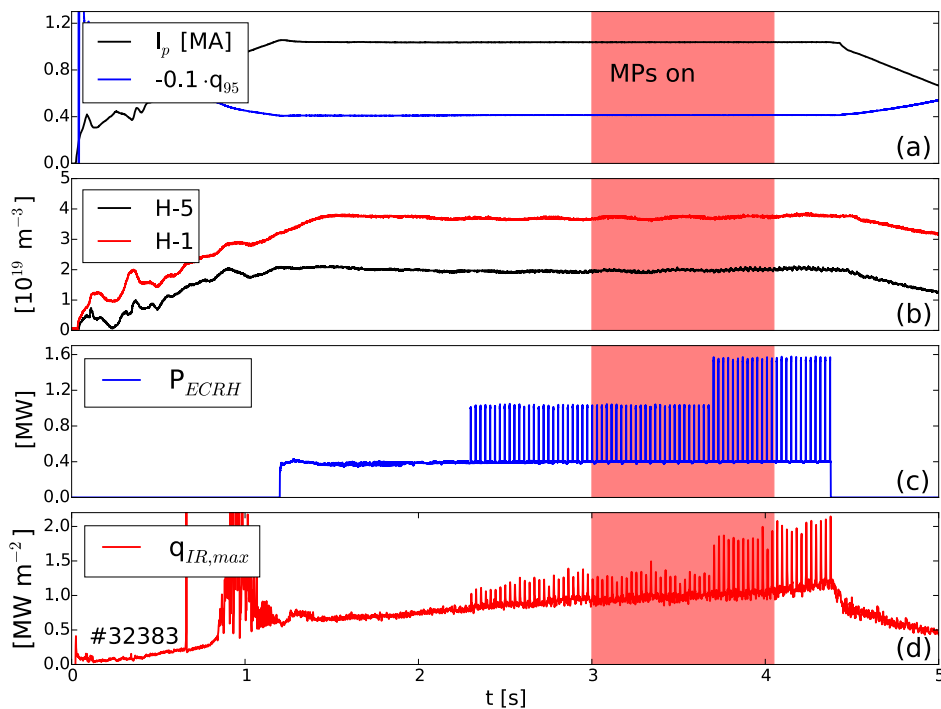


**Figure 5.14:** Selected time traces of the AUG discharge #32383: plasma current $I_p$ and edge safety factor $q_{95}$ (a), core and edge densities $n_{H-1}$ and $n_{H-5}$ (b), ECRH heating power $P_{ECRH}$ (c) and maximum outer target heat flux measured by the IR system (d).

1.2 s on temporally constant central ECRH heating of 0.4 MW was applied, and on top of that ECRH pulses with 0.6 MW deposited in the edge region at $\rho \approx 0.95$ from 2.3 s on. The pulse duration was about 2 ms and the period time 26 ms. At 3.7 s the ECRH pulse power was increased to 1.2 MW. From 3.0 to 4.0 s an MP field with a toroidal mode number of $n = 2$ and a differential phase of $\Delta\varphi = 90°$ was applied.

In contrast to #32217 the MP field was not rotated, which means that no 2D target heat flux pattern could be measured. A static MP field has, however, the advantage that it is not attenuated by the PSL. Figure 5.14d shows the time trace of the peak heat flux measured by the IR system. It can be clearly seen that each heat pulse leads to a distinct increase of the target heat flux.
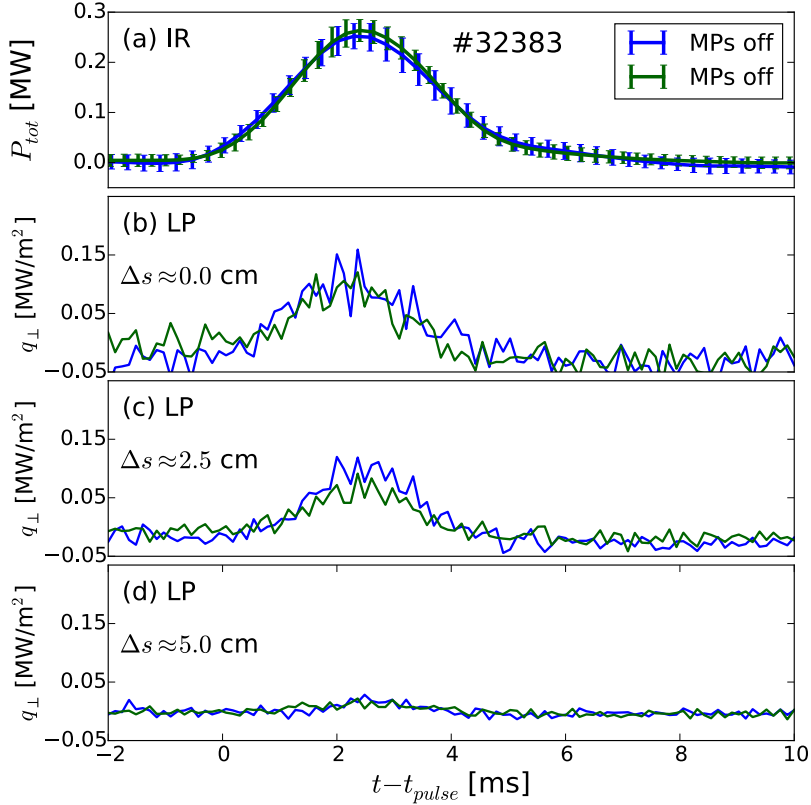


**Figure 5.15:** (a) Conditionally averaged estimated total heat flux after the heat pulse deposition from the IR camera at $\phi \approx 214°$. (b–d) Outer divertor heat flux obtained from Langmuir probes (LP) at $\phi \approx 168°$. In all plots a constant background heat flux was subtracted.

Figure 5.15a shows the estimated total heat flux $P_{tot}$ at the outer target after a heat pulse as a function of time $t$ for the MP-off and MP-on cases. Here $P_{tot}$ is given by (5.1), where $q_{\perp}$ is the heat flux conditionally averaged over several heat pulse periods. It can be seen that, except for a constant background which was subtracted, $P_{tot}$ coincides for the MP-on and MP-off cases within the error bars.

The heat pulses could also be observed in the heat flux measured by the outer divertor target triple Langmuir probes (LP) at $\phi \approx 168°$ with a time resolution of about 35 µs (Figs. 5.15b–d). The probe data confirms the IR data, showing no significant difference between the MP-on and the MP-off case.

## 5.5.2 EMC3-EIRENE Simulations

As discussed in section 5.1, EMC3-EIRENE solves the stationary plasma transport equations, whereas the transport of a heat pulse is a time dependent problem. Therefore, in order to simulate the transport of the heat pulse with EMC3-EIRENE, this functionality had to be implemented in the code in the course of this work. However, instead of solving the time dependent transport equations in a fully self-consistent way, only the time dependent energy transport equation was solved, while the background plasma parameters were kept constant. This approach is justified by the assumption that the perturbation of the background plasma is small compared to the equilibrium parameters. Similar to the approach used in chapter 5, first the background plasma for an MP-off time point was simulated. Using the same input and transport parameters as in the MP-off case, the MP-on cases were then simulated. Here three different plasma response scenarios were considered: no screening (vacuum), moderate screening and strong screening. For the moderate and strong screening scenarios all rational surfaces within $\rho = 0.97$ and $\rho = 0.996$ were screened, respectively. Technically, the solution of the heat pulse transport
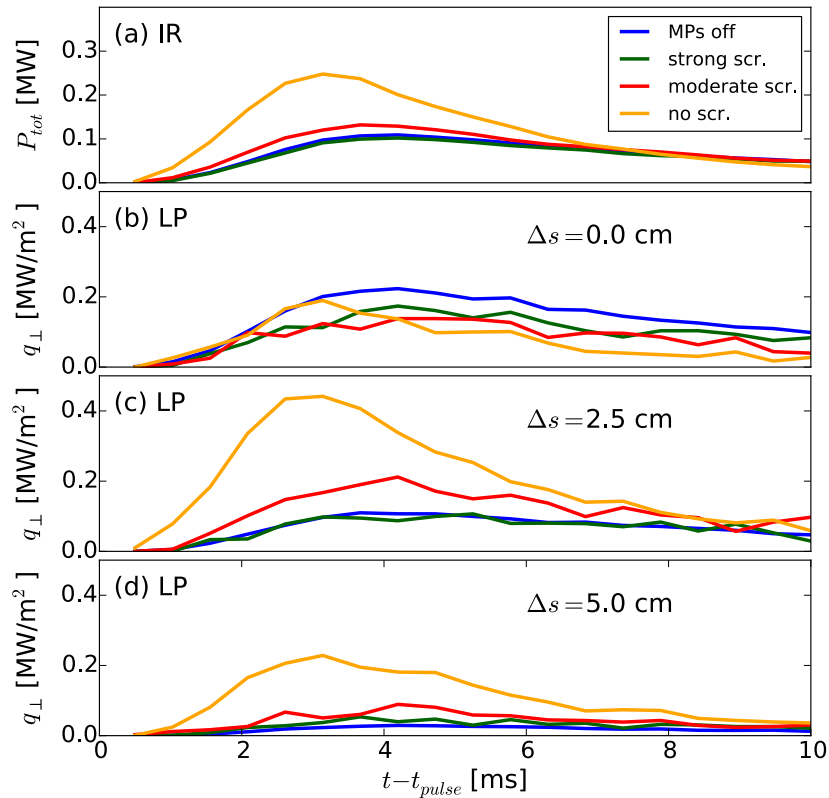


**Figure 5.16:** (a) Simulation results of the poloidally integrated outer target heat flux $P_{tot}^{sim}$ at $\phi \approx 214°$ after the heat pulse deposition. (b–d) Simulated heat flux after the heat pulse deposition at different target locations at $\phi \approx 160°$ at the approximate probe locations shown in Fig. 5.15.

was implemented by initializing energy Monte-Carlo particles at the ECRH pulse deposition surface and tracing them until they hit one of the targets. The time interval between the initialization and the deposition at the target $t_{int}$, as well as the deposition location at the target were then recorded. To take into account the finite ECRH pulse length of 2 ms, a random uniformly distributed time between 0 and 2 ms was added to the $t_{int}$ of each particle.

Figure 5.16a shows the simulated outer target total heat fluxes $P_{tot}^{sim}$ as a function of time for the MP-off case and the three MP-on cases. Here $P_{tot}^{sim}$ is defined analogously to the experiment, see (5.1). With screening the confinement increases compared to the vacuum case and as a result the duration of the heat pulse deposition increases and the maximum of $P_{tot}^{sim}$ decreases. With strong screening $P_{tot}^{sim}$ approaches the MP-off solution, as also observed in the experiment (see Fig. 5.15a).

Figure 5.16 depicts the heat pulse deposition flux at three different positions along the target at $\phi \approx 160°$ in dependence of time. The $\Delta s$ locations in this plot were chosen to be approximately the same as those of the probes shown in Figs. 5.15b–d. In the simulations it can be seen that particularly at the outer two locations the heat flux for the vacuum case is considerably higher than for the MP-off case. In contrast, the heat flux measured by the Langmuir probes is at all locations similar for the MP-off and on cases.

In conclusion, the simulations confirm that without screening the propagation time of the heat flux decreases. Moreover, the simulations show that without screening the maximum of $P_{tot}^{sim}$, and the local heat flux at the outer two probe locations increases. In the experiment none of these observations was made, which supports the conclusion made in section 5, that the MP field is strongly screened.

x

## 5.6 Effect of MPs on the power decay length $\lambda_q$ and Implications for ITER

In section 5.3 it was shown that MP fields can lead to an increase of the power decay length $\lambda_q$ in the simulations. As discussed in the introduction of this thesis a large $\lambda_q$ is desirable, in order to decrease the peak heat flux. The idea of increasing the effective perpendicular transport with the help of stochastic fields is the basis of the *ergodic divertor*, which was investigated e.g. in the tokamaks TEXTOR [108, 109] and Tore Supra [110, 111]. In contrast to the MP field in AUG, the MP fields in these tokamaks were specifically designed to decrease the target peak heat flux.

In this section it will be systematically analyzed if a significant increase of $\lambda_q$ can be achieved with MP fields in EMC3-EIRENE simulations of AUG plasmas, and under which conditions such an increase occurs. It will be seen that the effect on $\lambda_q$, depends mainly on the MP field geometry and the unperturbed

fall off length $\lambda_q^{off}$.

In order to investigate the effect of MP fields on $\lambda_q$ three sets of simulations with different MP field configurations were carried out:

1. A (non-rotating) vacuum MP field $B_{vac}$.

2. The vacuum MP field $B_{vac}$ with screening taken into account.

3. The doubled vacuum MP field $2B_{vac}$ without screening.

The fact that the field is non-rotating means that no attenuation of the MP field by the PSL was present. The third MP field configuration is incompatible with the electromagnetic force limits of the coils and is therefore not a realistic scenario in AUG. For each MP field configuration a set of simulations was carried out, where in each simulation the (spatially constant) perpendicular particle and heat diffusion coefficients $D_\perp$ and $\chi_\perp$ were varied, in order to change $\lambda_q^{off}$. The input power $P_{net} = 0.4$ MW, the separatrix density $n_{sep} = 1.0 \times 10^{19}$ m$^{-3}$ and the ratio $D_\perp/\chi_\perp = 1/4$ were kept constant. The perpendicular transport coefficients and the resulting $\lambda_q^{off}$ values are listed in table 5.1.

| parameter set | 1 | 2 | 3 | 4 | 5 |
|---|---|---|---|---|---|
| $D_\perp$ [m$^2$/s] | 0.3 | 0.5 | 0.75 | 1.0 | 1.5 |
| $\chi_\perp$ [m$^2$/s] | 1.2 | 2.0 | 3.0 | 4.0 | 6.0 |
| $\lambda_q^{off}$ [mm] | 2.1 | 3.1 | 4.1 | 5.0 | 6.6 |

**Table 5.1:** Table of perpendicular particle and heat transport coefficients $D_\perp$ and $\chi_\perp$ assumed for the simulations shown in Fig. 5.18, and resulting power decay length $\lambda_q^{off}$ without MPs.

Figure 5.17 shows as an example the toroidally averaged outer target heat flux profiles for the MP-off case (blue), the screened case (magenta), the vacuum case (red) and the doubled vacuum case (green) for the transport parameter set 2 from table 5.1. A clear decrease of the peak heat flux can be seen with increasing MP field strength. Furthermore, each toroidally averaged heat flux profile can again be fitted by formula (3.25) (cf. section 5.4), which is shown by the dashed curves.

In Fig. 5.18a the ratio of the toroidally averaged power decay length with, $\bar{\lambda}_q^{on}$, and the one without MP field, $\lambda_q^{off}$, for all sets is plotted in dependence of $\lambda_q^{off}$ for all three MP field configurations. In all simulations an increase of $\lambda_q$ is observed with MP fields. This increase is strongly dependent on the MP field strength and $\lambda_q^{off}$. Generally $\bar{\lambda}_q^{on}/\lambda_q^{off}$ increases for decreasing $\lambda_q^{off}$ and increasing MP field strength. The lowest $\lambda_q$ values which are achieved in AUG in L-mode are around 3 mm, where one would expect an increase of $\lambda_q$ by 50 % due to the MP field if no screening is taken into account. With the screening scenario used here, this value reduces to about 20 %. For the hypothetical scenario with doubled vacuum MP field, an increase by about 150 % was achieved in
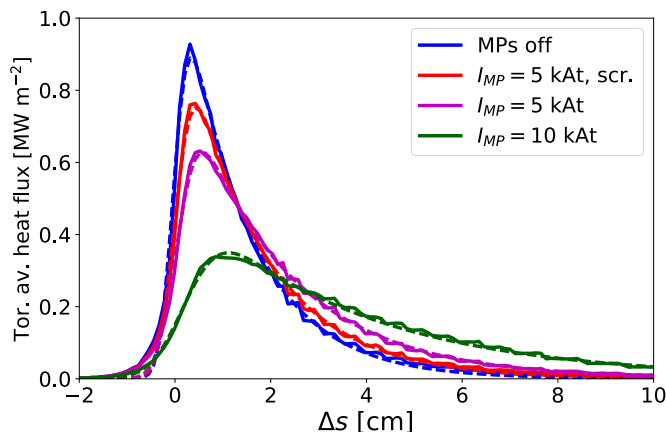
**Figure 5.17:** Outer target heat flux profiles for the MP-off case (blue), the screened case (red), the vacuum case (magenta) and the doubled vacuum case (green) for the parameter set 2 of table 5.1.

the simulations. The trends observed for $\bar{\lambda}_q^{on}$ can also be observed for the toroidally averaged integral power decay length $\bar{\lambda}_{int}^{on} = \bar{\lambda}_q^{on} + 1.64\bar{S}^{on}$, as can be seen in Fig. 5.18b, where the ratio $\bar{\lambda}_{int}^{on}/\lambda_{int}^{off}$ is plotted.

The dependence of $\bar{\lambda}_q^{on}$ on $\lambda_q^{off}$ and the MP field can be captured by a heuristic model presented in the following. We assume that heat is carried parallel to the field lines from inside the unperturbed separatrix into the magnetic lobes. The lobes have a typical extension of $\Delta w$ on the target, which increases with higher MP field strengths. Additionally we have to take into account the perpendicular diffusion in the SOL, which is parametrized by $\lambda_q^{off}$. The effective power decay length with MP field will therefore be given by

$$\bar{\lambda}_q^{on} = \sqrt{\lambda_q^{off2} + \Delta w^2}. \tag{5.2}$$

Equation (5.2) was fitted to the curves in Figs. 5.18a+b with $\Delta w$ as a fitting parameter. The fit function, represented by the continuous lines, describes the data very well.

The heuristic argumentation for the fit function (5.2) suggests that $\Delta w$ is approximately proportional to the maximum extension $s_{lobe}$ (see Fig. 5.19) of the magnetic lobe structures on the target

$$\Delta w = \frac{\alpha s_{lobe}}{f_x} \tag{5.3}$$

Here the factor $f_x = 4.5$ takes into account the integral flux expansion from the outer midplane to the target. The values for $s_{lobe}$ were evaluated to be 1.95, 3.4 and 8.2 cm for the screened, the vacuum, and the doubled vacuum case, as can be seen in Fig. 5.19 For all simulations the value of $\alpha$ was between 0.4 and 0.5 for the fits of $\bar{\lambda}_q^{on}$, and between 0.55 and 0.65 for the fits of $\bar{\lambda}_{int}^{on}$.
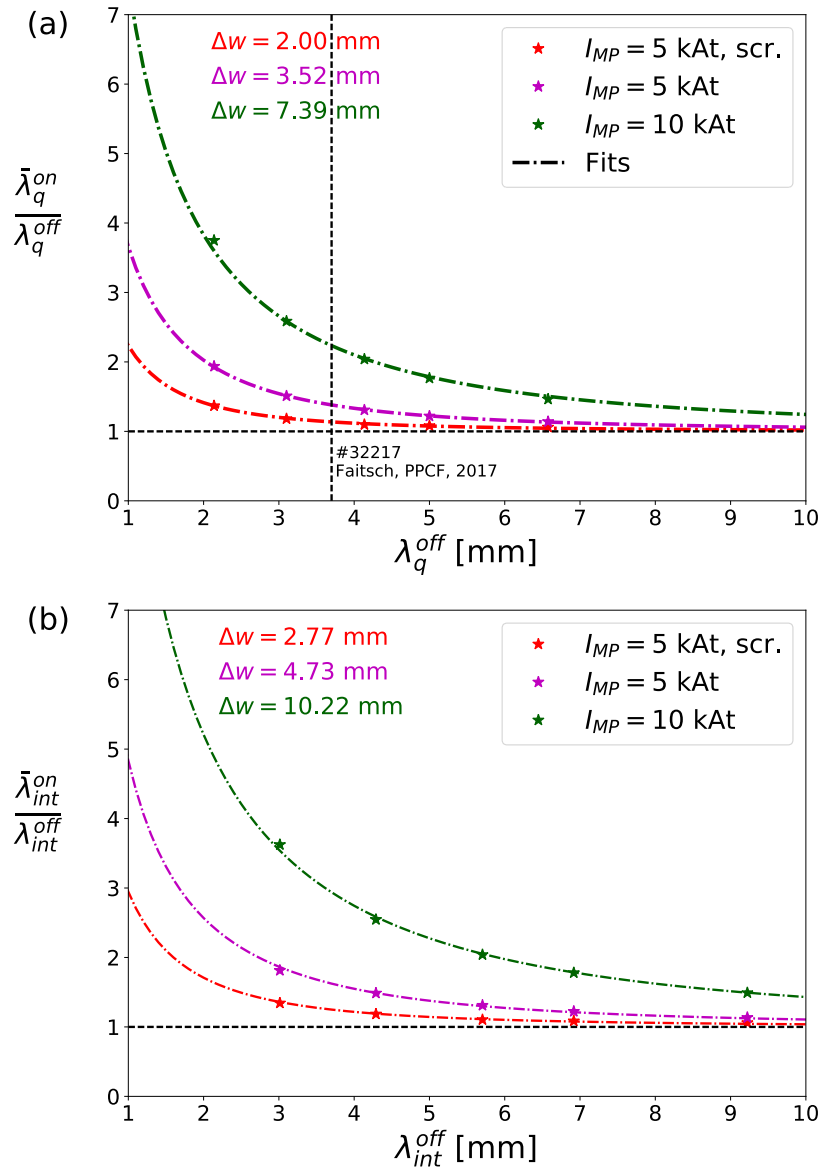
**Figure 5.18:** (a) Ratio of MP-on and MP-off power decay lengths $\bar{\lambda}_q^{on}$ and $\lambda_q^{off}$ in dependence of $\lambda_q^{off}$ for the screened case (red), the vacuum case (magenta) and the doubled vacuum case (green). The transport coefficients assumed to obtain the different values of $\lambda_q^{off}$ are shown in table 5.1. The vertical line at $\lambda_q^{off} = 3.7$ mm marks the experimentally measured MP-off power decay length of discharge #32217. (b) Same representation for the ratio of MP-on and MP-off integral power decay lengths $\bar{\lambda}_{int}^{on}$ and $\lambda_{int}^{off}$ in dependence of $\lambda_{int}^{off}$.

The experimental MP-off power decay length of $\lambda_q^{off} = 3.7$ mm measured in #32217 is marked by the vertical line in Fig. 5.18. From Fig. 5.18 an increase of the toroidally averaged $\lambda_q$ by about 40 % in the vacuum case, and about 15 % in the screened case would be expected. Additionally it has to be taken into account that the MP field was rigidly rotated with 1 Hz in #32217, and the field strength was therefore reduced further by 30 %. Therefore the fact that
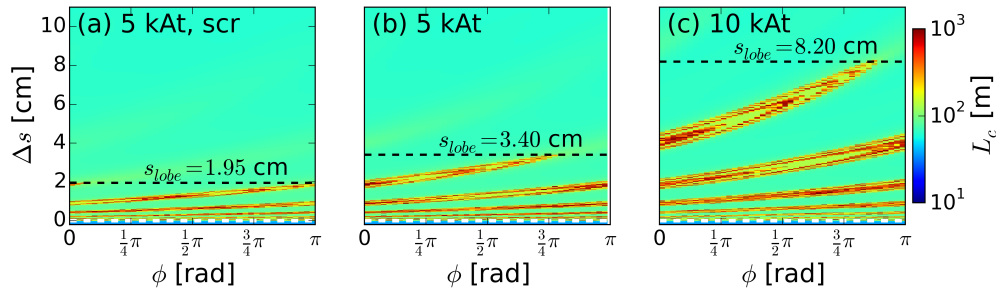
**Figure 5.19:** Target connection length plots for the screened case (a), the vacuum case (b), and the doubled vacuum field case (c). The horizontal dashed lines show the maximum extension $s_{lobe}$ of the magnetic footprints.

no increase of $\lambda_q$ was measured within the error bars for this scenario is well in line with the results of this section if screening is taken into account. For large $\lambda_q^{off} > 8$ mm, even with a vacuum approach only a small increase of $\lambda_q$ by about 10 % is expected with MPs. This explains why in the AUG simulations described in [97], where $\lambda_q^{off}$ was of that order, the MP-off and MP-on target peak heat fluxes were approximately the same, although a vacuum approach was used.

In ITER $s_{lobe}$ is expected to be larger than in AUG, while $\lambda_q^{off}$ is predicted to be approximately the same [112]. In Fig. 5.20 the fit was applied to an ITER case discussed in [113]. No screening was taken into account here, however the MP coil current of 45 kA corresponds to only half of the maximum current in ITER. The assumptions $s_{lobe} = 10$ cm, $f_x = 7.5$ and $\alpha = 0.2$ were used. The lower value of $\alpha$ with respect to the AUG simulations shown before, had to be chosen in order to match the simulation results in [113]. The dashed vertical line at $\lambda_q^{off} = 4$ mm shows the MP-off power decay length obtained in the simulations in [113]. Here the fit predicts an increase of $\lambda_q$ by about 20 %. However, at $\lambda_q^{off} = 1$ mm, which is predicted for ITER by the scaling in [112], an increase by about 300 % would be expected.

## 5.7 Conclusions

In this chapter the effect of MP fields on power exhaust and the target heat flux in typical AUG L-mode discharges has been examined. For this it was crucial, to know the degree of screening of the MP field by the plasma. To investigate these topics, detailed comparisons between EMC3-EIRENE simulations and experiments were made.

It was shown that without MP fields a reasonable agreement of divertor heat flux profiles from EMC3-EIRENE simulations and measurements of low density attached L-mode plasmas can be obtained, if the transport parameters are chosen appropriately. For the simulations with MP fields it was assumed that the transport parameters are not changed by the MP field. With this
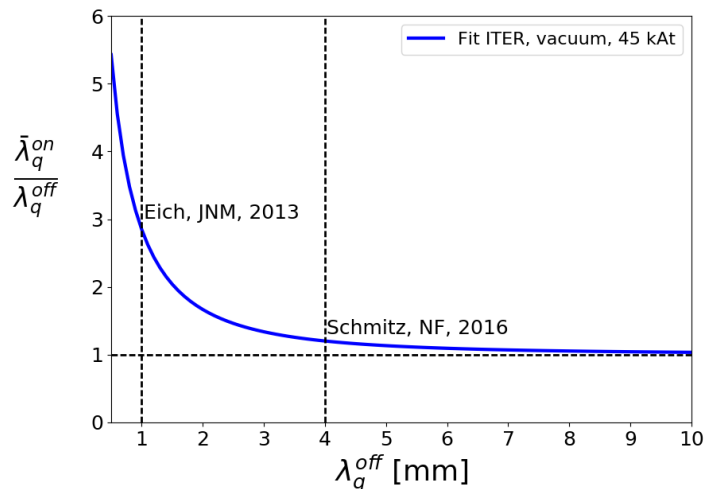
**Figure 5.20:** Ratio of MP-on and MP-off power decay lengths $\bar{\lambda}_q^{on}$ and $\lambda_q^{off}$ in dependence of $\lambda_q^{off}$ predicted by the fit function (5.2) for the vacuum 45 kAt case discussed in [113]. The assumptions $s_{lobe} = 10$ cm, $\alpha = 0.2$ and $f_x = 7.5$ were used in the fit.

assumption the vacuum approach led to a decrease of the plasma temperature by about 30 % at the inner simulation boundary with respect to the MP-off case. In contrast, the experimental temperature profiles of the MP-on and MP-off cases agreed within the error bars. With screening currents the simulated MP-on upstream profiles approached those of the MP-off case, i.e. it was possible to recover the confinement of the MP-off case.

Moreover, it was shown that in the experiment, as well as in the simulations, a striation pattern of the heat flux can be observed on the target and a qualitatively and quantitatively good agreement was obtained between the simulated and experimental heat flux. Furthermore, the vacuum case shows a more pronounced striation pattern than the screened case. Although the heat flux of the screened case yields a better agreement with the experimental heat flux in the far SOL, i.e. for $\Delta s \gtrsim 2$ cm, it was not definitely possible to decide on the basis of the striation pattern if screening is present in the experiment, which was partly due to measurement uncertainties.

A more reliable approach to determine if screening is present is to compare toroidally averaged heat flux profiles. These can again be fitted by the function (3.25), by which a power decay length is obtained. In the EMC3-EIRENE simulations the thus obtained power decay length with MP fields, is larger than the MP-off power decay length. For the vacuum case the power decay length was about 25 % larger, and for the screened case 10 %. For the measurement of the power decay length an error bar of about 10 % is estimated, which is compatible with the simulation including screening but not with the one for the vacuum approach. This is therefore another indication for the presence of screening currents.

The result that the MP field is screened was further corroborated by a heat pulse experiment. ECRH pulses were deposited in the edge region of the plasma, where a stochastic region would be expected if the MP field is unscreened. Due to this stochastic region, the heat pulse propagation time towards the target should decrease with respect to the MP-off case if no screening occurs. However, the time behavior of the target heat flux measurements with and without MPs was approximately the same. To model this experiment EMC3-EIRENE was modified in order to simulate the time dependent transport of heat on a constant plasma background. As expected, in the simulations without screening the heat pulse propagation time decreased, and the maximum heat flux in the far SOL increased considerably. Again, the experimental measurements could only be reproduced with screening.

In the last section of this chapter a systematic study of the effect of MP fields on the power decay length in EMC3-EIRENE simulations of typical AUG L-mode discharges was carried out. The simulations showed that with screening no significant increase of the power decay length can be achieved under the considered plasma conditions, in line with the experimental observations. However, in ITER the length of the magnetic footprints will be considerably larger than in AUG. Therefore, compared to AUG, a larger effect on the power decay length might be possible. An estimation, assuming half the maximum MP coil current, and no screening, resulted in an increase of 300 % of the power decay length in ITER.

Although the toroidally averaged peak heat flux might be lowered with MPs in ITER, due to the lobe structures the local heat flux could still be higher than without MPs which could be impedimental to reach detachment. This will be the topic of the next chapter, where detachment experiments with MPs in AUG will be discussed.

# Chapter 6

# Heat Flux Pattern in Detached Discharges with Magnetic Perturbation Fields

The discharges considered so far in this work have all been conducted under attached conditions. As was seen in chapter 5, for these cases MPs can lead to a heat flux which is locally higher than without non-axisymmetric perturbations. This is illustrated in Fig. 6.1a, where the heat flux without (MPs off) and with MPs (MPs on) for an attached case is sketched. In this section the question will be addressed if detachment with MPs occurs uniformly along the target, or if a *burn through* occurs, i.e. locally attached regions remain. This is illustrated in Fig. 6.1b, where the solid line shows the qualitative heat flux distribution for a detached MP-off case and the dashed line the corresponding hypothesized MP-on heat flux profile exhibiting a burn through. Such a scenario might be expected if the volumetric power dissipation has a strong non-linear dependence on the temperature, with considerably lower power losses in the hot and low-density regions. If the heat flux is toroidally strongly non-axisymmetric, measures for mitigating the local heat load, such as rotating the MP field, might become necessary. An understanding of the heat flux with MPs under high-recycling and detached conditions is therefore of great practical importance for a future fusion device in which MPs are applied to mitigate or suppress ELMs.

To investigate detachment with MP fields a number of deuterium L- and H-mode discharges have been carried out in AUG for this work. This chapter discusses the experimental results, as well as their interpretation with the help of modeling. The L-mode discharges, and their comparison to EMC3-EIRENE simulations as well as a simplified model based on field line tracing and diffusion will be presented in section 6.1. Section 6.2 discusses the heat flux pattern for ELM-mitigated high density H-mode plasmas with MP fields, and section **??** the nitrogen radiation distribution in these plasmas. Finally the results are summarized in section 6.4.
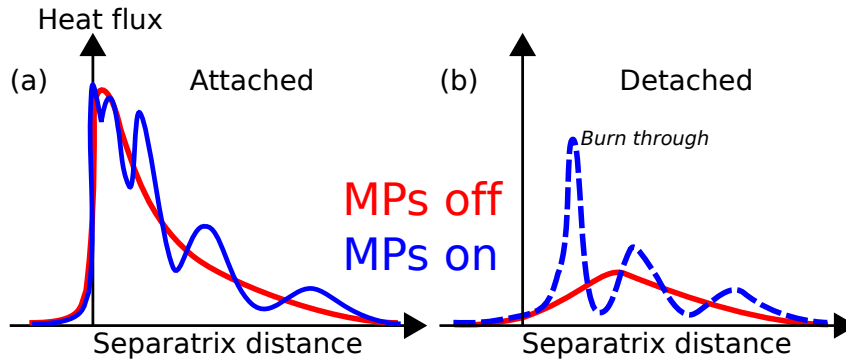
**Figure 6.1:** Illustration of hypothesized burn through effect: Qualitative heat flux profiles for attached (a) and detached (b) conditions with (on) and without (off) MPs.

## 6.1 L-mode Detachment Experiments with Magnetic Perturbation Fields

### 6.1.1 Experimental Setup

In the L-mode discharges presented in this chapter detachment was reached by increasing the density gradually (cf. section 3.4). As an example, Fig. 6.2 shows time traces of the discharge #32922. The toroidal magnetic field at the magnetic axis was $B_t = -2.5$ T. The plasma current and the safety factor, which are shown in Fig. 6.2a, were $I_p = 0.8$ MA and $q_{95} \approx 5.0$, respectively. In Fig. 6.2b the deuterium gas puff $\Phi_{D_2}$ can be seen. From 2.0 s on $\Phi_{D_2}$ was linearly increased from 0.35 to $20 \times 10^{21}\, e$/s. The line integrated edge density $n_{edge}$ (Fig. 6.2c), measured along the interferometry LOS H-5, increases during that phase from 1.1 to $3.2 \times 10^{19}\, \mathrm{m}^{-3}$. In Fig. 6.2d the ECRH power $P_{ECRH}$, the Ohmic heating power $P_{OH}$ and the total radiated power $P_{radtot}$ measured by bolometry are plotted. Figure 6.2e shows the $T_{div}$ signal, which is derived from the divertor shunt currents and serves as a proxi for the average outer target temperature [114]. In contrast to a temperature, however, this quantity can also become negative [115, 116], which indicates strong detachment.

Figure 6.2f shows the upper and lower MP coil currents $I_{Bu1}$ and $I_{Bl1}$ in sector 1. From 1.5 s on an MP field with a toroidal mode number $n = 2$ and differential phase difference $\Delta\varphi = -90°$ between upper and lower coil currents were switched on. The MP field was rotated rigidly with a rotation frequency of 5 Hz, to enable the measurement of the full toroidal heat flux profile. It can therefore be ensured that the toroidal heat flux maximum at each probe position is obtained. The high toroidal rotation frequency was chosen to ensure that the plasma parameters do not change significantly during one full toroidal MP field rotation.
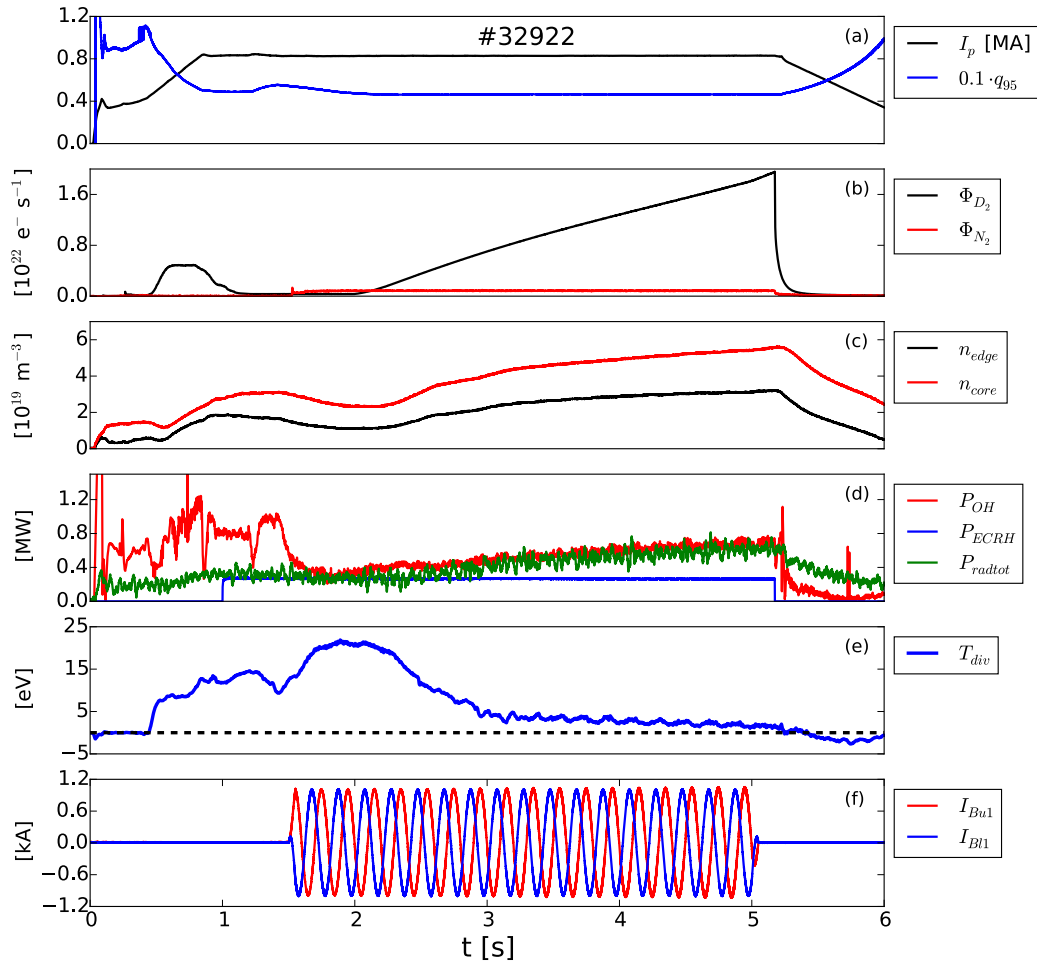
**Figure 6.2:** Time traces of plasma current $I_p$ and safety factor $q_{95}$ (a), deuterium and nitrogen puff rates $\Phi_{D2}$ and $\Phi_{N2}$ (b), line integrated edge and core densities $n_{edge}$ and $n_{core}$ (c), heating and total radiation (d), $T_{div}$ signal derived from the divert shunt current (e), and MP coil currents $I_{Bu1}$ and $I_{Bl1}$ (f) for the L-mode deuterium density ramp discharge #32922.

## 6.1.2 Divertor Heat Fluxes

Figure 6.3a shows the line integrated edge density time traces of the L-mode density ramps in discharges #32921 (MP-off, red) and #32922 (MP-on, blue). The corresponding time traces of the heat flux measurements of four adjacent Langmuir probes at the outer divertor can be seen in Fig. 6.3b-e. Here the heat flux was evaluated by the method described in section 2.6. For the MP-off as well as the MP-on case it is found that the triple Langmuir probe temperature measurement becomes unreliable as the temperature drops below 5 eV. The reason of the erroneous temperature measurements might be the decreasing electron mean free path as the temperature decreases [117, 118]. This leads to a decrease of the electron saturation current $j_{sat}^e$ and the assumption that $j_{sat}^e \gg j_{sat}$, under which the temperature is derived from the

triple probe measurements, is not fulfilled anymore. The triple probes can then yield unphysically high values for $T_e$ [119]. The time ranges where the measured temperature is believed to be unreliable are indicated by the gray shaded regions in Fig. 6.3b-e.

However, for low temperatures the heat flux (2.21) is dominated by $q_{rec}$ and the heat flux does not depend strongly on the temperature. We can therefore assume a constant temperature in the gray shaded regions in Fig. 6.3 without introducing a large error. Here the choice $T_e = 2.5$ eV was made, which is suggested by the divertor temperature derived from the shunt currents for $t > 3.0$ s (Fig. 6.2e). At the end of this section it will be argued that the assumption of a constant $T_e$ does not affect the results strongly.

Before discussing the MP-on case, the characteristics of the MP-off case will be briefly described. A detailed discussion of detachment in this kind of discharges at AUG can be found in [120]. Before 2.6 s the strike line position is not stationary, which may explain the decrease and subsequent increase of the heat flux in Fig. 6.3b. From 2.6 s on the divertor detaches near the strike line and the heat flux decreases. As the density is increased further, detachment extends outwards and from 3.2 s on the heat flux is decreasing at all probe positions.

In the MP-on case the same trends as for the MP-off case can be seen, but with an additional oscillatory modulation of the heat flux due to the rotating lobes that pass the probe positions. While at the strike line these oscillations are small, they become more pronounced towards the far SOL. As the heat flux decreases, the oscillation amplitude decreases as well at all probe locations. The running mean heat fluxes in the MP-on case $\langle q_{\perp,LP}^{on} \rangle$, with an averaging interval of one MP period (i.e. 0.2 s) are shown by the blue dashed lines. These follow closely the MP-off heat fluxes, showing that the MPs do not significantly affect the time averaged values.

The oscillatory nature of the heat fluxes can be seen even more clearly in Fig. 6.4b-e, where the relative deviation $\delta_q$ from the mean value is plotted. Here $\delta_q$ is defined as

$$\delta_q \equiv \frac{q_{\perp,LP}^{on} - \langle q_{\perp,LP}^{on} \rangle}{\langle q_{\perp,LP}^{on} \rangle} \tag{6.1}$$

Figure 6.4a shows the line integrated edge density of the MP-off case (#32921) and Fig. 6.4f the upper MP coil current $I_{Bu1}$ in sector 1. We concentrate from now on on the time period $t > 3.0$ s, where clear oscillations can be seen and the averaged heat fluxes change on a slow time scale compared to the MP period. $\delta_q$ varies strongest at the position of the outermost probe, with amplitudes as large as about 50 % around 3.0 s. Furthermore, $\delta_q$ tapers off at all four probe locations as the density increases, and the largest amplitudes observed towards the end of the discharge are around 20 %. In other words the oscillation amplitude decreases faster than the average heat flux.

It should be kept in mind that a constant temperature of $T_e = 2.5$ eV was assumed in the calculation of $\delta_q$, and therefore the oscillation of the temperature
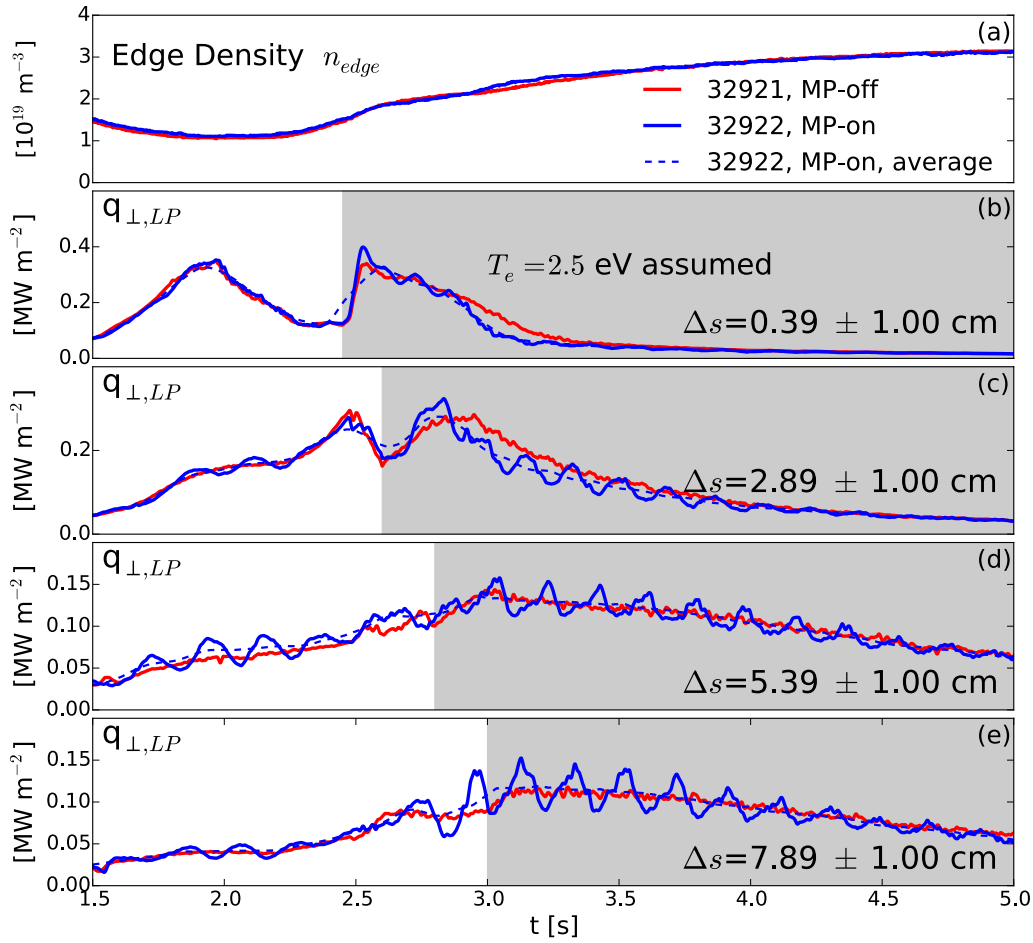
**Figure 6.3:** Line integrated edge density $n_{edge}$ (a) and outer target heat flux obtained by triple Langmuir probe measurements at several separatrix distances $\Delta s$ (b-e) for the MP-off case (red) and the MP-on case (blue). In the gray shaded regions $T_e = 2.5$ eV was assumed.

was not taken into account in the probe data evaluation. From (2.21) we can estimate the error introduced by this assumption as

$$\Delta \delta_q = \frac{\gamma_t \tilde{T}_e}{\gamma_t T_e + E_{rec}}. \tag{6.2}$$

Here $\tilde{T}_e$ is the amplitude of the temperature oscillations, which we can estimate from the variations of the $T_{div}$ signal as $\tilde{T}_e \approx 0.5$ eV. At $T_e = 2.5$ eV, $R_E = 0.55$ (see. Fig. 2.7) we get $\gamma_t \approx 4.4$ from (2.22). We obtain therefore $\Delta \delta_q \approx 10$ %, which is considerably lower than the largest heat flux amplitudes observed of $50\,\%$ .

79
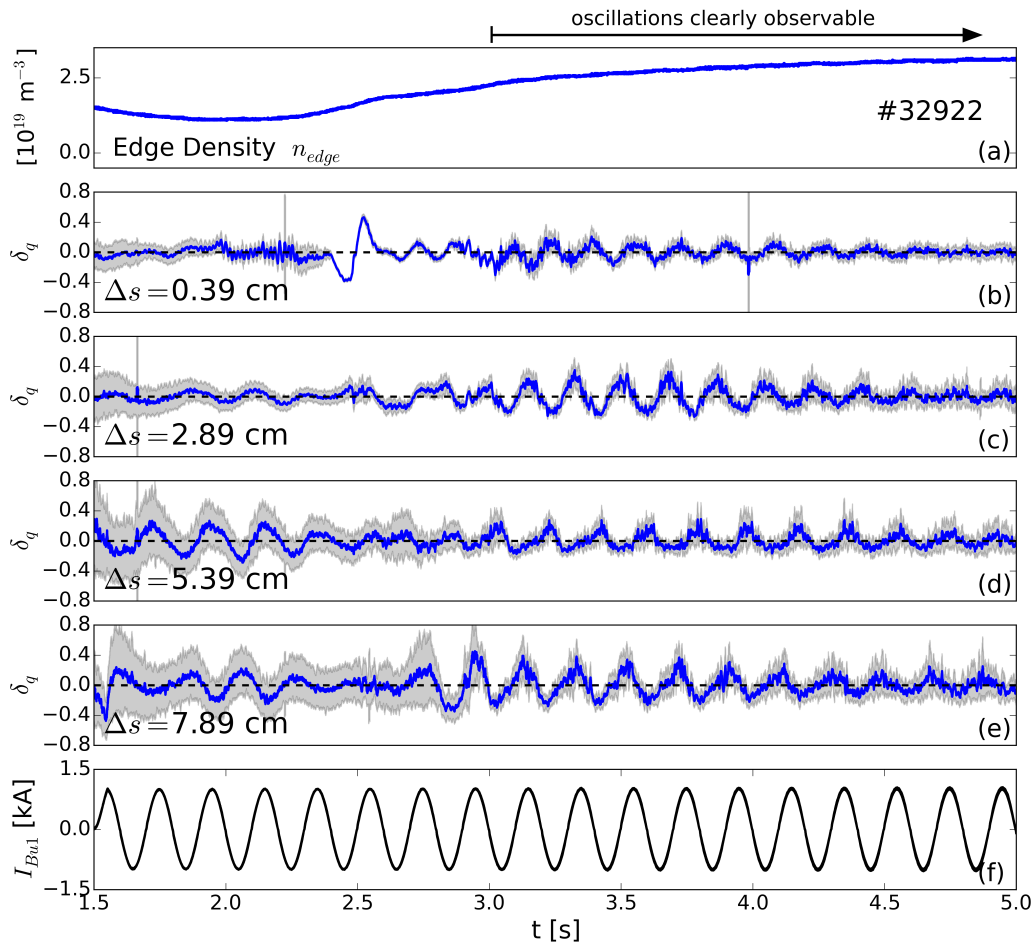
**Figure 6.4:** Line integrated edge density $n_{edge}$ of the MP-on discharge #32922, and relative oscillations $\delta_q$ of the outer target heat flux measurements shown in Fig. 6.3b-e. In (f) the current $I_{Bu1}$ of the upper MP coil in sector 1 is shown.

### 6.1.3 Comparison of the L-Mode Density Ramp Experiments to EMC3-EIRENE Simulations

To interpret the results presented in the last section the time points 3.1 and 4.1 s of both the discharges #32921 (MPs off) and #32922 (MPs on) were simulated with EMC3-EIRENE. The time point at 3.1 s will be referred to as 'medium density' and the one at 4.1 s as 'high density' case in the following. In Figs. 6.5a and b the simulated MP-off heat (top) and particle flux (bottom) profiles are shown for these two cases. The corresponding probe measurements are shown by the black symbols.

The simulation input parameters were chosen such, that a satisfactory agreement with the heat flux measurements was obtained. The respective net input powers and recycling fluxes were $P_{net} = 0.5$ MW and $\Phi_r = 6.6 \times 10^{22}\,e$/s for the medium density, and $P_{net} = 0.4$ MW and $\Phi_r = 4.0 \times 10^{22}\,e$/s for the high density case. The diffusion coefficients for particles $D_\perp$ and ion and electron

80

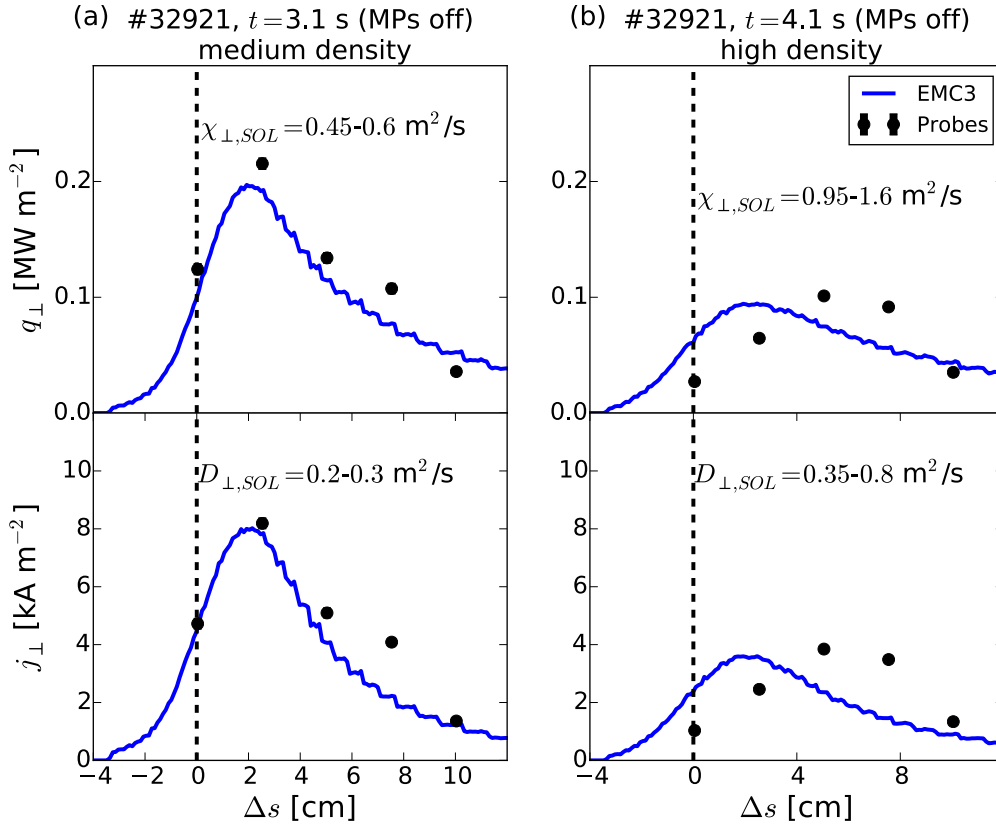**Figure 6.5:** EMC3-EIRENE heat (top) and particle flux (bottom) simulation results #32921, 3.1 s (a) and #32921, 4.1 s (b).

heat $\chi_{i,\perp}$ and $\chi_{e,\perp}$ were adapted individually for each simulated time point. For the medium density case heat and particle flux profiles are in good agreement with the measured data. For the high density case, the heat as well as the particle flux distributions are centered closer to the separatrix than the measurement results. This might be a consequence of the lack of volume recombination in the code, leading to an overestimation of the particle flux near the strike line and consequently also of the heat flux. However, the magnitude of the heat as well as the particle flux are approximately in agreement with $q_{LP,\perp}$ and $j_{sat}$, respectively.

In the MP-on simulations all resonant surfaces within $\psi_N < 0.97$ were screened. Figures 6.6b and c show the simulated heat flux profiles at the toroidal angles $\phi = 40°$ (solid, blue) and $\phi = 130°$ (dashed, blue) of the medium and high density cases with MPs. The black symbols show again the heat flux measured by the Langmuir probes. The error bars of the probe measurements indicate the amplitude of the toroidal heat flux variation, which is defined as

$$\Delta q_\perp \equiv \sqrt{2}\sigma_q. \tag{6.3}$$

Here $\sigma_q$ is the standard deviation of $q_\perp$ over one MP rotation period. The raw
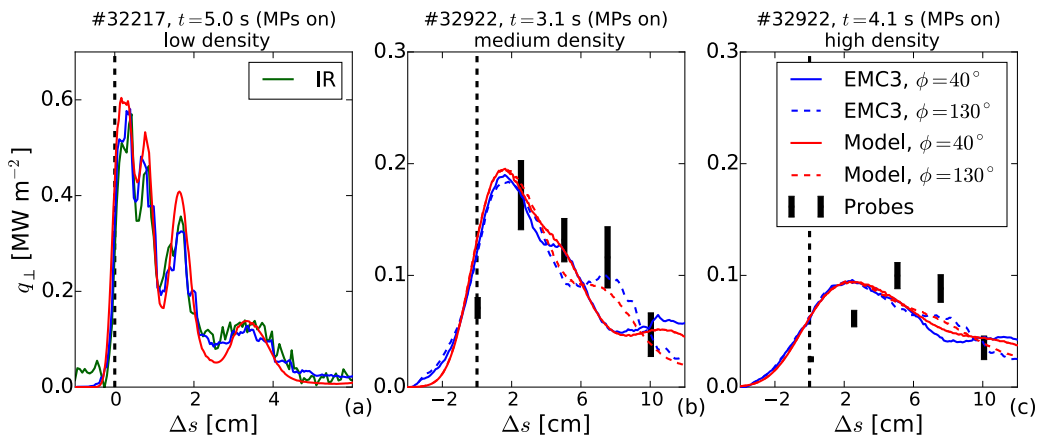
**Figure 6.6:** Comparison of the experimental heat flux profiles of #32217, 2.4 s (a), #32922, 3.1 s (b) and #32922, 4.1 s (c) with EMC3-EIRENE results (blue) and ad-hoc model (red) results at $\phi = 40°$ (solid) and $\phi = 130°$ (dashed). The green curve in (a) shows thermography measurements, and the black symbols in (b) and (c) Langmuir probe measurements. The error bars of the Langmuir probe measurements indicate the heat flux oscillation amplitude.

data and the data obtained by the signal processing procedure to obtain $\sigma_q$ is shown in Fig. 6.7 for the heat flux obtained by one of the outer target triple Langmuir probe in the H-mode deuterium discharge #33226, which will be discussed in more detail in section 6.2. A median filter was applied here to the data to remove outliers, e.g. due to small ELMs. The unfiltered data is shown in green and the median filtered one in blue. In red the average value $\langle q_{\perp,LP} \rangle$ and the amplitude $\Delta q_{\perp,LP}$ over one MP period around 3.75 s are shown. For the L-mode case discussed in this section an arithmetic mean filter was applied instead of a median filter.



**Figure 6.7:** Signal processing of the $q_\perp$ data measured by a Langmuir probe.

To compare the medium and high density cases to the heat flux of a low density discharge with MP field, also the simulated heat flux profile at $\phi = 40°$ of the

discharge #32217, which was discussed in chapter 5, is shown in Fig. 6.6a.
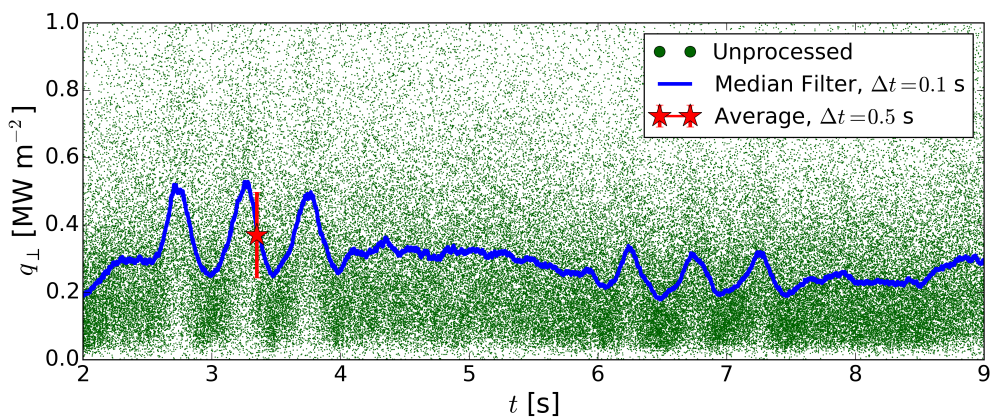Here the green curve shows the heat flux measured by the IR system.

It can be seen in Fig. 6.6a–c that the toroidal heat flux variations show the
same tendency in the simulations as observed in the experiment: the lobes in
the heat flux distribution smooth out and it becomes increasingly axisymmetric
from the low density to the high density case.

### 6.1.4    Comparison of Simulated Heat Flux to Semi-Analytical Model

It is illustrative to compare the simulated MP-on target heat flux results to
a semi-analytical model, which is similar to the ones presented in [121] and
[122] and, as will be shown, describes the EMC3-EIRENE results in good
approximation. In this model the target heat flux is completely determined
by the competition between parallel and perpendicular transport, and the
field geometry. As in the MP-off case, the competition between parallel and
perpendicular transport is parametrized by a power decay length $\lambda_q^{on}$ and a
power spreading factor $S^{on}$ (cf. sections 3.5.2 and 3.5.3), which are expected
to be of similar magnitude (but not necessarily equal) as the respective MP-off
values $\lambda_q^{off}$ and $S^{off}$. However, in contrast to the MP-off case, a *corrugated*
separatrix is assumed, which is sketched in Fig. 6.8. Accordingly, upstream
(u) at the midplane the parallel power flux can be expressed as

$$q_\| = q_0 e^{\frac{-\Delta r_u^{corr}}{\lambda_q^{on}}},$$
(6.4)

where $\Delta r_u^{corr}$ is the distance from the corrugated separatrix at the outer mid-
plane. The path of the corrugated separatrix has to be prescribed in the model,
and in this work the surface between the $N_{\theta,inner} = 0$ and $N_{\theta,inner} > 1$ basins,
where $N_{\theta,inner}$ is the number of integer poloidal turns towards the inner target,
was chosen[i] (cf. Fig. 4.9). The physical reasoning behind this choice is that the
region with $N_\theta = 0$, has similar connection lengths as the SOL in the MP-off
case and is therefore also assumed to play a similar role. The field lines are
mapped to the divertor target and the diffusion in the divertor region is taken
into account by a convolution with a Gaussian, according to (3.25), with the
divertor spreading factor $S^{on}$.

The 1D profiles obtained by the model are shown in Fig. 6.6a-c by the red
curves. For the profiles shown in Fig. 6.6b and Fig. 6.6c a satisfactory agree-
ment between the model and the EMC3-EIRENE simulations was found by
choosing $\lambda_q^{on} = \lambda_q^{off}$ and $S^{on} = S^{off}$. Here $\lambda_q^{off}$ and $S^{off}$ were obtained by fitting
(3.25) to the MP-off solution. For the low density profile shown in Fig. 6.6a, a
higher divertor spreading factor than in the MP-off case, with $S^{on} = 1.4S^{off}$,

---

[i]This is the main difference to the model in [121], where the corrugated separatrix was
determined by the condition that the connection length is between 120 and 125 m on it
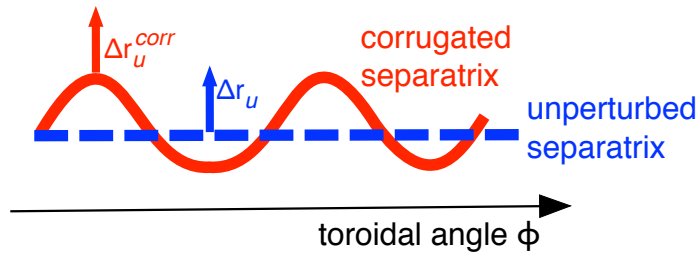
**Figure 6.8:** Sketch of unperturbed (blue) and corrugated (red) separatrices at the midplane in dependence of the toroidal angle $\phi$.

had to be chosen to obtain agreement between the EMC3-EIRENE simulation and the model.

In Fig. 6.9 (top) the EMC3-EIRENE simulation results of the outer divertor target heat flux patterns for the low density (left) and the high density cases (right) of Fig. 6.6, and the corresponding heat flux pattern obtained by the model (bottom) are shown. To highlight the effect of the divertor spreading factor $S^{on}$, in Fig. 6.9 (middle) the corresponding patterns with the assumption of no divertor spreading (i.e. $S^{on} = 0$) are shown. Here for both cases a strong non-axisymmetry with distinct lobe structures can be observed, since for this case $S^{on}$ is considerably smaller than the power decay length.

For the high density case $S^{on}$ comes out 15 times larger than for the low density case, and therefore the the smearing out of the lobes is considerably stronger for the higher density. For attached L-mode plasmas this smearing out effect of the lobes with increasing $S^{on}$ has already been shown experimentally in ASDEX Upgrade [103, 121], where $S^{on}$ was varied by increasing the density under attached conditions. Furthermore, in [121] the experimental results could be reproduced with a similar model to the one used here.

The reproducibility of the heat flux profiles with this simple model, which only takes into account diffusive transport processes, parametrized by $S^{on}$ and $\lambda_q^{on}$, shows that these processes alone are able to explain the diminishing of localized heat flux patterns.

## 6.2 ELM-Mitigated H-Mode Detachment Experiments with Magnetic Perturbation Fields

In section 6.1.2 it was shown that for typical L-mode conditions no burn through occurs. However, as discussed in chapter 4, MPs are considered as an option to mitigate or suppress ELMs in H-mode discharges in future fusion devices, such as ITER. For these conditions the transport properties differ from L-mode and the results presented in section 6.1.2 are not automatically transferable. To measure the fluxes with MPs under these conditions a comprehensive set of H-mode deuterium discharges, with partially ELM-mitigated
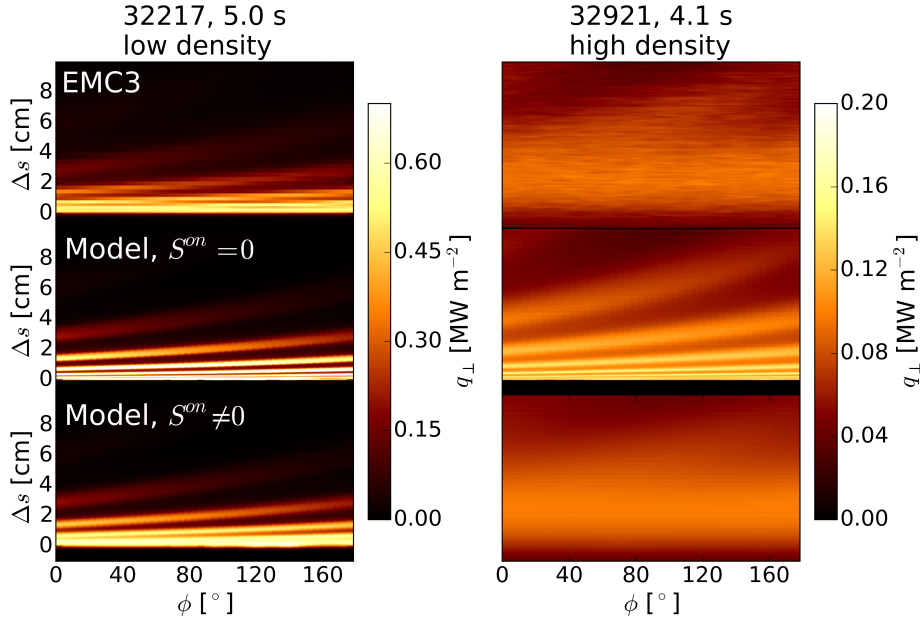
**Figure 6.9:** 2D target heat flux patterns for #32217 at 5.0 s (left) and #32922 at 4.1 s (right) obtained by EMC3-EIRENE simulations (top), and from the ad-hoc model with the assumption of no divertor spreading (middle), and with divertor spreading (bottom).

conditions, were carried out in AUG. The discharges were, however, carried out at a higher collisionality than the one envisaged for ITER, since in current tokamaks low collisionality is incompatible with the high edge densities required to reach detachment.

In contrast to L-mode plasmas, in H-mode plasmas it is impractical to reach detachment by increasing the density, since by this alone the plasma temperature in the divertor cannot be decreased to sufficiently low values. Instead, nitrogen was puffed under stationary conditions in order to increase the radiation in the divertor region (cf. Sec. 3.3.3). The typical setup for the discharges can be seen in Fig. 6.10, where time-traces for the discharge #33226 are shown. The shaded regions indicate the time periods where the MP field with toroidal mode number $n = 2$ and differential phase difference $\Delta\varphi = 180°$ were switched on. Compared to the L-mode density ramp discharge, a low MP rigid rotation frequency of 2 Hz could be used, since the H-mode discharges are stationary over several seconds. The lower rotation frequency has the advantage that the screening of the MP field by the PSL is smaller. Figure 6.10a shows the heating power, Fig. 6.10b the MP coil currents, Fig. 6.10c the core and edge line integrated densities $n_{core}$ and $n_{edge}$, Fig. 6.10d the nitrogen and deuterium gas puff levels $\Phi_{N2}$ and $\Phi_{D2}$ and Fig. 6.10e the outer divertor shunt current signal $I_{polsola}$, which serves as an ELM indicator. The toroidal magnetic field was $B_t = -2.5$ T and the plasma current $I_p = 0.6$ MA. The relatively low $I_p$ results in a high $q_{95} \approx 6.5$ and according to the scaling (3.23) a relatively large power fall off length $\lambda_q$ of about 3.5 mm.
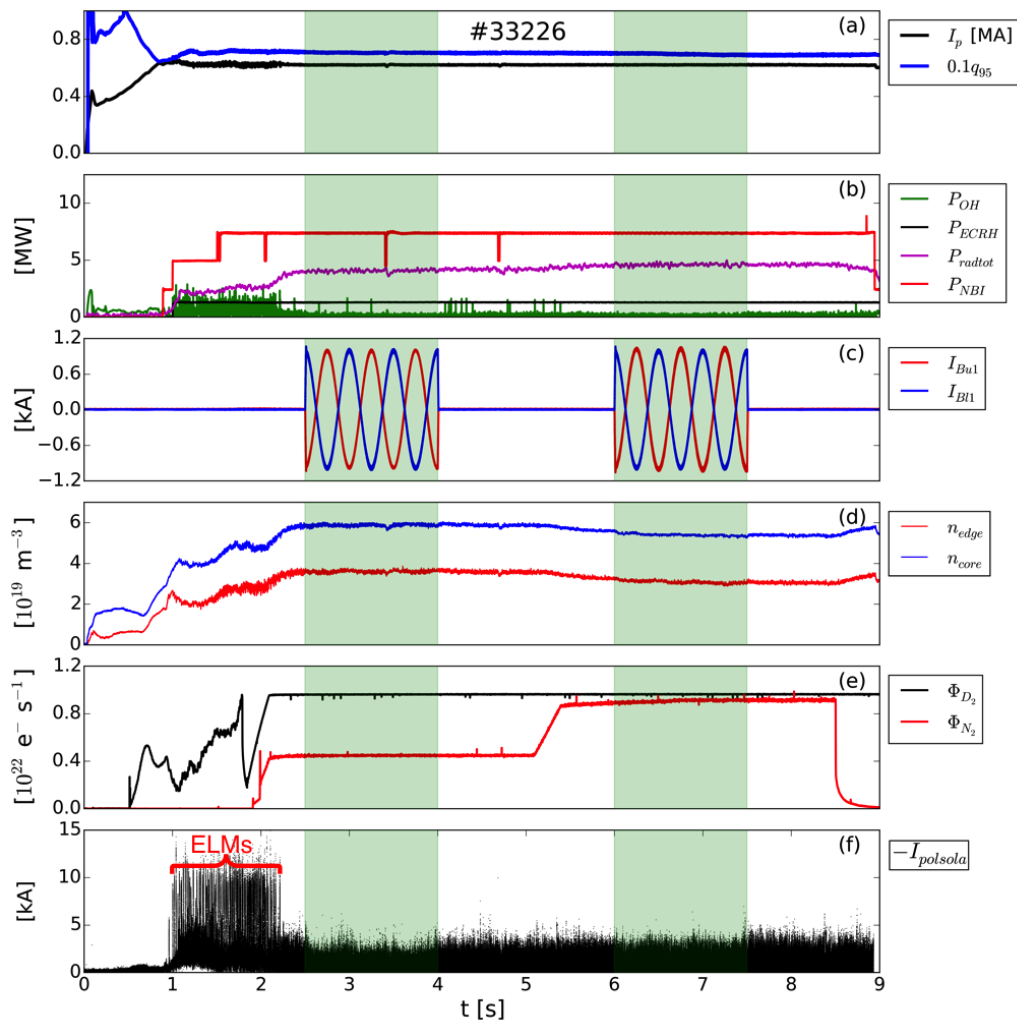
**Figure 6.10:** Time traces of plasma current $I_p$ and safety factor $q_{95}$ (a), heating and total radiation (b), coil currents $I_{Bu1}$ and $I_{Bl1}$ (c), line integrated edge and core densities $n_{edge}$ and $n_{core}$ (d), deuterium and nitrogen puff rates $\Phi_{D2}$ and $\Phi_{N2}$ (e), and divertor shunt current $I_{polsola}$ (f) for the H-mode discharge #33226.

The NBI heating power was constant, with $P_{NBI} = 7.5$ MW. In addition constant central ECRH of $P_{ECRH} = 1.25$ MW was applied during the discharge. At 5.0 s the nitrogen puff level was raised to increase the divertor radiation and decrease the target heat flux. During the stationary phases of the discharge the MP field was rotated several times to measure the 2D divertor fluxes with the triple Langmuir probes. As can be seen in the $I_{polsola}$ signal, type I ELMs were suppressed for $t \geq 2.2$ s and only small ELM-like events were observed. Note that, although ELM mitigation with MPs has been achieved before in AUG [123], in the shown discharge the type I ELMs are already suppressed before the MPs are switched on. The ELM mitigation might in this case be a result of the nitrogen seeding [124] or the high density [125]. Also in the other H-mode discharges with nitrogen seeding carried out for this study the ELMs

**Figure 6.11:** Time traces of the heat flux profile (a) measured by Langmuir probes for time-slices from discharges #33226, #33227 and #33228 with $\Delta\varphi = 180°$ and corresponding MP coil current $I_{Bu1}$ (b), nitrogen and deuterium seeding rates $\Phi_{N2}$ and $\Phi_{D2}$ (c) and $T_{div}$ signal (d).

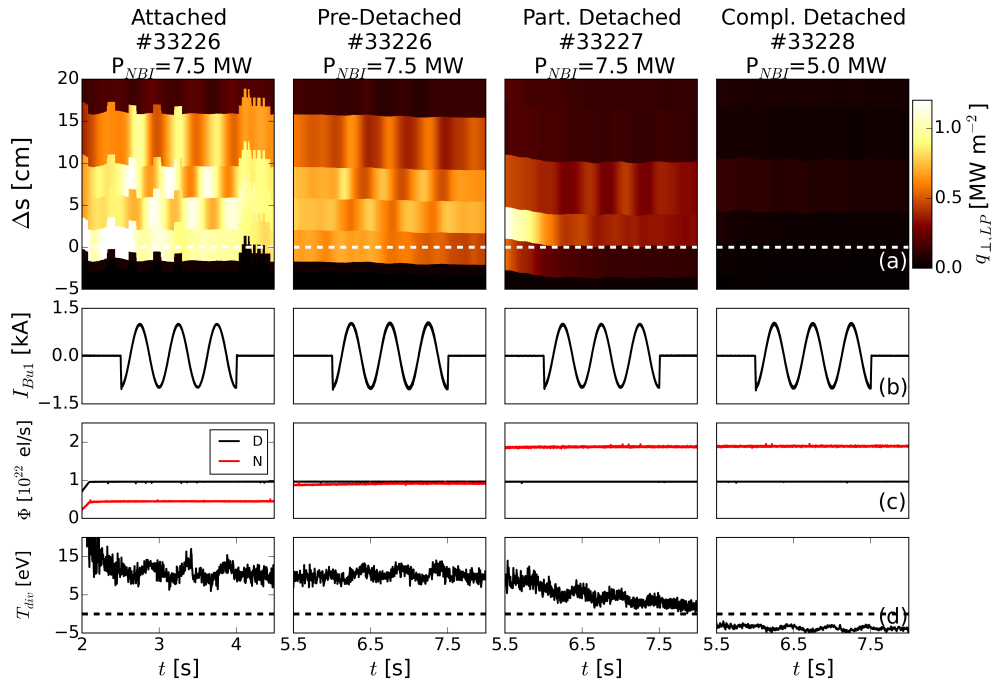were already mitigated before the MP phase. Based on the $I_{polsola}$ signal, no clear effect of the MP field on the already mitigated ELM characteristics was observed.

The other discharges carried out for this study differed in the neutral beam heating power and/or the nitrogen seeding level $\Phi_{N2}$. By this a scan of all relevant detachment states was achieved. Figure 6.11a shows the heat flux obtained by the Langmuir probes for increasingly detached states from left to right. In contrast to the L-mode discharges discussed above, the temperature measurement obtained by the Langmuir probes was reliable here, and therefore no assumptions on the temperature had to be made. The time slices were taken from ELM-mitigated phases of the discharges #33226 and #33227 with $P_{NBI} \approx 7.5$ MW and #33228 with $P_{NBI} \approx 5.0$ MW. Figure 6.11b shows the MP coil current signal $B_{u1}$, Fig. 6.11c the respective nitrogen and deuterium seeding levels $\Phi_{N2}$ and $\Phi_{D2}$ and Fig. 6.11d the $T_{div}$ signal. For the highly attached case clear oscillations of the heat flux are observed. As the nitrogen seeding is increased the heat flux decreases, however, distinct lobe structures are still present. For the partially detached case the lobe structures become less pronounced and no clear lobe structures are visible for the strongly detached case, where the power flux to the target is strongly reduced.

The toroidally averaged values and oscillation amplitudes of each of the 2D

profiles shown in Fig. 6.11a can be represented as 1D profiles, as already done for the L-mode discharge #32922. The resulting profiles for the different detachment states are shown in Fig. 6.12 by the red data points. As before the position of the symbol represents the mean value, and the error bar the oscillation amplitude. For comparison the corresponding MP-off profiles are shown in blue. As already observed in the 2D representation in Fig. 6.11a, the oscillations, represented by the length of the error bars, become gradually smaller as the divertor detaches. For the attached case, shown in Fig. 6.12a, the heat flux variation is around 35 %. In the pre-detached (b) and the partially detached (c) cases the maximum observed relative oscillation amplitudes are 25 % and for completely detached conditions (d) the relative amplitude drops to 15 %. As in the L-mode discharge, no burn through was observed for this scenario, i.e. no toroidally localized high heat flux zones were measured and the outer divertor detaches uniformly.
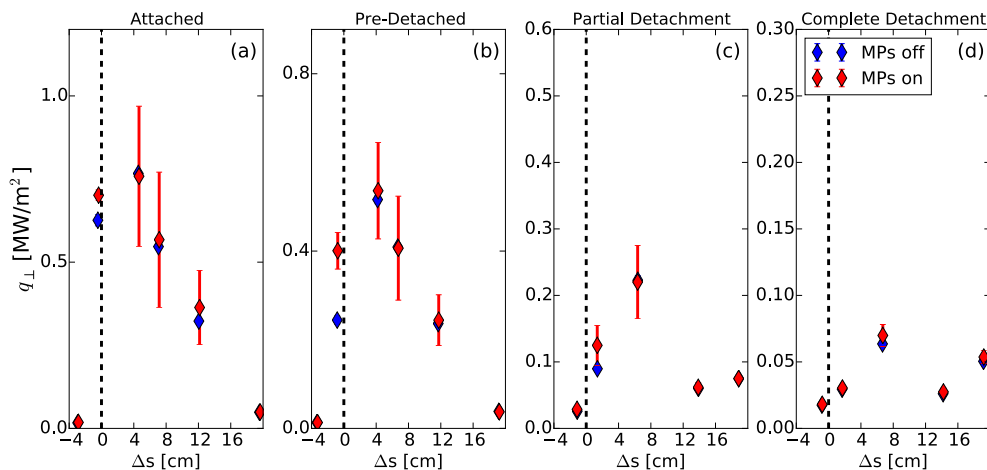


**Figure 6.12:** Outer target heat flux profiles for the H-mode discharges #33226, #33227 and #33228 with $\Delta\varphi=180°$. The blue symbols correspond to the MP-off values and the red ones to the MP-on values. The error bars show in both cases the measured amplitude of the heat flux variations.

From the probe measurements it was found that in all cases the relative temperature oscillation amplitude $\tilde{T}_e/T_e$ is of the same magnitude as the relative particle flux oscillation amplitude $\tilde{\Gamma}/\Gamma$. By assuming that $\gamma T_e \gg E_{rec}$ in (2.21), which is valid if $T_e$ is above several eV, the relative heat flux oscillation amplitude can be expressed as

$$\delta_q \approx \frac{\tilde{T}_e}{T_e} + \frac{\tilde{\Gamma}}{\Gamma}. \tag{6.5}$$

Since $\tilde{T}_e/T_e \approx \tilde{\Gamma}/\Gamma$, temperature and particle flux oscillations contribute by the same amount to the heat flux oscillations.

# 6.3 Effect of MPs on Radiation in the Confinement Region

In section 3.3.3 it was discussed that in order to reduce the target heat loads and reach detachment in a tungsten device it is commonly necessary to seed impurities such as nitrogen into the plasma. In current fusion experiments and ITER most of the impurity radiation should be produced in the divertor region, in order not to degrade the core confinement[ii]. Hence it is desirable that the impurities are retained in the SOL and the private flux region, and do not accumulate in the core region. The transport induced by the MPs leads to a modifications of the plasma fields, with lobes of higher temperature extending in the SOL. This lobes might lead to an increase of the volume where nitrogen can increase efficiently and, hence, to an increase of the maximum attainable radiation in the SOL [3].

In AUG experiments a small effect of the MP field on the core radiation could be observed in nitrogen seeded H-mode discharges. This effect was, however, only observed if the divertor was close to a completely detached state, with $T_{div}$ around zero. As an example, in Fig. 6.13a time traces of the total radiation $P_{radtot}$ and the core radiation $P_{rad}$, in Fig. 6.13b the $T_{div}$ signal, and in Fig. 6.13c the upper and lower coil currents $I_{Bu1}$ and $I_{Bl1}$ in sector one for the discharge #33664 are shown. This discharge had a total input power of about 8.5 MW, and deuterium and nitrogen puff rates of $\Phi_{D2} = 1 \times 10^{22}$ $e$/s and $\Phi_{N2} = 2 \times 10^{22}$ $e$/s. At 4.2 s the MP field in an $n = 2$, $\Delta\varphi = 90°$ configuration with a rigid roation frequency of 2 Hz was switched on. At about 4.6 s the core radiation $P_{rad}$ increases by about 10 %. This increase is accompanied by a drop of the $T_{div}$ signal. After the MPs are switched off at 6.7 s $P_{rad}$ decreases again, however $P_{radtot}$ and $T_{div}$ stay at a constant level. In Fig. 6.14 reconstructions of the radiation distribution obtained from the foil bolometers at 4.1 s (a), where the MPs are off, and 4.6 s (b), where the MPs are on, are plotted. The foil bolometry data was here averaged over one MP period, i.e. 0.5 s. It can be seen that the increase of core radiation is accompanied by a decrease of the radiation in the outer diverter region, while it increases inside the separatrix near the X-point.

In the following it will be discussed how the results observed in the experiment compare qualitatively to EMC3-EIRENE simulations. In the simulations with MP field different screening scenarios were again assumed, which will be called 'vacuum' case, 'weakly screened' case, and 'strongly screened' case. The field and input parameter of parameter set 2 from table 5.1 were used. The transport model for the nitrogen impurities was described in chapter 5.1, with the nitrogen particle diffusion coefficient being the same as the one for the deuterium ions. The total radiated power $P_{rad}$ was set as an input parameter to 25 % of the input power $P_{net}$. The nitrogen source is described here by the

---

[ii]In DEMO a large fraction will have to be radiated inside the separatrix, in order to reduce the target heat flux to sufficiently low values [126]
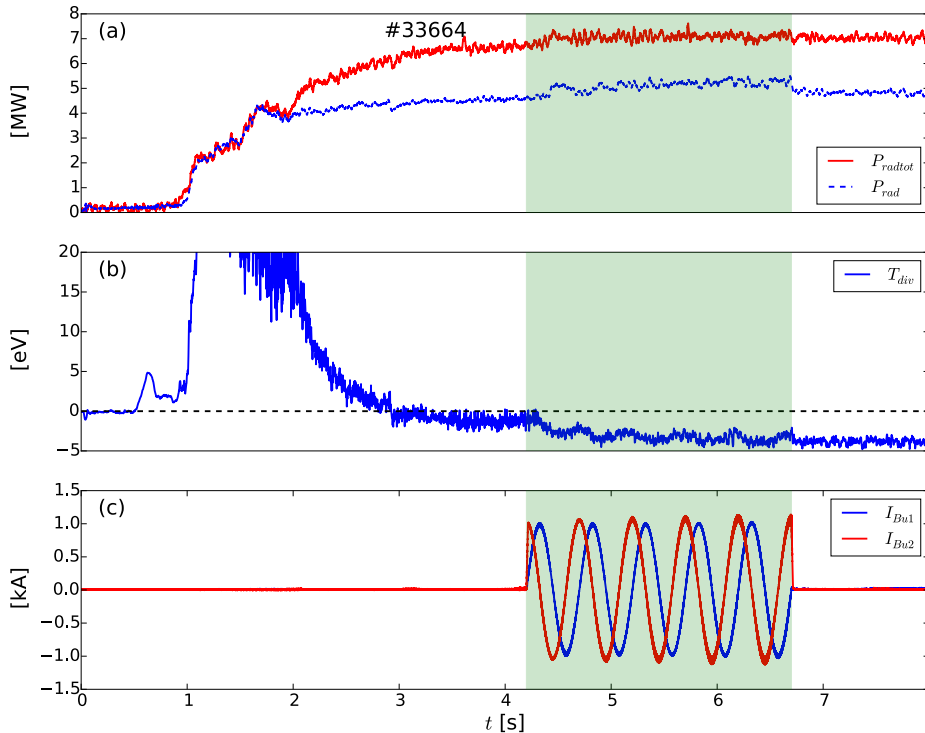
**Figure 6.13:** Time traces for total radiation $P_{radtot}$ and the core radiation $P_{rad}$ (a), the $T_{div}$ signal (b), and the upper and lower coil currents $I_{Bu1}$ and $I_{Bl1}$ (c) for discharge #33664.

assumption of chemical sputtering [42], i.e. for each deuterium ion hitting the target $Y$ nitrogen atoms are injected into the plasma. The sputtering yield $Y$ was iteratively adapted by the code, in order to reach the aforementioned radiation level. This model is reasonable if the wall is saturated with nitrogen, which is sputtered from the wall by the impinging plasma ions.

In Fig. 6.15 simulation results at $\phi = 11.25°$ for the MP-off case (a), the vacuum case (b), the case with weak MP field screening (c), and the case with strong MP field screening (d) are shown. The blue curves in (c) and (d) represent the outermost screened rational flux surface. The top row in Fig. 6.15 shows the Mach number $M$, the middle row the nitrogen density $n_N$, and the bottom row the nitrogen radiation $P_{rad,N}$. Here the Mach number is defined as $M = v/c_s$, where $v$ is the parallel plasma fluid velocity and $c_s$ the ion sound speed. Negative/positive Mach numbers correspond to flows towards the outer/inner target. Note that for $n_N$ and $P_{rad,N}$ a logarithmic color scale was used.

For the vacuum case the nitrogen density as well as the radiation inside $\psi_N = 1$ is considerably decreased with respect to the MP-off case. Moreover, the nitrogen distribution is not homogeneous, but shows some fine structure pattern. For the screened cases the nitrogen density increases with respect to the vacuum case, and it is moreover approximately homogeneous inside the last screened surface.
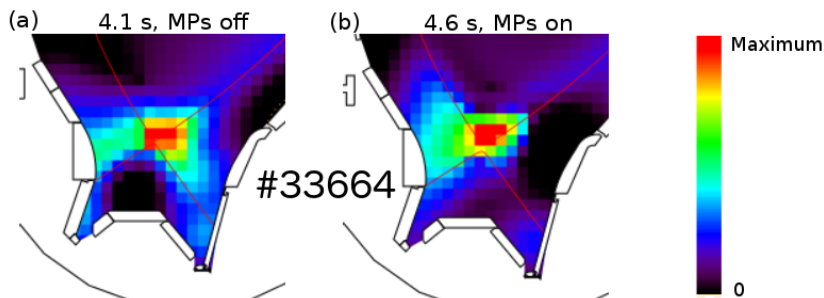
90

**Figure 6.14:** Radiation distribution reconstruction from foil bolometer measurements for the MP-off time point 4.1 s (a) and the MP-on time point 4.6 s (b) of discharge #33664.

The lower nitrogen density in the MP-on case can be related to flows which are generated inside the $\psi_N = 1$ surface. The Mach numbers in Figs. 6.15b–d show a 2D checkerboard like pattern of alternating co- and counter clockwise ion flows, which was described in detail in [95]. For the vacuum case the checkerboard pattern can be particularly well seen near the X-point. From the impurity model equation B.8 it can be seen that ion particle flows exert a friction force on impurities, and therefore impurities crossing the $\psi_N = 1$ boundary can be 'flushed out'. For the weakly and strongly screened cases the pattern is approximately limited to the region outside the last screened flux surface.

The nitrogen density $\langle n_{N,core} \rangle$ averaged over the region $\psi_N < 1$, and the ratio $P_{N,core}/P_{N,tot}$ for the four simulated cases are shown in Fig. 6.16. Here $P_{N,core}$ is the nitrogen radiation inside $\psi_N = 1$, and $P_{N,tot}$ the total nitrogen radiation. Generally, it can be noted that the nitrogen density inside $\psi_N = 1$ is about proportional to the radiated power in this region. For the MP-off case and the strongly screened case, $\langle n_{N,core} \rangle$ is approximately the same, and correspondingly in both cases about 20 % are radiated inside $\psi_N = 1$. For the weakly screened and the vacuum case the fraction radiated inside $\psi_N = 1$ decreases to about 6 % and 2.5 %, respectively.

It can be concluded that in the simulations the parallel flows generated along open field lines inside $\psi_N = 1$ by MPs can reduce the nitrogen density and radiation. These simulation results are, however, qualitatively not in agreement with the experiment, where the core radiation increased. Introducing strong screening in the simulations pushes open field lines further outwards, and thus increases the nitrogen density and radiation inside $\psi_N = 1$ to similar values as in the MP-off case. For low perpendicular transport coefficients, the radiation inside $\psi_N = 1$ even increased by about 10 % with screening, as was also observed experimentally. However, since it is currently not possible to simulate detached states with EMC3-EIRENE, the simulation results represent an attached regime, while experimentally the increase of $P_{rad}$ was only observed in already detached regimes. The agreement with the experiment might therefore be fortuitous, and more refined simulations, with additional physical processes
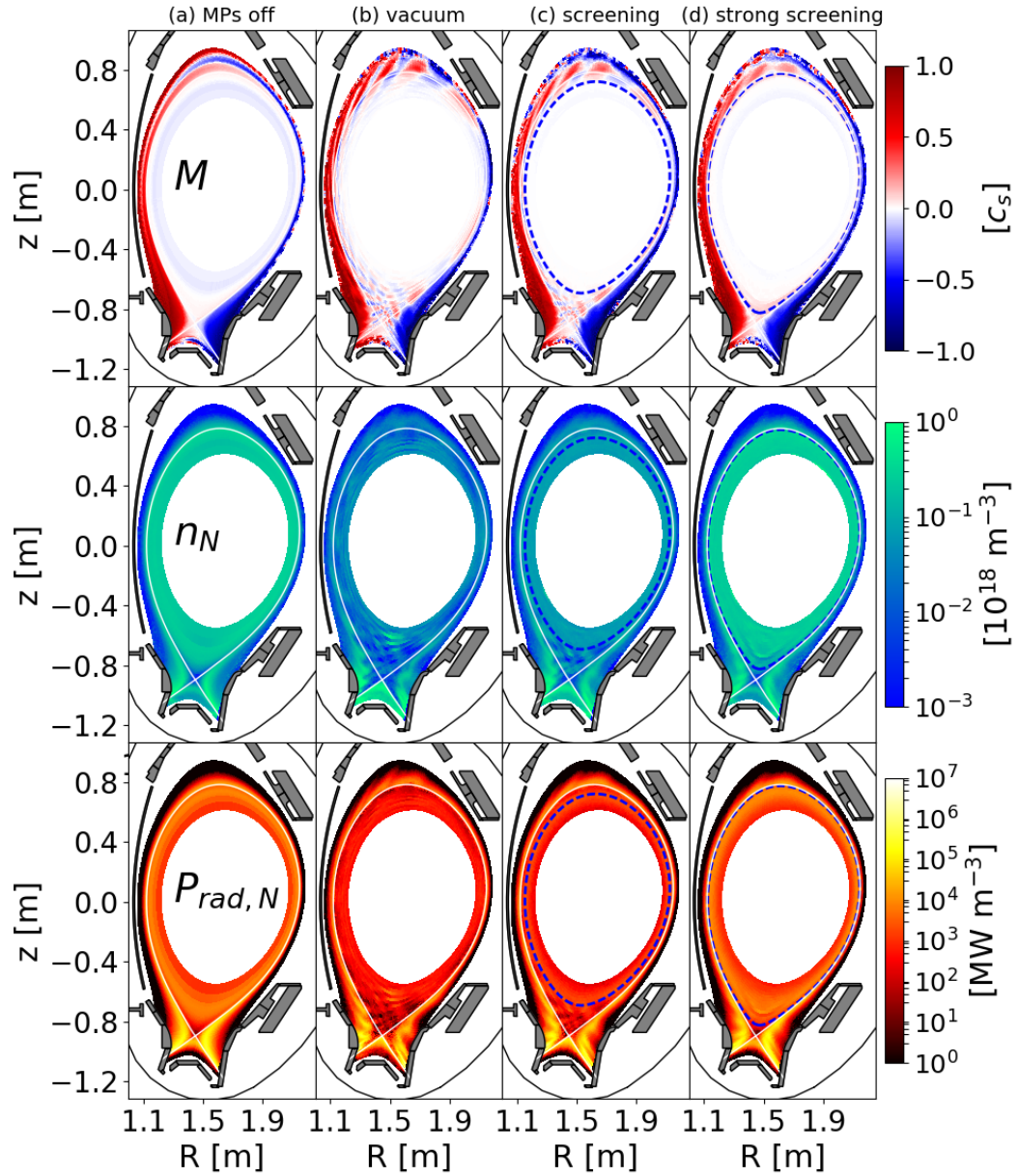
**Figure 6.15:** Mach number $M$ (top), nitrogen density $n_N$ (middle) and nitrogen radiation $P_{rad,N}$ (bottom) for the MP-off case (a), the vacuum case (b), the weakly screened case (b) and the strongly screened cased (d).
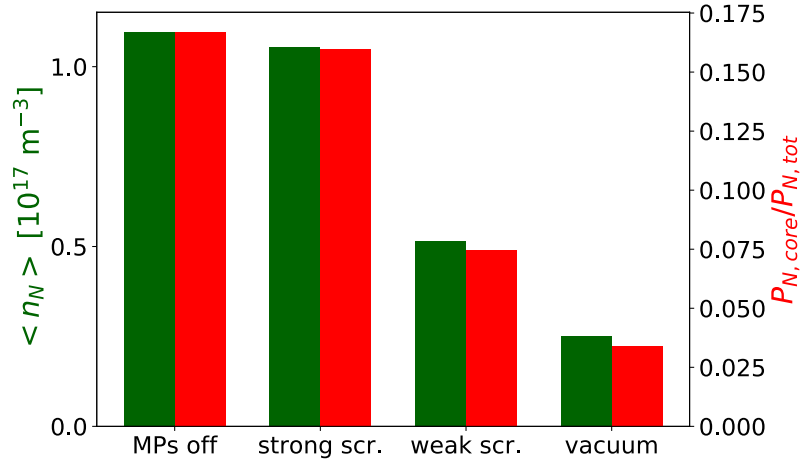
**Figure 6.16:** Averaged confinement nitrogen density (green, left axis) and fraction of radiated power in the confinement (red, right axis).

such as drifts and recombination, may have to be carried out to confirm the result.

## 6.4 Conclusions

A comprehensive set of deuterium L- and ELM-mitigated H-mode discharges with and without MP fields was carried out at AUG to study the 3D features in the divertor as they are introduced by MP fields at high densities up to the detached regime. By rotating the MP field, the full 2D heat and particle fluxes could be measured with triple Langmuir probes. In the attached case toroidal heat flux variations of up to 50 % were observed. For partially detached and strongly detached conditions these variations decrease to below 20 % and in particular no burn through due to localized strong power fluxes was observed. For the L-mode density ramp discharges two time points were compared to simulations with EMC3-EIRENE. Although, the simulations are not fully valid in the detached regions, where atomic processes not taken into account in EMC3-EIRENE play a role, the decrease of the toroidal heat flux variations could be reproduced. Moreover, from the EMC3-EIRENE heat fluxes without MP field the corresponding simulated heat fluxes with MP field could be obtained in good approximation by using a semi-analytical model. In the EMC3-EIRENE simulations as well as the model the decrease of the toroidal heat flux variations can be attributed to a decreasing ratio of parallel to perpendicular heat diffusion. This means that the relative effect of the perpendicular diffusion becomes larger and the heat flux variations smear out.

In ITER the possibility of a burn-through might necessitate to rotate the MP field, which would entail large engineering efforts. However, from the results presented in this chapter it can be concluded that in ITER – assuming the perpendicular heat diffusion in the divertor is of similar magnitude as in AUG

– a burn through is an unlikely scenario and rotating the MP field would therefore not have any beneficial effect with regard to power exhaust.

Furthermore, in H-mode experiments with MPs a small increase by about 10 % inside the unperturbed separatrix located at $\psi_N = 1$ was observed for almost completely detached divertor conditions. In contrast, in EMC3-EIRENE simulations with unscreened MP field, the core nitrogen density and radiation was considerably decreased, since nitrogen was flushed out by parallel plasma fluid flows. To increase the nitrogen radiation inside $\psi_N = 1$ to levels similar to the MP-off case, strong screening had to be introduced. The experimental observations that the MP-off and on radiation levels are similar, is therefore, in addition to the results of chapter 5, another indication for screening currents.

# Chapter 7

# Summary and Conclusions

One of the major issues for future fusion devices, such as ITER and DEMO, will be the exhaust of power and particles. Ideally, the exhaust power would be distributed uniformly on the fusion device's vessel wall, in order to guarantee low peak heat loads. However, since the parallel transport is orders of magnitudes larger than the perpendicular one, the power impinges within a narrow layer of width $\lambda_q$ on the divertor targets. According to experimentally derived scalings, $\lambda_q$ is only in the order of millimiters at the outer midplane of the plasma torus. If the heat flux is not mitigated, the maximum tolerable target heat flux of 5–10 MW/m$^2$ in a steady state operation will be exceeded, leading to damages of the target.

For this reason, it will be mandatory to operate future fusion devices in a socalled *detached* regime. In this regime, power as well as plasma particle fluxes are dissipated before reaching the targets. Detached regimes will likely only be achievable if impurities, such as nitrogen, neon or argon, are injected into the plasma. These lead to increased radiation in the plasma edge region and by this to low plasma temperatures at the target. Only at these low temperatures the atomic and molecular processes required to reach detachment set in.

The achievement and control of detached regimes has led to intense research activities, including a large number of experimental and numerical studies. Since tokamaks are intrinsically axisymmetric, these studies have been largely concentrated on effectively 2D configurations. However, in recent years 3D magnetic perturbation fields with a strength of about a factor of thousand smaller than that of the equilibrium field have been actively applied in AUG and other tokamaks in order to control plasma instabilities (ELMs) in the edge region. Due to the 3D nature of the MP fields, they also lead to a non-axisymmetric target heat and particle flux distribution on the targets.

This new situation might have beneficial and harmful effects on the power exhaust, which were addressed in this work. On the one hand, the MP field might lead to an effectively increased radial transport, due to the radial magnetic field component introduced by it. This in turn would lead to decreased peak heat and particle fluxes. Furthermore, by this increase of radial trans-

port the volume in the *Scrape Off Layer (SOL)* where impurities can radiate might be increased. On the other hand, the non-axisymmetry of the MP field leads to localized heat fluxes under attached conditions. At the locations of increased heat flux, detachment might be more difficult to achieve than in the 2D case.

In this work the effects of the MP field on power and particle exhaust have been investigated experimentally and numerically. The simulations were carried out with the 3D plasma and neutral particle transport code EMC3-EIRENE. Modeling of discharges with MPs had to take into account the magnetic field created by the plasma in response to the external MP field. Knowing this plasma response field, is not only important to model plasmas of todays experimental divertor tokamaks, but is also crucial in order to conduct predictive modeling for ITER. In particular, the plasma tends to screen the MP field. This effect was taken into account by implementing an ad-hoc screening model. However, since the strength of the screening is not self-consistently calculated in this model, the spatial extent and degree of the screening effect was determined by comparison with simple L-mode experiments at low density where the plasma remains attached to the divertor and thus the non-axisymmetric structure of power loads can be diagnosed with high spatial resolution IR cameras.

Simulations with unscreened MP fields show a decreased edge confinement and an increased toroidally averaged power fall off length $\lambda_q$ at the target with respect to the MP-off case, which was not observed in experiments, where similar values of $\lambda_q$ were measured in the MP-off and on cases. This finding could only be reproduced in the simulations if strong screening was assumed. A further experiment, in which heat pulses were deposited in the plasma edge corroborated the finding that strong screening is needed to reproduce the data. In order to simulate the heat pulse transport of this experiment, EMC3-EIRENE was modified in the course of this work. The simulations with this modified version show that without screening the heat pulse propagates considerably faster to the target than in the MP-off case. Again, experimentally this was not observed.

A further important result found in this work was that in simulations MPs can indeed increase $\lambda_q$. Although, due to screening $\lambda_q$ is not increased by MP fields for the situation of AUG, a pronounced increase can be expected for small values of $\lambda_q$ and high MP field strengths.

Using a heuristic argumentation, it was possible to fit the toroidally averaged $\lambda_q$ by an analytical function, which depends on the magnetic footprint size on the target, and the corresponding $\lambda_q$ for the MP-off case. Applying this fit to ITER parameters, shows that, in contrast to AUG, a significant increase of $\lambda_q$ may be possible, in agreement to what was found in Ref. [113]. For a $\lambda_q$ of 1 mm even an increase by about 300 % is predicted by the fit.

Although the experimentally observed toroidally averaged heat flux is approximately the same with and without MP fields in AUG, the heat flux profiles still show localized heat flux patterns for attached conditions. For ITER this

may require to rotate the MP field, which would be challenging from a technical point of view. To address the issue of a possible *burn-through* in localized regions of strong power fluxes a number of L- and H-mode experiments were carried out in AUG. It was found that, as the divertor detaches, the heat flux distribution becomes increasingly axisymmetric, i.e. no strongly toroidally localized heat flux pattern was measured. This observation can be explained by the decreasing parallel heat transport for decreasing temperatures, such that the relative importance of the perpendicular transport increases.

Due to the scientific efforts made regarding power exhaust with MP fields in tokamaks, it is now a largely understood field. The results presented in this thesis show that in AUG no clear advantage of MP fields on power exhaust handling can be observed under normal operating conditions. However, in ITER the effect of the MP field on the magnetic field topology in the edge is predicted to be larger than in current devices and, therefore, a beneficial effect may be possible. On the other hand, it was shown that MP fields do not introduce unfavorable target heat flux distributions under conditions in which ITER will be operated. Hence, MP fields do not endanger a safe operation.

**Outlook**

Experimentally MP fields were found to increase the radiation inside the unperturbed separatrix at $\psi_N = 1$ near the X-point, measured by bolometry. However, this increase was only in the order of 10 % of the total radiation, and occurred for an already almost completely detached outer divertor. EMC3-EIRENE simulations for attached cases predict that the nitrogen concentration, and hence also the nitrogen radiation, is considerably decreased inside $\psi_N = 1$ without screening, i.e. an effect contradictory to the one which is experimentally observed. Assuming strong screening, the nitrogen radiation levels inside $\psi_N = 1$ were similar as for the MP-off case. For certain transport coefficients, a small increase of the radiation inside $\psi_N = 1$ was even observed, which was of a similar magnitude as the one seen in the experiment. This agreement might, however, be fortuitous and more detailed simulations may be required to confirm this result.

# Appendices

# Appendix A

# Review of the Fitzpatrick Theory

In this appendix the plasma response is discussed in the frame of the Fitzpatrick theory [84]. We will assume in the following that the force equilibrium is given by equation (2.3), which is valid if resistivity is negligible. Taking the curl, of this equation we obtain

$$\nabla \times (\vec{j} \times \vec{B}) = \left(\vec{B} \cdot \nabla\right)\vec{j} - \left(\vec{j} \cdot \nabla\right)\vec{B} = 0 \tag{A.1}$$

Here it has been used that $\vec{\nabla} \times \vec{\nabla} p = 0$, and that $\nabla \cdot j = 0$ under stationary conditions. The magnetic field and the current are now expressed as sums of their equilibrium parts $\vec{B}_0$ and $\vec{j}_0$, and perturbation parts $\vec{b}_1$ and $\vec{j}_1$:

$$\vec{B} = \vec{B}_0 + \vec{b}_1, \quad \vec{j} = \vec{j}_0 + \vec{j}_1. \tag{A.2}$$

In the *large aspect ratio* approximation, where $a/R \ll 1$, it can be shown that the toroidal component of the magnetic perturbation field $\vec{b}_1$ and the poloidal and radial components of the perturbation current $\vec{j}_1$ are negligible, i.e. $b_{1,\phi} \approx 0$ and $j_{1,\theta} \approx j_{1,r} \approx 0$ [8]. The linearized form of (A.1) is therefore given by

$$(\vec{B}_0 \cdot \vec{\nabla})j_{1,\phi} + (\vec{b}_1 \cdot \vec{\nabla})j_{0,\phi} \approx 0, \tag{A.3}$$

We now assume that the magnetic field and current perturbations consist of a single mode

$$\vec{b}_1(r,\theta,\phi) = \vec{\widehat{b}}_1(r)e^{i(m\theta - n\phi)}, \quad \vec{j}_1(r,\theta,\phi) = \vec{\widehat{j}}_1(r)e^{i(m\theta - n\phi)}, \tag{A.4}$$

with toroidal and poloidal mode numbers $n$ and $m$. From (A.3) we obtain then for the current perturbation

$$\widehat{j}_{1,\phi} = -i\frac{nB_{0,\theta}\widehat{b}_{1,r}\frac{\mathrm{d}j_{0,\phi}}{\mathrm{d}r}}{r\left(\frac{m}{n} - q\right)}, \tag{A.5}$$

where $q = \frac{rB_{0,\phi}}{RB_{0,\theta}}$ is the safety factor. That is, in order to guarantee force balance the toroidal perturbation current $j_{1,\phi}$ has to be proportional to the

radial component of the magnetic perturbation field, and the radial gradient of the equilibrium current. However, for $q = \frac{m}{n}$, i.e. at the resonant surface of the perturbation, (A.5) has a singularity. Thus, the description by (2.3), breaks down within a layer near the rational surface, and inertial effects, resistivity, as well as viscosity have to be taken into account here.

To a first approximation this layer can be regarded as a rigid, i.e. non deformable, body with electrical resistivity $\eta$. The generalized Ohm's law valid in this layer is given by

$$\vec{E} = \eta \vec{j} \tag{A.6}$$

Applying the curl operator to (A.6), we obtain

$$\frac{\partial \vec{B}}{\partial t} = -\eta \nabla \times \vec{j}, \tag{A.7}$$

where Faraday's law of induction has been used:

$$\nabla \times \vec{E} = -\frac{\partial \vec{B}}{\partial t}. \tag{A.8}$$

If the plasma is rotating, the perturbation field in the reference frame of the plasma is given by

$$\vec{b}_1(r, \theta, \phi) = \vec{\tilde{b}_1}(r) e^{i(m\theta - n\phi - \omega t)}, \tag{A.9}$$

where $\omega$ is the plasma rotation frequency perpendicular to the equilibrium field lines at the resonant surface:

$$\omega = m\Omega_\theta + n\Omega_\phi. \tag{A.10}$$

Here $\Omega_\theta$ and $\Omega_\phi$ are the poloidal and toroidal rotation frequencies of the plasma. By inserting (A.9) into (A.7) we obtain the following relation between magnetic perturbation field and induced perturbation current

$$\nabla \times \vec{\tilde{j}_1} = \frac{i\omega \vec{\tilde{b}_1}}{\eta}. \tag{A.11}$$

The induced currents scale thus linearly with the rotation speed. In a fast rotating plasma a strong response field is created, which opposes the external magnetic perturbation field. In [84] it is shown that the width $W$ of the island which is created as a result of the perturbation field at the resonant surface, is given by

$$W = \frac{1}{(1 + (\omega\tau_{rec})^2)^{1/4}} W_{full}, \tag{A.12}$$

where $W_{full}$ is the island width which would be obtained for a non-rotating plasma with $\omega = 0$, and $\tau_{rec}$ is the reconnection time scale, i.e. the typical time scale on which the magnetic field diffuses through the resistive layer, given by

$$\tau_{rec} = \frac{\mu_0 \, r_{m,n} \Delta_{m,n}}{\eta}. \tag{A.13}$$

Here $r_{m,n}$ is the minor radius of the resonant surface and $\Delta_{m,n}$ the radial width of the resistive layer at that surface. From (A.12) we see that if $\omega \gg \tau_{rec}^{-1}$, then the island size will be much smaller than $W_{full}$.

According to the Fitzpatrick theory, the toroidal rotation frequency $\omega$ of the resistive layer results from the balance between electromagnetic and viscous torques. The electromagnetic force density is given by $\vec{f}_{EM} = \vec{j} \times \vec{B}$. On the resonant layer, this force leads to poloidal and toroidal electromagnetic torques $T_{EM,\theta}$ and $T_{EM,\phi}$, where

$$T_{EM,\theta} \approx \int_{\Delta_{m,n}} \int_S r\vec{f}_{EM} \cdot \vec{e}_\theta \mathrm{d}r\mathrm{d}S \approx \int_{\delta_{m,n}} \int_S r j_{1,\phi} b_{1,r} \mathrm{d}r\mathrm{d}S. \tag{A.14}$$

Here $S$ is the surface area of the resonant surface. In the last step it has been used that in the large aspect ratio approximation only the term which is quadratic in the perturbation quantities is nonzero. The toroidal torque can be expressed through the poloidal one by $T_{EM,\phi} = -\frac{n}{m} T_{EM,\theta}$. The dependence of $T_{EM,\phi}$ on the rotation frequency is shown in Fig. A.1a for three different MP field strengths. Here the MP field strength is parametrized by the island size $W_{vac}$ which would be created in absence of a plasma response. $W_{vac}$ has been normalized to a *reconnection island size* $W_{rec}$, whose meaning will explained below. The rotation frequency $\omega$ has been normalized to the inverse of the reconnection time scale $\tau_{rec}$. For low rotation frequencies with $\omega\tau_{rec} < 1$, $T_{EM,\phi}$ increases due to the increasing strength of the screening currents. For $\omega\tau_{rec} > 1$ the perturbation field is increasingly suppressed and $T_{EM,\phi}$ decreases again.

The electromagnetic torque is only acting on the resistive layer itself, and not on the surrounding plasma described by ideal MHD. Therefore velocity gradients and consequently viscous forces, counteracting the electromagnetic forces, are created around the resistive layer. The torque $T_{visc}$ created by the viscous force is shown in Fig. A.1a by the dashed line for a normalized initial rotation velocity $\omega_0\tau_{rec} = 7$. For $\omega = \omega_0$ the viscous force is zero, and increases linearly with decreasing layer rotation velocity.

An equilibrium rotation speed is only obtained if the viscous and electromagnetic torques cancel, i.e. if

$$T_{visc} = T_{EM,\phi}. \tag{A.15}$$

The real solutions for $\omega\tau_{rec}$ of this torque balance equation are shown in Fig. A.1b in dependence of $W_{vac}/W_{rec}$ for plasma rotation frequencies $\omega_0\tau_{rec} = 2.0, 3.0, 5.0$ and $7.0$. The arrows indicate the evolution of the rotation frequency as $W_{vac}$ increases. For $\omega_0\tau_{rec} = 2.0$ the resonant surface is gradually braked to zero rotation frequency. However for $\omega_0\tau_{rec} = 3.0, 5.0$ and $7.0$ a bifurcation occurs at a certain vacuum island width where the rational surface rotation frequency decreases abruptly. This bifurcation process is called *mode penetration*, and the smallest vacuum island size for which such a bifurcation occurs is $W_{vac} = W_{rec}$. From Fig. A.1b it can also be noted that the bifurcation towards higher rotation frequencies occurs at lower $W_{vac}$ then the one towards

low rotation frequencies, i.e. the theory predicts a hysteresis effect. Hence, once mode penetration has occurred at some vacuum perturbation magnetic field strength $B_{pen}$, the field has to be reduced to values lower than $B_{pen}$ in order to trigger a back transition.
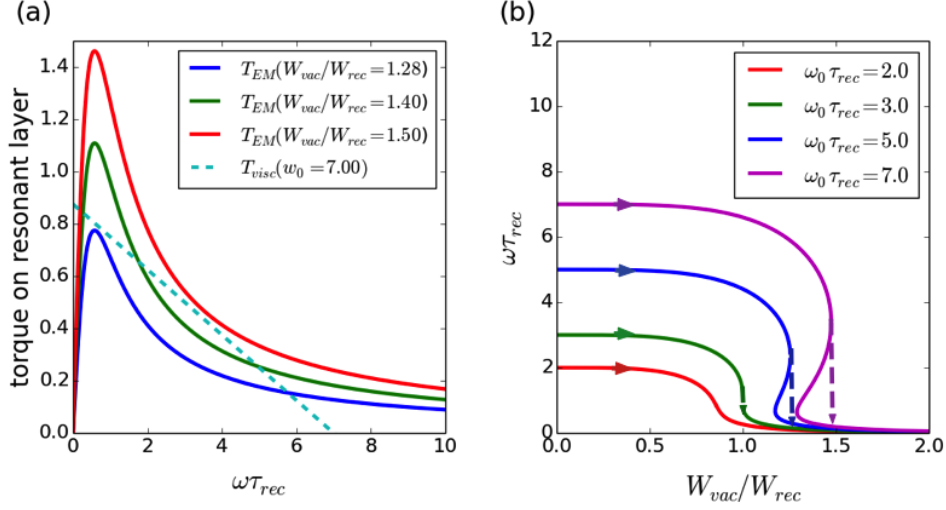


**Figure A.1:** (a) Electromagnetic and viscous forces acting on the resonant layer in dependence of the layer rotation frequency $\omega$ normalized to the inverse of the reconnection time scale $\tau_{rec}$. (b) Rotation frequency $\omega$ in dependence of the vacuum island size width $W_{vac}$ for unperturbed rotation frequencies $\omega_0 \tau_{rec} = 2.0, 3.0, 5.0$ and $7.0$.

# Appendix B

# The EMC3-EIRENE Model

In this appendix the physical model used by EMC3-EIRENE will be briefly discussed. In the current version of EMC3 the fields are assumed to be stationary (i.e. $\frac{\partial}{\partial t} = 0$). Furthermore, it is assumed that quasi-neutrality holds and that the plasma is current free:

$$n \equiv n_e = n_i \tag{B.1}$$

$$\vec{j} = 0 \Rightarrow \vec{V} \equiv \vec{V_i} = \vec{V_e} \tag{B.2}$$

Here $n_e$ and $n_i$ are the electron and ion densities, $\vec{V_e}$ and $\vec{V_i}$ are the electron and ion fluid velocities, and $\vec{j}$ is the plasma current. The electric field is assumed to be zero and the magnetic field is, as it is common in plasma transport codes, externally prescribed and not self-consistently calculated.

The plasma transport properties in a magnetic field are strongly anisotropic, with transport coefficients along the magnetic field much higher than perpendicular to it. The EMC3 equations are therefore formulated in a local coordinate system with one unit vector $\vec{b}_\parallel$ along the magnetic field and an unit vector $\vec{b}_\perp$ perpendicular to it. The derivative operators along $\vec{b}_\parallel$ and $\vec{b}_\perp$ will be denoted by $\partial_\parallel$ and $\partial_\perp$, respectively, in the following. The equations are a modified version of the *Braginskii* equations, formulated in a conservative form. In the following the individual conservation equations for particles, momentum and energy are discussed.

**Particle Conservation Equation**

The particle conservation equation is given by

$$\vec{\nabla} \cdot \left[ \underbrace{n V_\parallel \vec{b}_\parallel}_{1} - \underbrace{D_\perp \partial_\perp n \vec{b}_\perp}_{2} \right] = S_{ion}, \tag{B.3}$$

where $V_\parallel$ is plasma fluid velocity component parallel to the magnetic field. Term (1) is the parallel convective particle flux and term (2) the perpendicular diffusive particle flux, which is driven by the perpendicular density gradient.

The particle diffusion coefficient $D_\perp$ is an ad-hoc parameter in EMC3, i.e. it is prescribed. The perpendicular transport in magnetic confinement fusion plasmas is created mainly by turbulent processes. This turbulent transport is also called *anomalous*, in contrast to diffusion driven by particle collisions. Currently the anomalous diffusion coefficient $D$ is obtained by fitting simulation results to experimental data. The term $S_m$ on the right hand side of the particle conservation equation B.3, represents particle sources and sinks, e.g. due to the ionization of neutrals.

**Momentum Conservation Equation (Equation of Motion)**

The momentum conservation equation is given by

$$\vec{\nabla} \cdot \left[ \underbrace{m_i n V_\parallel^2 \vec{b}_\parallel}_{1} - \underbrace{\eta_\parallel \partial_\parallel V_\parallel \vec{b}_\parallel}_{2} - \underbrace{D_\perp \partial_\perp (m_i n V_\parallel) \vec{b}_\perp}_{3} \right] = -\underbrace{\partial_\parallel p}_{4} + S_m \qquad \text{(B.4)}$$

Here the terms (1), (2) and (3) on the left hand side represent the convective parallel transport of momentum, the viscous parallel transport of momentum and viscous perpendicular transport of momentum. The term (4) on the right hand side means that, in absence of any momentum sources $S_m$, a non-divergence free momentum field is accompanied by a change in static pressure. A momentum source $S_m$ is e.g. due to ion-neutral collisions, such as charge exchange collisions.

**Energy Conservation Equations**

The energy conservation equation for the electrons is given by

$$\vec{\nabla} \cdot \left[ \underbrace{\frac{5}{2} n T_e V_\parallel \vec{b}_\parallel}_{1} - \underbrace{\kappa_e \partial_\parallel T_e \vec{b}_\parallel}_{2} - \underbrace{\frac{5}{2} T_e D_\perp \partial_\perp n \vec{b}_\perp}_{3} - \underbrace{\chi_{e,\perp} n \partial_\perp T_e \vec{b}_\perp}_{4} \right]$$
$$= \underbrace{k(T_i - T_e)}_{5} + S_{e,e} \qquad \text{(B.5)}$$

Here term (1) represents the parallel convective energy transport, term (2) the conductive parallel transport, term (3) the perpendicular convective transport, term (4) the perpendicular conductive transport and term (5) the energy loss from the electrons to the ions. The perpendicular heat conductivity is, similar to the perpendicular particle diffusion coefficient, an anomalous quantity which is determined from the experimental data. Electron energy sources and sinks are represented by the term $S_{e,e}$. For example line radiation, due to collisions of electrons with neutrals, is included in $S_{e,e}$. Analogously to the electron

energy conservation equation the ion energy conservation equation is given by

$$\vec{\nabla} \cdot \left[ \underbrace{\frac{5}{2} n T_i V_\| \vec{b}_\|}_{1} - \underbrace{\kappa_i \partial_\| T_i \vec{b}_\|}_{2} - \underbrace{\frac{5}{2} T_i D_\perp \partial_\perp n \vec{b}_\perp}_{3} - \underbrace{\chi_{i,\perp} n \partial_\perp T_i \vec{b}_\perp}_{4} \right]$$
$$= \underbrace{k(T_e - T_i)}_{5} + S_{e,i} \qquad \text{(B.6)}$$

The parallel heat conductivities $\kappa_{e,i}$ are given by the Spitzer formulas

$$\kappa_{e.i} = \kappa_{0,e,i} T_{e,i}^{5/2}, \quad \kappa_{0,e} \approx 2000 \, \text{W}/(\text{eV})^{7/2}\text{m}, \quad \kappa_{0,i} \approx 60 \, \text{W}/(\text{eV})^{7/2}\text{m} \quad \text{(B.7)}$$

Since $\kappa_{0,e} \gg \kappa_{0,i}$, the electron heat conduction is considerably more effective than the ion conductivity.

**Trace Impurity Ion Model**

Impurity neutrals and ions are treated as trace particles, which influence the background plasma only via radiation [127]. Therefore the model is only valid for sufficiently low impurity concentrations, which is however usually the case in fusion plasmas. For the impurities the same particle conservation equation as for the main ions holds for each impurity charge state. The impurity force balance equation is given by

$$\underbrace{\frac{m_I m_i (V_{I,\|}^z - V_\|)}{\tau_s}}_{1} = -\underbrace{\partial_\|(n_I^z T_i)}_{2} + \underbrace{n_I^z Z e E_\|}_{3} + \underbrace{0.71 n_I^z Z^2 \partial_\| T_e}_{4} + \underbrace{n_I^z \beta \partial_\| T_i}_{5}, \quad \text{(B.8)}$$

where $V_{i,\|}^z$ and $n_I^z$ are the ion velocity and densitiy, $E_\|$ is the parallel electric field, $e$ the elementary charge and $Z$ the impurities charge number. Term (1) in Eq. B.8 represents the friction between main ions and impurites. The *ion stopping time* $\tau_s$ in this term is the typical time within which the impurities reach the same speed as the main ions. Terms (2) and (3) represent the impurity pressure force. Terms (4) and (5) are the forces exerted due to the main ion and electron temperature gradients. The coefficient $\beta$ depends on $m, m_I$ and $Z$.

**Neutral Transport**

The neutral transport is treated by the code EIRENE, which solves a kinetic equation for each neutral species by means of a Monte-Carlo technique. EIRENE is coupled to databases, from which the reaction rates with the background plasma, e.g. ionization and charge exchange collisions, as well as the velocity distribution and species of the recycled neutrals are calculated.

# Bibliography

[1] U.S. Energy Information Administration (EIA), "International energy outlook 2016," 2016.

[2] IPCC, *Climate change 2013: the physical science basis: Working Group I contribution to the Fifth assessment report of the Intergovernmental Panel on Climate Change.* Cambridge University Press, 2014.

[3] A. Kallenbach, M. Bernert, T. Eich, A. Herrmann, F. Reimold, J. Schweinzer, B. Sieglin, M. Wischmeier, C. Giroud, G. Maddison, *et al.*, "Multi-machine comparisons of divertor heat flux mitigation by radiative cooling," tech. rep., 2012.

[4] H. Bethe, "Energy production in stars," *Phys. Rev.*, vol. 55, pp. 434–456, Mar 1939.

[5] J. Huba, "NRL: Plasma formulary," 2004.

[6] G. Miley, H. Towner, and N. Ivich, "Fusion cross sections and reactivities," tech. rep., Illinois Univ., Urbana (USA), 1974.

[7] J. Lawson, "Some criteria for a power producing thermonuclear reactor," *Proceedings of the Physical Society. Section B*, vol. 70, no. 1, p. 6, 1957.

[8] J. Wesson and D. Campbell, *Tokamaks.* Oxford University Press, 2011.

[9] M. Shimada *et al.*, "Progress in ITER physics basis, chapter 1: Overview and summary," *Nucl. Fusion*, vol. 47, no. 6, 2007.

[10] U. Stroth, *Plasmaphysik: Phänomene Grundladen, Anwendungen.* Vieweg+ Teubner Verlag, Wiesbaden, 2011.

[11] M. Keilhacker, A. Gibson, C. Gormezano, P. Lomas, P. Thomas, M. Watkins, P. Andrew, B. Balet, D. Borba, C. Challis, *et al.*, "High fusion performance from deuterium-tritium plasmas in JET," *Nucl. Fusion*, vol. 39, no. 2, p. 209, 1999.

[12] IPP, Grafik: Dr. Christian Brandt.

[13] M. Shimada, M. Nagami, K. Ioki, S. Izumi, M. Maeno, H. Yokomizo, K. Shinya, H. Yoshida, A. Kitsunezaki, N. Brooks, *et al.*, "Helium ash exhaust with single-null poloidal divertor in doublet iii," *Phys. Rev. Lett.*, vol. 47, no. 11, p. 796, 1981.

[14] F. Wagner, G. Becker, K. Behringer, D. Campbell, A. Eberhagen, W. Engelhardt, G. Fussmann, O. Gehre, J. Gernhardt, G. v. Gierke, *et al.*, "Regime of improved confinement and high beta in neutral-beam-heated divertor discharges of the asdex tokamak," *Phys. Rev. Lett.*, vol. 49, no. 19, p. 1408, 1982.

[15] R. Schneider, H.-S. Bosch, D. Coster, J. Fuchs, J. Gafert, G. Haas, A. Herrmann, M. Kaufmann, A. Kallenbach, J. Neuhauser, *et al.*, "Role of divertor geometry on detachment in ASDEX Upgrade," *J. Nucl. Mater.*, vol. 266, pp. 175–181, 1999.

[16] A. Loarte, R. Monk, J. Martin-Solis, D. Campbell, A. Chankin, S. Clement, S. Davies, J. Ehrenberg, S. Erents, H. Guo, *et al.*, "Plasma detachment in JET Mark I divertor experiments," *Nucl. Fusion*, vol. 38, no. 3, p. 331, 1998.

[17] ASDEX Upgrade Design Team and Tokamak Theory Group, "ASDEX Upgrade. Definition of a tokamak experiment with a reactor compatible poloidal divertor, Technical Report IPP 1/197," 1982.

[18] W. Köppendörfer, "ASDEX Upgrade – ein Tokamakexperiment mit reaktorrelevantem Divertor," *Physikalische Blätter*, vol. 46, no. 8, pp. 324–326, 1990.

[19] ASDEX Group, "Divertor tokamak ASDEX, Technical Report IPP III/47," 1978.

[20] O. Gruber *et al.*, "Physics background of the ASDEX Upgrade project," *J. Nucl. Mater.*, vol. 121, pp. 407–414, 1984.

[21] H. Zohm, G. Gantenbein, G. Giruzzi, S. Günter, F. Leuterer, M. Maraschek, J. Meskat, A. Peeters, W. Suttrop, D. Wagner, *et al.*, "Experiments on neoclassical tearing mode stabilization by eccd in ASDEX Upgrade," *Nucl. Fusion*, vol. 39, no. 5, p. 577, 1999.

[22] H. Zohm, G. Gantenbein, F. Leuterer, A. Manini, M. Maraschek, Q. Yu, *et al.*, "Control of MHD instabilities by eccd: ASDEX Upgrade results and implications for ITER," *Nucl. Fusion*, vol. 47, no. 3, p. 228, 2007.

[23] A. Herrmann and O. Gruber, "ASDEX Upgrade - introduction and overview," *Fusion Science and Technology*, vol. 44, no. 3, pp. 569–577, 2003.

[24] W. Schneider, P. McCarthy, K. Lackner, O. Gruber, K. Behler, P. Martin, and R. Merkel, "ASDEX Upgrade MHD equilibria reconstruction on distributed workstations," *Fusion Eng. Des.*, vol. 48, no. 1, pp. 127–134, 2000.

[25] P. J. McCarthy, P. Martin, and W. Schneider, "The CLISTE interpretive equilibrium code, Technical Report IPP 5/85," 1999.

[26] A. Mlynek, G. Schramm, H. Eixenberger, G. Sips, K. McCormick, M. Zilker, K. Behler, J. Eheberg, and A. Team, "Design of a digital multiradian phase detector and its application in fusion plasma interferometry," *Rev. Sci. Instrum.*, vol. 81, no. 3, p. 033507, 2010.

[27] H. Murmann, S. Götsch, H. Röhr, H. Salzmann, and K. Steuer, "The thomson scattering systems of the asdex upgrade tokamak," *Rev. Sci. Instrum.*, vol. 63, no. 10, pp. 4941–4943, 1992.

[28] J. A. Bittencourt, *Fundamentals of plasma physics.* Springer Science & Business Media, 2013.

[29] I. H. Hutchinson, "Principles of plasma diagnostics," *Plasma Phys. Control. Fusion*, vol. 44, no. 12, p. 2603, 2002.

[30] E. Wolfrum, F. Aumayr, D. Wutte, H. Winter, E. Hintz, D. Rusbüldt, and R. Schorn, "Fast lithium-beam spectroscopy of tokamak edge plasmas," *Rev. Sci. Instrum.*, vol. 64, no. 8, pp. 2285–2292, 1993.

[31] J. Schweinzer, E. Wolfrum, F. Aumayr, M. Pockl, H. Winter, R. Schorn, E. Hintz, and A. Unterreiter, "Reconstruction of plasma edge density profiles from li i (2s-2p) emission profiles," *Plasma Phys. Control. Fusion*, vol. 34, no. 7, p. 1173, 1992.

[32] R. Fischer, E. Wolfrum, J. Schweinzer, *et al.*, "Probabilistic lithium beam data analysis," *Plasma Phys. Control. Fusion*, vol. 50, no. 8, p. 085009, 2008.

[33] S. Rathgeber, L. Barrera, T. Eich, R. Fischer, B. Nold, W. Suttrop, M. Willensdorfer, E. Wolfrum, *et al.*, "Estimation of edge electron temperature profiles via forward modelling of the electron cyclotron radiation transport at ASDEX Upgrade," *Plasma Phys. Control. Fusion*, vol. 55, no. 2, p. 025004, 2012.

[34] M. Bernert, T. Eich, A. Burckhart, J. Fuchs, L. Giannone, A. Kallenbach, R. McDermott, B. Sieglin, and A. U. Team, "Application of AXUV diode detectors at ASDEX Upgrade," *Rev. Sci. Instrum.*, vol. 53, no. 3, p. 104003, 2014.

[35] B. Sieglin, M. Faitsch, A. Herrmann, B. Brucker, T. Eich, L. Kammerloher, and S. Martinov, "Real time capable infrared thermography for ASDEX Upgrade," *Rev. Sci. Instrum.*, vol. 86, no. 11, p. 113502, 2015.

[36] A. Herrmann, W. Junker, K. Gunther, S. Bosch, M. Kaufmann, J. Neuhauser, G. Pautasso, T. Richter, and R. Schneider, "Energy flux to the ASDEX Upgrade diverter plates determined by thermography and calorimetry," *Plasma Phys. Control. Fusion*, vol. 37, no. 1, p. 17, 1995.

[37] M. Weinlich and A. Carlson, "Flush mounted probes in ASDEX Upgrade - can they be operated as triple probes?," *Contrib. Plasma Phys.*, vol. 36, no. S1, pp. 53–59, 1996.

[38] R. Chodura, "Physics of plasma-wall interactions in controlled fusion," *Controlled Fusion, Plenum, New York*, p. 99, 1986.

[39] K. U. Riemann, "The bohm criterion and sheath formation," *Journal of Physics D: Applied Physics*, vol. 24, no. 4, p. 493, 1991.

[40] J. P. Gunn, "The influence of magnetization strength on the sheath: Implications for flush-mounted probes," *Phys. Plasmas*, vol. 4, no. 12, pp. 4435–4446, 1997.

[41] P. C. Stangeby, "The plasma sheath," in *Physics of Plasma-Wall Interactions in Controlled Fusion*, pp. 41–97, Springer, 1986.

[42] P. C. Stangeby *et al.*, *The Plasma Boundary of Magnetic Fusion Devices*, vol. 224. Institute of Physics Publishing Bristol, 2000.

[43] W. Eckstein and H. Verbeek, "Data compendium for plasma-surface interactions, chapter 2," *Nucl. Fusion*, vol. 24, no. S1, p. S9, 1984.

[44] W. Eckstein, "Reflection (Backscattering), Technical Report IPP 17/12," 2009.

[45] D. Tskhakaya and S. Kuhn, "Influence of initial energy on the effective secondary-electron emission coefficient in the presence of an oblique magnetic field," *Contrib. Plasma Phys.*, vol. 40, no. 3-4, pp. 484–490, 2000.

[46] R. Aymar *et al.*, "The ITER design," *Plasma Phys. Control. Fusion*, vol. 44, no. 5, p. 519, 2002.

[47] A. Loarte *et al.*, "Power and particle control," *Nucl. Fusion*, vol. 47, no. 6, p. S203, 2007.

[48] J. Gunn, S. Carpentier-Chouchana, F. Escourbiac, T. Hirai, S. Panayotis, R. Pitts, Y. Corre, R. Dejarnac, M. Firdaouss, M. Kočan, *et al.*, "Surface heat loads on the ITER divertor vertical targets," *Nucl. Fusion*, vol. 57, no. 4, p. 046025, 2017.

[49] A. Kallenbach *et al.*, "Impurity seeding for tokamak power exhaust: from present devices via ITER to DEMO," *Plasma Phys. Control. Fusion*, vol. 55, no. 12, p. 124041, 2013.

[50] R. Parker *et al.*, "Plasma-wall interactions in ITER," *J. Nucl. Mater.*, vol. 241, pp. 1–26, 1997.

[51] T. Eich *et al.*, "Scaling of the tokamak near the scrape-off layer H-mode power width and implications for ITER," *Nucl. Fusion*, vol. 53, no. 9, p. 093031, 2013.

[52] A. Kallenbach, M. Bernert, T. Eich, J. Fuchs, L. Giannone, A. Herrmann, J. Schweinzer, W. Treutterer, *et al.*, "Optimized tokamak power exhaust with double radiative feedback in ASDEX Upgrade," *Nucl. Fusion*, vol. 52, no. 12, p. 122003, 2012.

[53] F. Reimold, M. Wischmeier, M. Bernert, S. Potzel, D. Coster, X. Bonnin, D. Reiter, G. Meisl, A. Kallenbach, L. Aho-Mantila, *et al.*, "Experimental studies and modeling of complete H-mode divertor detachment in ASDEX Upgrade," *J. Nucl. Mater.*, vol. 463, pp. 128–134, 2015.

[54] S. Braginskii, "Transport processes in a plasma," *Rev. Plasma Phys.*, vol. 1, p. 205, 1965.

[55] R. Schneider, X. Bonnin, K. Borrass, D. Coster, H. Kastelewicz, D. Reiter, V. Rozhansky, and B. Braams, "Plasma edge physics with B2-EIRENE," *Contrib. Plasma Phys.*, vol. 46, no. 1-2, pp. 3–191, 2006.

[56] M. Bernert, M. Wischmeier, A. Huber, F. Reimold, B. Lipschultz, C. Lowry, S. Brezinsek, R. Dux, T. Eich, A. Kallenbach, *et al.*, "Power exhaust by sol and pedestal radiation at ASDEX Upgrade and JET," *Nucl. Mater. Energy*, 2017.

[57] H. P. Summers, "http://www.adas.ac.uk./manual.php," 2004.

[58] Y. Shimomura, M. Keilhacker, K. Lackner, and H. Murmann, "Characteristics of the divertor plasma in neutral-beam-heated asdex discharges," *Nucl. Fusion*, vol. 23, no. 7, p. 869, 1983.

[59] A. Kallenbach *et al.*, "Partial detachment of high power discharges in ASDEX Upgrade," *Nucl. Fusion*, vol. 55, no. 5, p. 053026, 2015.

[60] P. Stangeby, "Can detached divertor plasmas be explained as self-sustained gas targets?," *Nucl. Fusion*, vol. 33, no. 11, p. 1695, 1993.

[61] S. Krasheninnikov, A. Kukushkin, and A. Pshenov, "Divertor plasma detachment," *Phys. Plasmas*, vol. 23, no. 5, p. 055602, 2016.

[62] A. Scarabosio, T. Eich, A. Herrmann, B. Sieglin, J.-E. contributors, *et al.*, "Outer target heat fluxes and power decay length scaling in L-mode plasmas at JET and AUG," *J. Nucl. Mater.*, vol. 438, pp. S426–S430, 2013.

[63] G. B. Arfken and H. J. Weber, *Mathematical methods for physicists*. AAPT, 1999.

[64] M. A. Makowski *et al.*, "Analysis of a multi-machine database on divertor heat fluxes a," *Phys. Plasmas*, vol. 19, no. 5, p. 056122, 2012.

[65] B. Sieglin *et al.*, "Investigation of scrape-off layer and divertor heat transport in ASDEX Upgrade L-mode," *Plasma Phys. Control. Fusion*, vol. 58, no. 5, p. 055015, 2016.

[66] T. Evans, R. Moyer, J. Watkins, P. Thomas, T. Osborne, J. Boedo, M. Fenstermacher, K. Finken, R. Groebner, M. Groth, *et al.*, "Suppression of large edge localized modes in high confinement DIII-D plasmas with a stochastic magnetic boundary," *J. Nucl. Mater.*, vol. 337, pp. 691–696, 2005.

[67] W. Suttrop *et al.*, "First observation of edge localized modes mitigation with resonant and nonresonant magnetic perturbations in ASDEX Upgrade," *Phys. Rev. Lett.*, vol. 106, p. 225004, 2011.

[68] H. Zohm, "Edge localized modes (ELMs)," *Plasma Phys. Control. Fusion*, vol. 38, no. 2, p. 105, 1996.

[69] J. Connor, "A review of models for ELMs," *Plasma Phys. Control. Fusion*, vol. 40, no. 2, p. 191, 1998.

[70] M. Willensdorfer, E. Strumberger, W. Suttrop, M. Dunne, R. Fischer, G. Birkenmeier, D. Brida, M. Cavedon, S. Denk, V. Igochine, *et al.*, "Three dimensional boundary displacement due to stable ideal kink modes excited by external $n = 2$ magnetic perturbations," *Nucl. Fusion*, vol. 57, no. 11, 2017.

[71] M. Lanctot, R. Buttery, J. De Grassie, T. Evans, N. Ferraro, J. Hanson, S. Haskey, R. Moyer, R. Nazikian, T. Osborne, *et al.*, "Sustained suppression of type-I edge-localized modes with dominantly $n = 2$ magnetic fields in DIII-D," *Nucl. Fusion*, vol. 53, no. 8, p. 083019, 2013.

[72] D. Ryan, Y. Liu, A. Kirk, W. Suttrop, B. Dudson, M. Dunne, R. Fischer, J. Fuchs, M. Garcia-Munoz, B. Kurzan, *et al.*, "Toroidal modelling of resonant magnetic perturbations response in ASDEX Upgrade: coupling between field pitch aligned response and kink amplification," *Plasma Phys. Control. Fusion*, vol. 57, no. 9, p. 095008, 2015.

[73] M. Wade, R. Nazikian, T. Evans, N. Ferraro, R. Moyer, D. Orlov, R. Buttery, M. Fenstermacher, A. Garofalo, M. Lanctot, *et al.*, "Advances in the physics understanding of ELM suppression using resonant magnetic perturbations in DIII-D," *Nucl. Fusion*, vol. 55, no. 2, p. 023002, 2015.

[74] F. Orain, M. Bécoulet, G. Dif-Pradalier, G. Huijsmans, S. Pamela, E. Nardon, C. Passeron, G. Latu, V. Grandgirard, A. Fil, *et al.*, "Nonlinear magnetohydrodynamic modeling of plasma response to resonant magnetic perturbations," *Phys. Plasmas*, vol. 20, no. 10, p. 102510, 2013.

[75] W. Suttrop, "https://www.aug.ipp.mpg.de/augtwiki/bin/view/cwac/pslresponse."

[76] H. Zohm, *Magnetohydrodynamic stability of tokamaks.* John Wiley & Sons, 2014.

[77] P. Ghendrih, A. Grosman, and H. Capes, "Theoretical and experimental investigations of stochastic boundaries in tokamaks," *Plasma Phys. Control. Fusion*, vol. 38, no. 10, p. 1653, 1996.

[78] P. Cahyna and E. Nardon, "Resonant magnetic perturbations and divertor footprints in poloidally diverted tokamaks," *arXiv preprint arXiv:1005.3663*, 2010.

[79] P. Ghendrih, H. Capes, F. Nguyen, and A. Samain, "Control of the edge transport with the ergodic divertor," *Contrib. Plasma Phys.*, vol. 32, no. 3-4, pp. 179–191, 1992.

[80] T. Evans, R. Moyer, and P. Monat, "Modeling of stochastic magnetic flux loss from the edge of a poloidally diverted tokamak," *Phys. Plasmas*, vol. 9, no. 12, pp. 4957–4967, 2002.

[81] O. Schmitz *et al.*, "Aspects of three dimensional transport for ELM control experiments in ITER-similar shape plasmas at low collisionality in DIII-D," *Plasma Phys. Control. Fusion*, vol. 50, no. 12, p. 124029, 2008.

[82] S. Abdullaev, M. Jakubowski, M. Lehnen, O. Schmitz, and B. Unterberg, "On description of magnetic stochasticity in poloidal divertor tokamaks," *Phys. Plasmas (1994-present)*, vol. 15, no. 4, p. 042508, 2008.

[83] P. Cahyna, "Model for screening of resonant magnetic perturbations by plasma in a realistic tokamak geometry and its impact on divertor strike points," *J. Nucl. Mater.*, vol. 415, no. 1, Supplement, pp. S927 – S931, 2011.

[84] R. Fitzpatrick, "Interaction of tearing modes with external structures in cylindrical geometry (plasma)," *Nucl. Fusion*, vol. 33, no. 7, p. 1049, 1993.

[85] M. Becoulet, F. Orain, P. Maget, N. Mellet, X. Garbet, E. Nardon, G. Huysmans, T. Casper, A. Loarte, P. Cahyna, *et al.*, "Screening of resonant magnetic perturbations by flows in tokamaks," *Nucl. Fusion*, vol. 52, no. 5, p. 054003, 2012.

[86] Y. Liu, A. Kirk, and E. Nardon, "Full toroidal plasma response to externally applied nonaxisymmetric magnetic fields," *Phys. Plasmas*, vol. 17, no. 12, p. 122502, 2010.

[87] Q. Yu, S. Günter, Y. Kikuchi, and K. Finken, "Numerical modelling of error field penetration," *Nucl. Fusion*, vol. 48, no. 2, p. 024007, 2008.

[88] P. Merkel and E. Strumberger, "Linear MHD stability studies with the starwall code," *arXiv preprint arXiv:1508.04911*, 2015.

[89] A. Taroni, G. Corrigan, G. Radford, R. Simonini, J. Spence, and S. Weber, "The multi-fluid codes edgeid and Edge2D: Models and results," *Contrib. Plasma Phys.*, vol. 32, no. 3-4, pp. 438–443, 1992.

[90] Y. Feng, F. Sardei, J. Kisslinger, and P. Grigull, "A 3D monte carlo code for plasma transport in island divertors," *J. Nucl. Mater.*, vol. 241, pp. 930–934, 1997.

[91] M. Kobayashi, Y. Feng, F. Sardei, D. Reiter, K. Finken, and D. Reiser, "3D numerical transport study of the edge ergodized plasma in TEXTOR-DED," *Nucl. Fusion*, vol. 44, no. 6, p. S64, 2004.

[92] D. Harting, D. Reiter, Y. Feng, O. Schmitz, D. Reiser, and H. Frerichs, "3D edge transport studies with EMC3-EIRENE for the dynamic ergodic divertor (DED) at TEXTOR," *Contrib. Plasma Phys.*, vol. 48, no. 1-3, pp. 99–105, 2008.

[93] H. Frerichs *et al.*, "Three-dimensional edge transport simulations for DIII-D plasmas with resonant magnetic perturbations," *Nucl. Fusion*, vol. 50, no. 3, p. 034004, 2010.

[94] H. Frerichs, D. Reiter, O. Schmitz, D. Harting, T. Evans, and Y. Feng, "On gas flow effects in 3D edge transport simulations for DIII-D plasmas with resonant magnetic perturbations," *Nucl. Fusion*, vol. 52, no. 5, p. 054008, 2012.

[95] H. Frerichs, O. Schmitz, T. Evans, Y. Feng, and D. Reiter, "The pattern of parallel edge plasma flows due to pressure gradients, recycling, and resonant magnetic perturbations in DIII-D," *Phys. Plasmas*, vol. 22, no. 7, p. 072508, 2015.

[96] J. Lore, J. Canik, Y. Feng, J.-W. Ahn, R. Maingi, and V. Soukhanovskii, "Implementation of the 3D edge plasma code EMC3-EIRENE on NSTX," *Nucl. Fusion*, vol. 52, no. 5, p. 054012, 2012.

[97] T. Lunt *et al.*, "First EMC3-EIRENE simulations of the impact of the edge magnetic perturbations at ASDEX Upgrade compared with the experiment simulations of the impact of the edge magnetic perturbations at asdex upgrade compared with the experiment," *Nucl. Fusion*, vol. 52, no. 5, p. 054013, 2012.

[98] D. Brida, T. Lunt, M. Wischmeier, G. Birkenmeier, P. Cahyna, D. Carralero, M. Faitsch, Y. Feng, B. Kurzan, M. Schubert, *et al.*, "Determination of the stochastic layer properties induced by magnetic perturbations via heat pulse experiments at ASDEX Upgrade," *Nucl. Mater. Energy*, 2017.

[99] Y. Feng *et al.*, "Formulation of a monte carlo model for edge plasma transport," in *27. EPS Conf. on Plasma Physics, Budapest, Hungaria, vol. 24B, pp. 1188-91*, 2000.

[100] T. Lunt, D. Carralero, Y. Feng, G. Birkenmeier, H. W. Müller, S. Müller, M. Wischmeier, *et al.*, "EMC3-EIRENE simulations of particle-and energy fluxes to main chamber-and divertor plasma facing components in ASDEX Upgrade compared to experiments," *J. Nucl. Mater.*, vol. 463, pp. 744–747, 2015.

[101] T. Lunt, G. P. Canal, Y. Feng, H. Reimerdes, B. P. Duval, B. Labit, W. A. J. Vijvers, D. Coster, K. Lackner, and M. Wischmeier, "First EMC3-EIRENE simulations of the TCV snowflake divertor," *Plasma Phys. Control. Fusion*, vol. 56, no. 3, p. 035009, 2014.

[102] F. Reimold, M. Wischmeier, S. Potzel, L. Guimarais, D. Reiter, M. Bernert, M. Dunne, T. Lunt, *et al.*, "The high field side high density region in SOLPS-modeling of nitrogen-seeded H-modes in ASDEX Upgrade," *Nucl. Mater. Energy*, 2017.

[103] M. Faitsch, B. Sieglin, T. Eich, A. Herrmann, W. Suttrop, *et al.*, "2D heat flux in ASDEX Upgrade L-mode with magnetic perturbation," *Nucl. Mater. Energy*, 2017.

[104] D. Laxhuber, "Analyse von fluktuationen der divertor-leistungsflüsse in asdex upgrade," bachelor thesis, 2017.

[105] K. Ida, T. Kobayashi, M. Yoshinuma, Y. Suzuki, Y. Narushima, T. Evans, S. Ohdachi, H. Tsuchiya, S. Inagaki, and K. Itoh, "Bifurcation physics of magnetic islands and stochasticity explored by heat pulse propagation studies in toroidal plasmas," *Nucl. Fusion*, vol. 56, no. 9, p. 092001, 2016.

[106] N. L. Cardozo, "Perturbative transport studies in fusion plasmas," *Plasma Phys. Control. Fusion*, vol. 37, no. 8, p. 799, 1995.

[107] E. Poli, "TORBEAM, a beam tracing code for electron-cyclotron waves in tokamak plasmas," *Comput. Phys. Commun.*, vol. 136, no. 1–2, pp. 90 – 104, 2001.

[108] K. Finken, B. Unterberg, Y. Xu, S. Abdullaev, M. Jakubowski, M. Lehnen, M. de Bock, S. Bozhenkov, S. Brezinsek, C. Busch, *et al.*, "Influence of the dynamic ergodic divertor on transport properties in TEXTOR," *Nucl. Fusion*, vol. 47, no. 7, p. 522, 2007.

[109] M. Jakubowski, O. Schmitz, S. Abdullaev, S. Brezinsek, K. Finken, A. Krämer-Flecken, M. Lehnen, U. Samm, K. Spatschek, B. Unterberg, *et al.*, "Change of the magnetic-field topology by an ergodic divertor and the effect on the plasma structure and transport," *Phys. Rev. Lett.*, vol. 96, no. 3, p. 035004, 2006.

[110] A. Samain, A. Grosman, T. Blenski, G. Fuchs, and B. Steffen, "An ergodic divertor for Tore Supra," *J. Nucl. Mater.*, vol. 128, pp. 395–399, 1984.

[111] P. Ghendrih, M. Bécoulet, L. Colas, A. Grosman, R. Guirlet, J. Gunn, T. Loarer, A. Azéroual, V. Basiuk, B. Beaumont, *et al.*, "Progress in ergodic divertor operation on Tore Supra," *Nucl. Fusion*, vol. 42, no. 10, p. 1221, 2002.

[112] T. Eich, B. Sieglin, A. Scarabosio, A. Herrmann, A. Kallenbach, G. Matthews, S. Jachmich, S. Brezinsek, M. Rack, R. Goldston, *et al.*, "Empiricial scaling of inter-ELM power widths in ASDEX Upgrade and JET," *J. Nucl. Mater.*, vol. 438, pp. S72–S77, 2013.

[113] O. Schmitz, M. Becoulet, P. Cahyna, T. Evans, Y. Feng, H. Frerichs, A. Loarte, R. Pitts, D. Reiser, M. Fenstermacher, *et al.*, "Three-dimensional modeling of plasma edge transport and divertor fluxes during application of resonant magnetic perturbations on ITER," *Nucl. Fusion*, vol. 56, no. 6, p. 066008, 2016.

[114] A. Kallenbach *et al.*, "Divertor power load feedback with nitrogen seeding in ASDEX Upgrade," *Plasma Phys. Control. Fusion*, vol. 52, no. 5, p. 055002, 2010.

[115] G. Staebler and F. Hinton, "Currents in the scrape-off layer of diverted tokamaks," *Nucl. Fusion*, vol. 29, no. 10, p. 1820, 1989.

[116] A. Kallenbach *et al.*, "Electric currents in the scrape-off layer in ASDEX Upgrade," *J. Nucl. Mater.*, vol. 290, pp. 639–643, 2001.

[117] P. C. Stangeby and G. M. McCracken, "Plasma boundary phenomena in tokamaks," *Nucl. Fusion*, vol. 30, no. 7, p. 1225, 1990.

[118] J. A. Tagle *et al.*, "Errors in measuring electron temperatures using a single langmuir probe in a magnetic field," *Plasma Phys. Control. Fusion*, vol. 29, no. 3, p. 297, 1987.

[119] R. D. Monk *et al.*, "Interpretation of ion flux and electron temperature profiles at the JET divertor target during high recycling and detached discharges," *J. Nucl. Mater.*, vol. 241, pp. 396–401, 1997.

[120] S. Potzel *et al.*, "A new experimental classification of divertor detachment in ASDEX Upgrade," *Nucl. Fusion*, vol. 54, no. 1, p. 013001, 2014.

[121] M. Faitsch, B. Sieglin, T. Eich, A. Herrmann, W. Suttrop, *et al.*, "Divertor heat load in ASDEX Upgrade L-mode in presence of external magnetic perturbation," *arXiv preprint arXiv:1703.03192*, 2017.

[122] P. Cahyna *et al.*, "Method for comparison of tokamak divertor strike point data with magnetic perturbation models," *Nucl. Fusion*, vol. 54, no. 6, p. 064002, 2014.

[123] W. Suttrop, "First observation of edge localized modes mitigation with resonant and nonresonant magnetic perturbations in ASDEX Upgrade," *Phys. Rev. Lett.*, vol. 106, p. 225004, Jun 2011.

[124] P. Schneider, "Pedestal and edge localized mode characteristics with different first wall materials and nitrogen seeding in ASDEX Upgrade," *Plasma Phys. Control. Fusion*, vol. 57, no. 1, p. 014029, 2014.

[125] J. Stober, P. Lomas, G. Saibene, Y. Andrew, P. Belo, G. Conway, A. Herrmann, L. Horton, M. Kempenaars, H.-R. Koslowski, *et al.*, "Small ELM regimes with good confinement on JET and comparison to those on ASDEX Upgrade, Alcator C-mod and JT-60U," *Nucl. Fusion*, vol. 45, no. 11, p. 1213, 2005.

[126] M. Wischmeier *et al.*, "High density operation for reactor-relevant power exhaust," *J. Nucl. Mater.*, vol. 463, pp. 22 – 29, 2015.

[127] Y. Feng, T. Lunt, F. Sardei, and X. Zha, "Implicit coupling of impurity transport at the SOL–core interface," *Comput. Phys. Commun.*, vol. 184, no. 6, pp. 1555–1561, 2013.